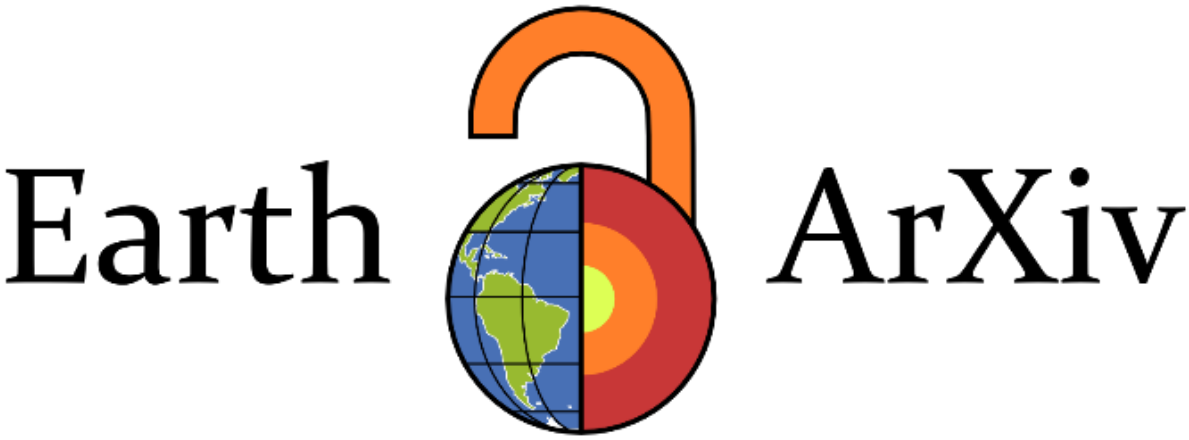

Submitted for review to *Science Advances*

Lithological heterogeneity controls high-temperature ductile deformation and late melt infiltration in moderately-magmatic OCCs

Authors

Andrew J. Parsons[1*], Rebecca Kuehn[2], Barbara E. John[3], Jeremy R. Deans[4], Ethan L. Lopes[5], Kuan-Yu Lin[6], C. Johan Lissenberg[7], Carlotta Ferrando[8], Andrew McCaig[9], Susan Q. Lang[10], Peter Blum[11] , Natsue Abe[12], William J. Brazelton[13], Rémi Coltat[14], Kristin L. Dickerson[15], Marguerite Godard[16], Frieder Klein[17], Haiyang Liu[18], Toshio Nozaka[19], Vamdev Pathak[20], Mark K. Reagan[21], Jordyn A. Robare[22], Ivan P. Savov[9], Esther M. Schwarzenbach[23], Olivier Sissmann[24], Fengping Wang[25]

***Corresponding Author Email & ORCID:**
andy.parsons@plymouth.ac.uk
https://orcid.org/0000-0001-7538-9418

Author affiliations:

1. School of Geography, Earth and Environmental Sciences, University of Plymouth; Plymouth, UK.
2. Institute of Geosciences and Geography, Martin-Luther-University Halle-Wittenberg; Halle, Germany.
3. Department of Geology and Geophysics, University of Wyoming; Laramie, WY, USA.
4. School of Biological, Environmental, and Earth Sciences, University of Southern Mississippi; Hattiesburg, MS, USA.
5. Department of Geophysics, Stanford University; Stanford, CA, USA.
6. National Museum of Natural History, Smithsonian Institution; Washington, DC, USA.
7. School of Earth and Environmental Sciences, Cardiff University; Cardiff, UK.
8. Department of Earth, Environmental and Life Sciences, University of Genova; Genova, Italy.
9. School of Earth and Environment, University of Leeds; Leeds, UK.
10. Departments of Geology and Geophysics, Woods Hole Oceanographic Institution; Woods Hole, MA, USA.
11. International Ocean Discovery Program, Texas A&M University; College Station, TX, USA.
12. Japan Agency for Marine-Earth Science and Technology; Yokohama, Japan.
13. School of Biological Sciences, University of Utah; Salt Lake City, UT, USA.
14. Instituto Andaluz de Ciencias de la Tierra (IACT), CSIC, Armilla, Granada, Spain; and ISTO, UMR 7327, Univ Orleans, CNRS, BRGM, OSUC, Orléans, France.
15. Department of Earth and Planetary Sciences, University of California, Santa Cruz; Santa Cruz, CA, USA.
16. Géosciences Montpellier, CNRS, University of Montpellier; Montpellier, France.
17. Department of Marine Chemistry and Geochemistry, Woods Hole Oceanographic Institution; Woods Hole, MA, USA.
18. Key Laboratory of Ocean Observation and Forecasting, Center of Deep Sea Research, Institute of Oceanology, Chinese Academy of Sciences, Qingdao 266071, P. R. China.
19. Department of Earth Sciences, Okayama University; Okayama, Japan.
20. Department of Geology, Central University of Punjab; Bathinda, India.
21. School of Earth, Environment, and Sustainability, University of Iowa; Iowa City, IA, USA.
22. School of Molecular Sciences, Arizona State University; Phoenix, AZ, USA.
23. Department of Geosciences, University of Fribourg; Fribourg, Switzerland.
24. IFP Energies Nouvelles; Rueil-Malmaison, France.
25. Key Laboratory of Polar Ecosystem and Climate Change, Ministry of Education; and School of Oceanography, Shanghai Jiao Tong University; Shanghai, China.

ABSTRACT

Oceanic core complexes (OCCs) are a fundamental component of slow-to-ultraslow spreading mid-ocean ridges, yet the processes that control OCC formation and evolution are poorly understood especially with respect to their high-temperature lithospheric roots. We present detailed analyses of high-temperature ductile deformation preserved in drill-core from IODP Hole U1601C, on the Atlantis Massif OCC (30°N, MAR). We show that gabbroic intrusions within peridotite accommodated significant high-temperature deformation, especially within Fe-Ti oxide-bearing assemblages. This deformation spatially localizes in zones of high lithological heterogeneity created by meter-to-submeter-scale gabbroic intrusions within peridotite. High-temperature ductile deformation often localizes close to, and/or along, intrusive contacts, accompanied by localized, evolved, melt-reactive porous flow (crystallizing Fe-Ti oxides), and followed by fluid-rock reaction that enhanced and sustained further ductile deformation. These spatially controlling relationships between magmatism, deformation, and late melt ± fluid infiltration are a direct consequence of the lithological heterogeneity within moderately-magmatic OCCs, which are the dominant style of OCC along the Mid-Atlantic Ridge and other slow-spreading ridges.

TEASER

Lithological heterogeneity controls high-temperature ductile deformation & melt infiltration in the lower lithosphere of MM-OCCs

INTRODUCTION

Mid-ocean ridges are a fundamental component of Earth's plate tectonic system that have been active for at least the last 2 billion years **[1, 2]**. At slow- (50-20 mm/yr, full spreading rate) and ultraslow-spreading (<20 mm/yr) ridges, oceanic core complexes (OCCs) locally accommodate up to 100% asymmetric plate spreading for short periods of time (100's kyr to 1 Myr) and as much as ~40-60% of full plate spreading over geological timescales **[3-5]**. Hydrothermal circulation within OCCs alters the composition and rheology of oceanic lithosphere **[6-8]** and modifies seafloor and ocean chemistry through biogeochemical processes that include H_2-production, C-sequestration, and metal-sulphide mineralization **[7, 9-12]**. Furthermore, OCCs provide an excellent opportunity to sample and study seafloor-exposed rocks that originated from the asthenospheric mantle and lower lithosphere **[1, 13]**. But to fully understand and constrain the controls and impacts of processes stemming from OCCs, we first need to understand the deformation and magmatic processes that control the formation and evolution of OCCs and the resulting lithological and structural architecture that they create.

To address this problem we present the first detailed investigation of the macro-to-microscale character and spatial-temporal distribution of high-temperature deformation processes preserved in rock core from International Ocean Discovery Program (IODP) Hole U1601C on the Atlantis Massif OCC **[14, 15]**. Hole U1601C was drilled during IODP Expedition 399 to a depth of 1267.8 mbsf (meters below sea floor), and represents the most complete and scientifically valuable section of mantle and lower crustal rocks drilled to date from the ocean **[14-16]**. Crucially, the partial extent of serpentinization and the paucity of low-temperature overprints within gabbroic sections in Hole U1601C offers an invaluable opportunity to investigate the high-temperature processes that operate in the lithospheric roots of OCCs, and the impacts of those processes on the formation and evolution of OCCs and their magmatic and hydrothermal systems **[14-16]**. Here, we capitalize on this opportunity, to reveal how lithological heterogeneity created by the magmatic architecture of "moderately-magmatic" OCCs, spatially controls high-temperature ductile deformation, late evolved melt infiltration, and early fluid-rock interaction.

Oceanic Core Complexes and Detachment Faults

OCCs form via deformation-accommodated asymmetric plate spreading, whereby the plate interface is defined by a lithospheric-scale detachment fault. The OCC forms the footwall to the detachment fault, and is characterised by exhumed lower lithospheric and/or asthenospheric rocks, which have been exposed to the seafloor through a combination of uplift, bending, and rotation of the footwall during displacement on the detachment fault **[1, 13, 17-19]**.

A variety of geomorphic and/or litho-structural styles and classifications have been reported for detachment faults and OCCs that highlight differences in the styles of seafloor detachment **[3, 20]**, the volume of magmatism, and bathymetric structure of the footwall **[21-24]**. For clarity, we use the term "detachment fault system" to refer to all styles of detachment fault and their associated footwalls as well as any associated structures within the underlying lithosphere. We use the term "OCC" to refer to detachment fault systems with kilometre-scale domal bathymetric structures and variable proportions and gabbroic and ultramafic footwall rocks **(Fig. 1B-C)**, of which many display a corrugated-seafloor detachment fault **[20, 25, 26]**. OCCs are the dominant style of detachment fault system along the slow-spreading Mid-Atlantic Ridge (MAR) **[26-31]**. They are distinct from "near-amagmatic detachment

systems" (**Fig. 1A**) which dominate along the ultraslow-spreading South West Indian Ridge (SWIR) and Gakkel Ridge (Arctic Ocean), with footwalls almost entirely composed of serpentinized peridotite **[3, 32, 33]**.

Due to the variability of the volume of magmatism and associated extent of magmatic deformation (hyper-solidus strain of a magma during emplacement) observed between OCCs **[e.g., 26, 34]**, we subdivide OCCs into moderately-magmatic and highly-magmatic OCCs (MM-OCCs / HM-OCCs). HM-OCCs (**Fig. 1C**) are dominated by thick gabbroic plutons with comparably minor proportions of mantle rocks. HM-OCCs such as Atlantis Bank (SWIR) and Godzilla (Philippine Sea) form the largest of all detachment fault systems with the largest detachment fault zones by both area and thickness, but their occurrence is rare in comparison to MM-OCCs **[23, 34]**. MM-OCCs (**Fig. 1B**) comprise greater proportions of serpentinized peridotite and variable mafic plutonic and volcanic rocks **[4, 20, 26, 27, 31, 35]**. MM-OCCs such as Atlantis Massif (the focus of our study) are commonly reported from ridge segments with intermediate to low volumes of magmatism (~30-50% magmatic accretion) and are consequently the dominant style of detachment fault system reported from the Atlantic Ocean **[26-31]**.

Deformation processes in detachment fault systems and OCCs

Deformation reported from seafloor-exposed detachment fault surfaces is dominated by hydrothermally-assisted, ductile-to-brittle processes (we use the term "ductile deformation" as describing deformation by dislocation creep and/or diffusion creep) . This style of deformation typifies the "detachment fault zone", which is a ubiquitous feature of all detachment fault systems, comprising strongly altered ultramafic and/or mafic rocks and metasomatic assemblages that deformed at low to intermediate temperatures (approximately ≤400-500 °C) in the middle to upper lithosphere **[6, 31, 36]**. In contrast, observations of higher temperature deformation processes (approximately ≥500-600 °C up to hypersolidus conditions) which take place in the lower lithosphere portions of detachment fault systems are less abundant, in part due to the overprinting nature of later, low-temperature deformation **[37-43]**.

Importantly, high-temperature deformation processes appear to vary with detachment fault system style **[3, 21, 33]**. Near-amagmatic detachment systems and HM-OCCs can be viewed as deformation endmembers, reflecting the impacts of the absence or dominance of magmatism on the character of deformation in the system. Near-amagmatic detachment systems (Fig. 1A) display high-temperature, solid-state deformation of peridotite characterized by dislocation creep with dynamic recrystallization controlling strain localization via grainsize-reduction of olivine **[41]**. HM-OCCs (Fig. 1C) display high-temperature deformation characterized by magmatic deformation (hyper-solidus strain of a magmatic body during emplacement) and melt-present solid-state ductile deformation (solid-state deformation of a solid crystalline framework in presence of a low volume of interstitial melt) of gabbroic intrusions, with strain localization controlled by magmatic intrusions and crystal mush zones **[34, 38]**.

In contrast, the style(s) of deformation which control the lower lithospheric roots of MM-OCCs (Fig. 1B) is unclear. Studies continue to debate the relative importance of hydrothermally-assisted strain localization processes versus magmatic/melt-assisted strain localization processes, especially with respect to lower lithospheric deformation processes in MM-OCCs **[6, 24-27, 37, 39, 40, 44-46]**. This has implications for the vertical and lateral extent of MM-OCC detachment faults (or fault zones), the

depth of magmatic intrusions, hydrothermal alteration fronts **[5, 22, 24, 25, 27, 37, 47, 48]**, and the associated spatial extent of hydrothermal circulation that deformation in MM-OCCs permits **[6, 10, 29, 31, 45, 47].** Constraining the high temperature, lower lithosphere deformation processes that control the formation and evolution of MM-OCCs is therefore fundamental to our understanding of slow-spreading and ultraslow-spreading MORs and the oceanic lithosphere and hydrothermal systems that they create, especially in the Atlantic Ocean where MM-OCCs dominate **[1, 4, 7, 9, 11, 27-30, 39]**.

The Atlantis Massif MM-OCC: Previous work

Located at 30°N on the MAR, the Atlantis Massif MM-OCC covers a 12 x 12 km area on the North American plate, adjacent to the MAR axial valley and the Atlantis transform (**Fig. 2A**). Atlantis Massif is capped by a NNE-SSW-striking, ESE-dipping corrugated seafloor detachment fault that was active between ~0.4-2 Ma **[48-51]**, with a damage zone thickness of ~100-200 m **[6, 8, 40, 45]**. The Central Dome exposes a thick gabbroic intrusion drilled during IODP Expeditions 304/305 and 399 at Site U1309 (**Fig. 2D**) to a sub-seafloor depth of 1489 mbsf **[14, 52, 53]**. To the south, the crest of the Southern Ridge of Atlantis Massif (**Fig. 2A**) exposes serpentinized peridotite, talc-tremolite schist, variably altered mafic to intermediate intrusive rocks, diabase, and calcareous sediments, sampled by seafloor drilling (<17 mbsf) during IODP Expedition 357 **[54]**. Below the ridge, the South Wall exposes variably deformed serpentinized peridotite with an uppermost portion of amphibole-bearing "blackwall" assemblages and meter-thick mafic intrusions observed and sampled by submersible expeditions **[6, 8, 40]**. Footwall rotation of Atlantis Massif is estimated to be ≥60-70°, with 46±6° rotation recorded after exhumation through ~580 °C **[19]**.

Along the Southern Ridge and Wall of Atlantis Massif, Ti-in-zircon thermometry from individual zircon spot analyses **[55]** records crystallization of magmatic veins in altered ultramafic rocks between 919-757 °C (n=25). Across the massif (Southern Ridge and Site U1309), Ti-in-zircon thermometry (individual zircon spot analyses) records magmatic crystallization of gabbro at 799-730 °C (n=12) and of oxide-gabbro and plagiogranite samples at 830-676 °C (n=74). This overlaps with secondary growth and alteration of zircon in the presence of aqueous fluids at 971-658°C (n=33, Grimes et al.'s "Type 3" zircon). Post-magmatic hydrothermal precipitation of zircon from aqueous fluids, interpreted from individual spot analyses of luminescent rims, is recorded at 642-604 °C (n=7) **[55]**.

Previous analyses report a variety of deformation fabrics and features recorded from pyroxene-hornfels/granulite facies temperatures through to albite-epidote hornfels/greenschist facies temperatures **[6, 40, 52, 56]**. At the crest of the South Ridge, deformation observed in drill cores recovered during IODP Expedition 357 (maximum depth of 17 mbsf) is associated with the seafloor detachment fault, dominated by fault breccia and sheared talc-tremolite-chlorite schist; breccia included clasts of reworked amphibolite facies mylonite, cataclasite and fault gouge.

Alvin submersible observations along the South Wall of Atlantis Massif, at ~0-200 m and ~350-500 m below the crest record deformation in variably serpentinized peridotite and meter-scale mafic intrusions **[40]**. High temperature ductile deformation is sparsely distributed across the depth transect, reported from mafic and, to a lesser extent, ultramafic samples, broadly constrained to pyroxene-hornfels/granulite to hornblende-hornfels/amphibolite facies temperatures. Amphibole-plagioclase thermometry and undeformed ilmenite lamellae in magnetite hosted by mylonitized gabbroic rocks indicate ductile deformation temperatures of 900-650°C **[40]**. Lower temperature (≤500°C) semi-

brittle to brittle deformation is concentrated in the uppermost 90 m of the South Wall and includes cataclasis, brecciation, and mylonitization of altered mafic rocks, serpentinite (especially the amphibole-dominated blackwall assemblage), and talc-tremolite schist. The most intense brittle deformation is restricted to the upper 10 m associated with the seafloor detachment fault **[6, 40]**. Serpentinization is interpreted to have occurred at ≤425°C **[6]**. Textures of albite-epidote hornfels/greenschist alteration assemblages appear to be mostly static at hand-sample scale, although deformation of these assemblages is observed at the microscale **[6, 40]**. Serpentine fabrics were initially interpreted as mostly static **[56]**, however, X-ray diffraction analysis has since shown that some serpentinites have a strong lizardite crystallographic preferred orientation suggesting mineral growth during detachment faulting at serpentine-stable conditions **[57]**.

On the Central Dome of Atlantis Massif, IODP Hole U1309D was drilled to 1498 mbsf during Exp 304/305 and 399. The recovered rocks are notable for their paucity of ductile deformation **[26, 45, 53]**. Faulting, brecciation, and cataclasis, at and below albite-epidote hornfels/greenschist facies conditions, characterises deformation in mafic and minor ultramafic intrusive rocks in upper ~170 mbsf, and is interpreted as the seafloor detachment fault zone **[45, 51]**. Intervals hosting ductile deformation account for <3% of the curated core at Site U1309 (**Fig. 2E**) and are localized in the upper ~320 mbsf **[53]**. Where present, protomylonitic to mylonitic intervals typically localize at gabbroic-gabbroic and gabbroic-ultramafic contacts, especially within oxide gabbro and troctolite/troctolitic gabbro intervals, and indicate pyroxene-hornfels/granulite to hornblende-hornfels/amphibolite deformation temperatures (approximately ≥700 °C) **[53]**, consistent with constraints from the Southern Ridge **[40, 55]**. Geospeedometry of olivine-rich troctolites suggest melt-rock reactions began at ~1230°C and continued to segregate into gabbroic intrusions down to ~850°C **[58]**.

IODP Expedition 399 provides a unique record of high-temperature deformation processes from the Atlantis Massif MM-OCC

In this study, we present the first detailed macro-to-microscale structural analysis of high-temperature deformation process recorded throughout the entire length of new rock core from IODP Hole U1601C, drilled from the Atlantis Massif MM-OCC (**Fig. 2**). Hole U1601C was drilled from the Southern Ridge of Atlantis Massif during IODP Expedition 399 (**Fig. 2**). With total core recorvery of >70%, Hole U1601C represents the deepest and most complete section of mantle rocks with gabbroic intrusions drilled from the seafloor **[14-16]**. Below 200 mbsf, the high recovery and structural continuity of this core includes many 10's of meters of ultramafic and mafic cores at 90-100% recovery, allowing for analyses of mantle and mid-ocean ridge-related processes at a resolution and a level of structural context not previously possible.

IODP Expedition 399 shipboard analyses recorded brittle, semi-brittle, and ductile deformation from Hole U1601C **[16]**. Surprisingly, the extent of high-strain brittle to semi-brittle deformation intervals was relatively low in comparison to high-strain ductile intervals **[16]**. Additionally, intervals of medium-to-low temperature ductile deformation (approximately ≤400-500 °C) associated with the seafloor detachment fault zone, as typified by deformed talc-tremolite-chlorite schists reported from IODP Expeditions 304/305 and 357 and Alvin dives **[6, 8, 40, 45, 51, 54]**, were rare to absent across Site U1601 (Holes A and C) **[16]**. Consequently, in this study we focus on the record of high-temperature ductile deformation (approximately ≥500-600 °C up to hypersolidus conditions) recorded

from Hole U1601C. This includes shipboard core analyses of U1601C, supplemented with subsequent post-cruise analyses of the core at the hand-sample to thin-section scale.

Our study provides a detailed synthesis of the macro-to-microscale character and distribution of high-temperature ductile deformation throughout Hole U1601C, which we relate our findings to the structural and magmatic evolution of the Atlantis Massif MM-OCC. Our observations indicate that lithological heterogeneity defined by zones with a high density of meter-scale gabbroic intrusions contacting against peridotite controlled the distribution and localization of high-temperature ductile deformation. That high-temperature ductile deformation preferentially localized in gabbroic intrusions, especially towards gabbroic-ultramafic and gabbroic-gabbroic contacts, and temporally and spatially overlapped with localized late, evolved, melt infiltration and associated Fe-Ti oxide crystallization within gabbroic intervals in the lower lithosphere beneath Atlantis Massif. Furthermore, we show that late evolved melt infiltration followed the spatial distribution of ductile deformation at the margins of mafic intrusions. We suggest that this style of high-temperature lower lithosphere ductile strain localization may be a unique characteristic of MM-OCCs where lithological heterogeneity in the detachment footwall represents a key defining feature of this type of OCC.

RESULTS

Observations from IODP Hole U1601C

Site U1601 **[16]** is located on the corrugated-seafloor detachment surface at the crest of the Southern Ridge (**Fig. 2AB**). Site U1601 lies ~800 m north of the Lost City Hydrothermal Field **[10]**, within ~~20-60 m distance from Hole M0069, 100-300 m distance from M0072, and M0076 (IODP Expedition 357) **[54]**, and 4.7 km due-south of Site U1309 **[53]** (**Fig. 2A**).

At Site U1601, 889.2 m of core was recovered from Hole U1601C between 23.0-1267.8 mbsf (71% recovery). Recovery from the upper 200 mbsf of Hole U1601C is low (44%) compared to rest of the hole (76% recovery below 200 mbsf). The core comprises serpentinized peridotite (68%), mafic intrusive rocks (32%), and rare intermediate intrusive rocks (<1%) (**[16]**, **Fig. 2B**).

Ultramafic rock types recovered in Hole U1601C (67 %) are dominated by variably serpentinized harzburgite, with subordinate dunite and orthopyroxene-bearing dunite, and rare lherzolite. Mafic to intermediate intrusive rock types (**Fig. 2F**) include olivine gabbro (7.5%; includes olivine-bearing gabbro), gabbro (10.1%), disseminated oxide gabbro (0.6%; "disseminated" defined as 1-2% oxide content), oxide gabbro (1.8%; includes oxide-bearing gabbro, oxide gabbronorite, and rare oxide diorite; "oxide-bearing" defined as 2<5% oxide content), disseminated oxide gabbronorite (0.7%), gabbronorite (11.7%), and minor (<1%) of troctolite, diabase, and diorite. These intrusions range in thickness from mm's to 10's of metres and their contacts with ultramafic rocks have dips ranging from 0-90°, but typically >30°(**[15]**; **Fig. S1**). We note that hole-parallel (i.e., sub-vertical) contacts are usually under-sampled by drill core **[59]**, and that dip directions are unconstrained due to rotation of core pieces during recovery. The spatial variability of gabbroic-ultramafic contact dips appears to be random, suggesting that the heterogenous distribution of variably sized gabbroic intrusions represent a net-vein complex (e.g., **[15]**), potentially emanating from larger gabbroic bodies within the Central Dome of the massif to the north (i.e., Hole U1309D) and/or below Hole U1601C **[**e.g., **14]**.

The relative proportion of gabbroic vs ultramafic rock types increases down-hole (**Fig. 2B**) defining 3 domains: Domain 1 - dominantly ultramafic rocks (23-637 mbsf); Domain 2 – variable, but in many places comparable, proportions of gabbroic intrusions within ultramafic rocks (637-950 mbsf); and (3)

Domain 3 dominated by gabbroic intrusions, including 5m- to 80 m-thick intervals of 100% gabbroic rocks with high proportion of gabbronorite (950-1268 mbsf). These domains (**Fig. 2B**) form the broad lithostratigraphic framework for our analysis of ductile deformation in Hole U1601C.

Distribution of ductile deformation in Hole U1601C

We characterize ductile deformation in Hole U1601C based on macroscopic observations of continuous, penetrative deformation fabrics. The distribution and intensity of ductile deformation was recorded during shipboard and post-cruise analyses of macroscale fabrics in core specimens, and microscale fabrics in thin sections. Classification of recovered intervals hosting ductile deformation are based on the macro-scale intensity of solid-state deformation and encompasses dynamic recrystallization by both dislocation and diffusion creep processes (see Materials and Methods section below). Observed ductile deformation intervals account for 8% (79.7 m) of the curated core thickness **(Fig. 2C; Table S1)**. High strain fabrics (protomylonite, mylonite, ultramylonite) account for 61% (48.6 m) of these intervals **(Table S1)**. Recovered zones of ductile deformation are up to 3.8 m thick, some of which concentrate into 10-50 m zones of ductile deformation. Ductile fabric dips vary from 0-90° with a higher proportion of dips between 30-60° (**Fig. S1).** There is no systematic variation in the spatial or lithological distribution of ductile fabric dips, except at intrusive contacts where fabric orientations typically mimic contact orientation (detailed below).

Gabbroic intervals lacking solid-state deformation typically display isotropic magmatic fabrics and occasional grain size and/or modal layering. Intervals of magmatic deformation were rarely observed (0.8% of recovered core). Where present, these formed cm-scale intervals of magmatic foliation defined by aligned plagioclase and are mostly confined to the middle portions of larger gabbroic sections away from contacts (see Lang et al 2025a).

Lithological distribution of ductile deformation

Ductile deformation is concentrated in gabbroic intervals (**Fig. 2G**), accounting for 82% of the observed total ductile deformation in Hole U1601C. These deformed intervals in gabbroic rocks are reported from cm-scale through to >10m-scale intrusive bodies throughout the hole (**Figs. 3 & S2-3**). Many of these deformation intervals are localized along intrusive contacts with peridotite, displaying mylonitic fabrics that are parallel or sub-parallel to contact orientations (**Figs. 3D-E & S4-5**). In Domains 2 and 3, ductile deformation also localizes at intrusive contacts between different gabbroic bodies, most commonly at the margins of oxide-bearing gabbroic intervals (**Figs. 3C & S5**). In some cases, ductile deformation intervals at gabbroic-ultramafic contacts and gabbroic-gabbroic contacts display a strain gradient which increases in strain intensity towards the contact.

Within gabbroic intervals, ductile deformation is partitioned into: gabbro (22%), gabbronorite (23%), oxide gabbro (14%), disseminated oxide gabbro (7%), disseminated oxide gabbronorite (6%), and olivine gabbro (10%) (**Fig. 2G**). Comparing the proportion of ductile deformation in each gabbroic lithology (**Fig. 2G**) to the overall distribution of that lithology throughout Hole U1601C (**Fig. 2F**) highlights a preference for localization in evolved gabbroic compositions over primitive olivine-bearing gabbro. Most notably, oxide-bearing gabbroic compositions show an overwhelming preference for ductile strain localization, accounting for 27% of all ductile intervals, but only 3% of Hole U1601C (**Fig. 2F-G**). This translates to 74% of the total cumulative length of oxide-bearing gabbroic intervals in Hole U1601C displaying ductile deformation fabrics.

The remaining ductile deformation is reported from ultramafic rock types including harzburgite (7%), orthopyroxene-bearing dunite (8%), and dunite (3%), (mostly weak to strong foliations, **Fig 2G**) and rare talc-tremolite schist intervals (<1%). Ductile deformation within ultramafic intervals is almost exclusively restricted to the contacts with deformed gabbroic intrusions (**Fig. S4I-J, M-O**). These intervals form continuums of deformation that transition from the mafic intrusions into the adjacent ultramafic rocks.

Spatial distribution of ductile deformation

Fig. 4 shows the spatial distribution and down-hole length of recovered drill-core intervals hosting ductile deformation alongside rock type. The localization of ductile deformation within gabbroic intrusions and at contacts between gabbroic intrusions and peridotite imparts a strong spatial control on the distribution of deformation. Consequently, 90% of the total ductile deformation in Hole U1601C is recorded in Domains 2 and 3, equating to 15% of the total curated core thickness below 637 mbsf, where the proportion of mafic to ultramafic lithologies is significantly higher.

In Domain 1, (0-637 mbsf) minor zones of ductile deformation are concentrated between 100-200 mbsf where there is also a higher concentration of gabbroic intrusions up to ~10 m (**Fig. 4**). Notably, the low recovery rate in the upper 200m of Hole U1601C may mean that ductile deformation at this depth is underrepresented. In Domain 2 (637-950 mbsf) ductile deformation localizes in mixed gabbroic-ultramafic cores (**Fig. 4,** turquoise cores = 33-66% mafic intervals), and in mantle- or mafic-dominated cores (**Fig. 4**, dark green cores = >66% ultramafic intervals; blue cores = >66% mafic intervals) that are adjacent to mixed gabbroic-ultramafic cores. This reflects the high number of gabbroic-ultramafic contacts which are observed to preferentially localize ductile deformation within these cores. In Domain 3 (950-1268 mbsf), where most cores have >66% mafic intervals (**Fig. 4**, blue cores), ductile deformation localizes at the margins of 5-80 m-thick mafic intervals, and at gabbroic-gabbroic contacts involving oxide-bearing compositions and/or gabbronorite, with little to no record of ductile deformation in their interiors.

High strain zones within Hole U1601C

Six 'high strain zones' (HSZs) characterised by greater concentrations and thicker intervals of ductile deformation (**Fig. 4**), are defined in Hole U1601C. These HSZs are recognized in Domains 2 and 3 between 637 mbsf and 1176 mbsf, have downhole thicknesses of 6-28 m, and are characterized by 31-91% ductile deformation (**Table S3**) (22-83% high strain ductile deformation).

The locations and thicknesses of the HSZs show a spatial correlation with the distribution of gabbroic rocks, which account for 93% of the ductile intervals reported from all six HSZs. But in detail, the mafic lithologic distribution of ductile deformation of each HSZ varies (**Fig. 5, Table S4**). There is a down-hole decrease in the proportion of ultramafic ductile deformation intervals from HSZ 1 (32%), to HSZs 2-3 (11-9%), to HSZs 4-6 (0%), coincident with a down-hole increase in the proportion of evolved mafic ductile deformation intervals (**Fig. 5**). Ductile deformation intervals in olivine gabbro decrease from 19-44% in HSZs 1-3, to 2-0% in HSZs 4-6. In contrast, ductile deformation intervals in evolved gabbroic rocks (oxide gabbro, disseminated oxide gabbro/gabbronorite, and gabbronorite), increases down-hole from 7% in HSZ 1, to 33-48% in HSZs 2 to 4, to 93-100% in HSZs 5 and 6.

The locations of HSZs coincide with notable changes in lithostratigraphy (**Fig. 4**). HSZ 1 is located at the first major increase in the proportion of mafic rocks (**Fig. 4**), after a ~400m-long section dominated

by ultramafic rocks. HSZs 2 and 4 are located in mixed zones of sub-meter to meter-scale gabbroic intrusions of varying composition within ultramafic rocks (**Fig. 4**). HSZs 3, 5 and 6 are located at the boundaries of 20 m- to 80 m-thick gabbroic intervals that also mark the upper boundaries of three distinct gabbronorite bodies dominating core sections at ~975-1025 mbsf and ~1130-1268 mbsf (**Fig. 4**). Notably, in HSZ 5 there is a down-hole increase in the intensity of ductile deformation which also corresponds with a change in composition, from disseminated oxide gabbro to gabbronorite (**Fig. 4**).

Thermal and temporal constraints for ductile deformation in Hole U1601C

The following sections report macro- and microscale observations that provide constraints on the temperature(s) and relative timing of the reported ductile deformation. In part, this is constrained on the basis that detachment fault footwalls cool with time as they exhume towards the seafloor **[50]**. Firstly, we present constraints from the deformation of primary phases which formed early in the footwall's history. This is followed by constraints from the deformation of later secondary phases. Where presented, our temperature estimates are made through comparison of our observations with equivalent microstructural assemblages, petrographic relationships and comparable samples reported in previous studies from Atlantis Massif and other OCCs **[38, 40, 42-44, 60, 61]**.

Ductile deformation of primary mineral phases

In this section we present observations of ductile deformation of primary minerals in gabbroic and ultramafic rocks with the exclusion of deformation of Fe-Ti oxide assemblages. These Fe-Ti oxide assemblages provide a more complex set of observations that warrant more detailed description and interpretation in the subsequent section.

Macroscopic and petrographic observations of high-strain ductile intervals in gabbroic rocks record well-developed mylonitic foliations with localized to pervasive grain size reduction by dynamic recrystallization, and strong grain shape fabrics of primary phases (**Figs. 6, & S2-3**) including plagioclase, orthopyroxene, clinopyroxene, and olivine. Plagioclase domains display strong crystallographic preferred orientation fabrics (**Figs. S2E,H & S3H**). Mylonitic deformation (i.e., ductile deformation with dynamic recrystallization and grain size reduction) of clinopyroxene and orthopyroxene into neoblasts (**Figs. 6A,D & 7B,D**) indicates pyroxene-hornfels/granulite facies deformation temperatures (>800°C e.g., **[38, 42, 43]**).

Dynamic recrystallization of plagioclase includes higher-temperature grain boundary migration and subgrain microstructures in equilibrium with recrystallized pyroxene (**Fig. 6A,D**), and lower-temperature grain boundary bulging microstructures (e.g., **[60]**) in equilibrium with recrystallized secondary amphibole-after-pyroxene (**Figs. 6B, 7B-D & 8F**). These relations indicate mylonitic deformation of plagioclase continued down to hornblende-hornfels/amphibolite facies temperatures (600-500 °C) (e.g., **[60]**). In lower-strain ductile intervals (weakly foliated/strongly foliated), comparable styles of dynamic recrystallization of primary phases are observed albeit with less recrystallization.

Ductile deformation at, and across, intrusive gabbroic-gabbroic contacts displays a variety of relationships that provide relative temporal constraints for the timing of deformation. Rare examples of (1) mylonitic intervals of diabase intruding gabbroic rocks (**Figs. S5AB**); and (2) undeformed microgabbro cutting mylonitic gabbroic rock (**Fig. S5C-E**), indicate that multiple stages of magmatism occurred during and after mylonitic deformation of mafic intervals.

At gabbroic-ultramafic contacts, primary minerals within the gabbroic intervals display contact sub-parallel mylonitic foliations (**Figs. 3D-E, S4**). In most cases, ultramafic assemblages adjacent to these contacts are completely altered to secondary phases (**Figs. 3D, 8C, S4**); however, two samples showed evidence of dynamic recrystallization of olivine, including a grain shape alignment parallel to mylonitic foliation in the adjacent gabbroic interval (**Figs. S4J, O**).

Away from intrusive contacts, rare intervals of coarse-grained ultramafic protomylonite and mylonite are defined by sigmoidal to lozenged shapes orthopyroxene porphyroclasts in a serpentine matrix (**Fig. S6Q-S**). These fabrics were initially interpreted as a record of deformation at asthenospheric conditions **[16, 62]**, however, it is also possible these fabrics formed during ductile deformation in the lowermost lithosphere, where temperatures remain high enough for ductile deformation of peridotite primary phases. A minority of peridotite samples contain primary olivine grains (**Fig. S6E-L**). In most cases, primary olivine grains are subhedral to anhedral, with interlocking grain shapes that do not suggest high temperature ductile deformation of peridotite in the lower lithosphere (**Fig. S6E-L**). Away from contacts, dynamic recrystallization of olivine in peridotite has been observed in one only sample from Hole U1601C. **Schroeder and John [40]** also observed mylonitic deformation of peridotite in one sample collected ~50 m below the top of the Southern Ridge.

Ductile deformation of Fe-Ti oxide assemblages

In oxide-bearing gabbroic intervals, assemblages of magnetite, ilmenite, and rare iron-sulfides display a variety of deformed and undeformed petrographic relationships (**Figs. 3BC, 6C-F, 7B-D, & S3**). Experimental studies demonstrate Fe-Ti oxide assemblages can form through the fractional crystallization of late-stage MORB **[63]**. Textural observations from Atlantis Massif and other detachment fault systems on slow/ultraslow-spreading MORs indicate that these Fe-Ti oxide assemblages typically form as the crystallization products from reactive porous flow of a highly differentiated, evolved melt through pre-existing gabbroic crystal mush rather than through in-situ fractional crystallization (e.g., **[38, 44, 61, 64-66]**). In either case, both explanations indicate that Fe-Ti oxide assemblages reflect a later and lower temperature component of the magmatic system and can thus provide important information on the influence and relative timing of ductile deformation with respect to magmatic evolution.

Fe-Ti oxides in gabbroic intervals of Hole U1601C are spatially associated with zones of ductile deformation at both macro- and micro-scale (**Fig. 4**). Strongly deformed, finer-grained, oxide-rich gabbroic intervals are often juxtaposed against undeformed/less deformed, coarser-grained, gabbro or disseminated oxide gabbro, separated by sheared contacts (**Figs. 3C & 6C**). Mylonitic fabrics in oxide-rich domains typically display a higher intensity of deformation than adjacent oxide-free mylonitic fabrics, indicated by a greater extent of grain size reduction and strong plagioclase and pyroxene grain-shape fabrics and crystallographic fabrics (**Figs. 6C-E & S3H**). Oxide-rich domains form foliation-parallel layers of interconnected Fe-Ti oxide grains within bands of pyroxene and plagioclase neoblasts (**Figs. 6D-E, 7B-D**). In some cases, these plagioclase and pyroxene neoblasts have rounded grain shapes ± cuspate embayments along their grain boundaries, indicating resorption (**Fig. 6D-F, 7BC**). Some Fe-Ti oxide domains form sigmoidal pressure shadows around large pyroxene porphyroclasts (**Figs. 6D, 7B, S7B**). Within silicate-dominated foliation bands isolated, interstitial Fe-Ti oxide grains have irregular cuspate grain shapes and low dihedral grain boundary triple junction angles (**Figs. 7D, S7BC**). This is consistent with precipitation from a low-volume interstitial melt localizing in pore spaces within a solid framework **[38, 44, 61]**. Collectively, these petrographic relationships indicate that in these samples, ductile deformation occurred after and/or during crystallization of Fe-Ti oxides

from a late-stage, evolved melt (note that these observations do not rule out the possibility of deformation also occurring before Fe-Ti oxide crystallization in addition to during/after Fe-Ti oxide crystallization).

In some deformed oxide-bearing samples, temporal relationships can be constrained more tightly:

In zones of lower-strain mylonitic gabbroic rocks, localized zones of dynamically recrystallized plagioclase form along thin Fe-Ti oxide veins (**Fig. S3M**). In these examples, infiltration of the evolved melt has locally promoted further dynamic recrystallization and grain size reduction of plagioclase.

In some mylonitic to ultramylonitic intervals, oxide-rich domains contain multi-grain clasts of plagioclase neoblasts plucked from the Fe-Ti oxide vein walls, which have cuspate embayments produced by resorption into the surrounding melt, and are sometimes folded parallel to the mylonitic foliation (**Figs. 6D-F, 7BD, & S3B,C,O**). The occurrence of these multi-grain clasts of plagioclase neoblasts with resorption microstructures dictates that, at least in the case of these particular samples, mylonitic deformation of plagioclase and pyroxene was already underway before the mm-thick melt bands intruded the rock and crystallized Fe-Ti oxides. The folded nature of multi-grain clasts of recrystalized plagioclase (**Fig. S3O**), along with the presence of sigmoidal Fe-Ti oxide pressure shadows around pyroxene and plagioclase porphyroclasts (**Figs. 6D, S7E**) indicates that ductile deformation continued during and/or after late melt infiltration.

Had the melt bands been present prior to dynamic recrystallization of plagioclase and pyroxene, the weak rheology of the melt and Fe-Ti oxides would have preferentially localized deformation instead of the surrounding silicates solid-framework. Similarly, had the isolated Fe-Ti oxide grains within mylonitized bands of plagioclase crystallized before mylonitic deformation of the plagioclase, they would no longer retain their cuspate, interstitial grain shapes with low dihedral triple junction angles.

Collectively these observations indicate (1) that these Fe-Ti oxide assemblages are the products of reactive porous flow of a late stage evolved melt (e.g., **[38, 44, 61, 64, 65]**); and (2) that ductile deformation and infiltration of this late-stage evolved melt spatially and temporally overlapped. Whether or not deformation continued after these Fe-Ti oxide domains crystallized is not always clear; however, well-formed ilmenite exsolution lamellae within magnetite observed in some samples (**Fig. S7D**) suggest that those grains have not deformed below 600°C (e.g., **[67, 68]**).

Ductile deformation of secondary phases

Gabbroic and ultramafic intervals include a range of secondary alteration assemblages, some of which display ductile deformation fabrics. Within mylonitic gabbroic intervals, amphibole grains display a range of textural relationships with their surrounding ductile deformation fabrics.

Brown amphibole in mafic intervals is often spatially associated with Fe-Ti oxide assemblages and is observed as (1) isolated interstitial grains within a matrix of plagioclase and pyroxene neoblasts (**Fig. S7E**); (2) mantles surrounding pyroxene (**Figs. 7EF & 8A**); and (3) as partial to complete replacements of pyroxene (**Figs. 8B-E**). In some mylonitic and ultramylonitic intervals clinopyroxene neoblasts have mantles of brown amphibole at their edges which form foliation-parallel, sigmoidal pressure shadows (**Figs. 8A & S7F**). The grain distributions and morphologies of these brown amphibole and their spatial association with Fe-Ti oxide assemblages suggest that these examples are likely magmatic in origin and grew as a reaction product during reactive porous flow of a late-infiltrating evolved melt (**[**e.g., **69]**).

A minority of mylonitic gabbroic samples host domains of brown amphibole and ilmenite with interlocking, subhedral, blocky to sub-rounded grain shapes (**Figs. 8B & S3A-D,I-J**). In one example, this amphibole-ilmenite assemblage clearly intrudes a pre-existing mylonitic plagioclase fabric but lacks a deformation fabric of its own (**Fig. S3A-D**). In another example, this amphibole-ilmenite assemblage forms foliation-parallel bands with a weak foliation-parallel grain shape alignment (**Fig. 8B & S3I-J)** whereas pyroxene is completely replaced by brown and green-brown amphibole. Based on these observations, we interpret the amphibole-ilmenite domains as a replacement assemblage of former magnetite + ilmenite + pyroxene domains that are more typically observed in the oxide-bearing gabbroic intervals.

Many of the observed mylonitic gabbroic samples include secondary alteration assemblages that are also deformed as part of the encompassing mylonitic fabric. Assemblages of colourless-to-pale-green-brown amphibole ± minor talc, formed at the expense of pyroxene (typically clinopyroxene), create mylonitic bands with a foliation-parallel grain shape alignment, indicating growth during ductile deformation (**Figs. 3A, 6B, 7A,E-F & 8C-D**). In some samples, olivine porphyroclasts have rims of secondary orthopyroxene and olivine neoblasts which form mylonitic foliation-parallel bands between plagioclase layers (**Figs. 6B, 7A**). Similarly, in some mylonitic gabbroic intervals, secondary overgrowths of colourless-to-pale-green-brown amphibole ± talc, talc veins, and amphibole veins are deformed alongside lower temperature dynamic recrystallization microstructures ± brecciation and cataclasis of plagioclase, including at the contacts between mylonitized mafic and ultramafic intervals (**Fig. 8C-D)**. In some mylonitized mafic intervals, ultrafine (<20 μm) plagioclase and amphibole grains form mm-thick ultramylonitic bands, suggestive of diffusion-controlled, granular flow at amphibole-stable conditions (**Figs. 7F, 8E**).

This colourless-to-pale-green-brown amphibole alteration assemblage is near-ubiquitously observed at gabbroic-ultramafic contacts and commonly displays a mylonitic fabric sub-parallel to the contact (**Figs. 8C-D & S4**). In some instances, the growth of this secondary assemblage is such that the former gabbroic rock and any pre-existing magmatic or mylonitic fabric is completely replaced (**Fig. S4A-H**). At some contacts, this alteration assemblage also replaces parts of the ultramafic rock (**Fig. S4I-J**).

Importantly, not all occurrences of colourless-to-pale-green-brown amphibole are deformed and in some gabbroic samples, undeformed colourless-to-pale-green-brown amphibole veins and talc veins are observed truncating mylonitic fabrics. Lower temperature alteration assemblages are largely undeformed and cut and/or statically overprint mylonitic and undeformed gabbroic intervals alike. Common lower temperature alteration assemblages can include dark green-brown amphibole, chlorite, talc, albite prehnite, zeolite, quartz, and carbonate (**Figs. 8C-E, S4A-B,E-H**). Undeformed chlorite, calcite and serpentine ± magnetite veins are observed cross-cutting gabbroic-ultramafic contacts and mylonitic foliations (**Fig. 8C**). An extensive account of the full range and diversity of alteration assemblages in U1601C is reported in **Lang et. al [16]**.

Summary of deformation temperature estimates

Collectively, the deformation fabrics displayed by (1) brown amphibole, likely to be of late-magmatic origin; and (2) colourless-to-pale-green-brown amphibole ± minor talc assemblages, alongside lower temperature dynamic recrystallization microstructures ± brecciation and cataclasis of plagioclase, indicate that ductile deformation of gabbroic intervals continued as temperatures cooled from pyroxene-hornfels/granulite facies deformation temperatures (>800°C) and melt-present conditions, into subsolidus hornblende-hornfels/amphibolite facies deformation temperatures (≥500-600°C).

Importantly, the undeformed nature of lower temperature alteration phases, and undeformed amphibole veins, talc veins, chlorite veins, and carbonate veins that crosscut mylonitic fabrics, indicate that high-intensity ductile deformation of gabbroic intervals in Hole U1601C is largely absent at and below albite-epidote hornfels/greenschist facies temperatures (≤400-500°C).

DISCUSSION

The impact of serpentinization on the record of high temperature deformation in Hole U1601C

As over 70% of Hole U1601C is ultramafic, it is important to consider the impact of serpentinization on the record of high-temperature ductile deformation in ultramafic intervals. The degree of serpentinization is spatially variable ranging from 100% to as low as ~40% (**Fig. S6**), allowing for some interpretation of the degree of ductile deformation of peridotite prior to serpentinization. Our observations of primary phases in partially serpentinized ultramafic intervals suggest that high-temperature ductile deformation of peridotite was not a significant process in localizing strain in the lower lithosphere of Atlantis Massif. This is consistent with general understanding of the rheological properties of mafic and ultramafic rock types which predicts that at solid-state, high to intermediate temperature conditions (e.g., ~800-1000 ºC to ~500-600ºC), gabbroic intervals should preferentially localize deformation over peridotite **[**e.g., **70]**; similar interpretations have been made from observations of deformed gabbroic intrusions in the moho transition zone of the Oman ophiolite **[70]**. Evidence for melt-present deformation in gabbroic intervals (**Figs. 6D-E & 7D-F)** strengthens this argument further **[e.g., 71, 72]**. We therefore consider gabbroic intrusions and melt-present deformation to be key controlling factors for strain localization in the lower lithosphere of Atlantis Massif, whilst cautiously acknowledging that serpentinization may have overprinted a subordinate component of high-temperature ductile deformation of peridotite.

The spatial, thermal, and temporal evolution of high-temperature ductile deformation in Hole U1601C

Petrographic constraints based on the range of deformed and undeformed mineral assemblages indicate that solid-state ductile deformation of gabbroic intervals occurred broadly from pyroxene-hornfels/granulite temperatures (≥800°C) through hornblende-hornfels/amphibolite facies temperatures (≥500-600°C). This is supported by Ti-in-zircon thermometry and amphibole-plagioclase thermometry from undeformed and deformed gabbroic rocks collected from the Southern Ridge and Wall of Atlantis Massif **[40, 55]**, and consistent with two-pyroxene thermometry and amphibole-plagioclase thermometry from comparably deformed and undeformed gabbroic rocks from Atlantis Bank on the SWIR **[38, 42, 43]**. Observations of magmatic deformation (i.e. hypersolidus strain of a magmatic body during emplacement) are rare and restricted to the centres of the largest gabbroic bodies. It is possible that emplacement of gabbroic intrusions included a component magmatic deformation along their contacts, but if this is the case, then that record of magmatic deformation has been overprinted by subsequent solid-state deformation and hidden from our observations.

The spatial distribution of undeformed, lower-temperature alteration assemblages indicates that ductile deformation within gabbroic intervals at and below albite-epidote hornfels/greenschist facies temperatures (≤400-500°C) was not widespread in U1601C. However, we acknowledge that poor

recovery in the upper 200m of the Hole does not negate the occurrence of medium-to-low temperature ductile deformation associated with the detachment fault zone **[e.g., 6, 8, 45]**).

Ductile deformation is observed in all gabbroic rock types, from primitive olivine gabbro to evolved oxide gabbro, oxide gabbronorite, and gabbronorite (**Fig. 2G**). This includes HSZs 1 to 6 which display the full range of gabbroic lithologies in varying proportions (**Fig. 5**). Consequently, although oxide-bearing gabbroic compositions accommodate the most ductile deformation of all gabbroic lithologies within the HSZs, their presence is not a pre-requisite for ductile deformation and the formation of HSZs. This lithological distribution within HSZ, along with (1) cross-cutting relationships between mylonitic and undeformed gabbroic and diabase intrusions, and (2) the localization of ductile intervals at the boundaries between contrasting compositions of gabbroic rock types, indicate that deformation and magmatism overlapped spatially and temporally during the magmatic evolution of the system; this is most clearly demonstrated by the localization of HSZs 3, 5, and 6 at the boundaries of the 10-60 m-thick gabbronorite bodies in Domain 3 (**Fig. 4**).

Oxide-bearing gabbroic lithologies are clearly the most important rock types for promoting strain localization. Differences in the intensity of mylonitic fabrics across lithological contacts between oxide-bearing and oxide-free compositions (**Figs. 3C & 6C-D**) indicate that the former provide important weak zones that accommodate significantly higher amounts of strain. Within these intervals, Fe-Ti oxide assemblages represent the crystallization products of late-stage evolved melt migrating by reactive porous flow through a pre-existing gabbroic mush/framework, as is commonly observed from lower crustal mid-ocean ridge samples **[38, 44, 61, 64-66, 69]**. Crucially in Hole U1601C, petrographically constrained temporal relationships indicate that mylonitic deformation of the plagioclase solid framework began prior to emplacement of mm-thick melt bands and subsequent Fe-Ti oxide crystallization (**Fig. 6D**). As solid phases, Fe-Ti oxides are weaker than most silicates, including plagioclase, olivine, and pyroxene, and so it is possible that these Fe-Ti oxide assemblages continued to accommodate strain by diffusion and dislocation creep mechanisms down to ~450-500°C **[46, 73]**. Collectively, this implies (1) that most late reactive porous flow followed the distribution of active ductile deformation; and (2) that Fe-Ti oxide crystallization during reactive porous flow subsequently enhanced the degree of ductile strain localization in those locations. This relationship is further supported by (1) microstructural features that we interpret as evidence of melt-present deformation (**Figs. 6D-E & 7B-D**), which are comparable to similar observations and interpretations previously reported for oxide-bearing gabbroic rocks from Atlantis Massif and Atlantis Bank **[38, 44, 61]**; and (2) the spatial distribution of oxide-bearing intervals which are typically at the margins of the HSZs and within deformed sections with significant lithological heterogeneity (**Fig. 4**). This explains why a relatively minor rock type (3% of the recovered core) accommodates the greatest amount of ductile deformation (27% of all ductile intervals throughout Hole U1601C; 44% of all ductile intervals within HSZs) (**Figs. 2F-G & 5**).

With decreasing temperatures to sub-solidus conditions, widespread mylonitic deformation of gabbroic intervals continued in the presence of secondary colourless-to-pale-green-brown amphibole (**Figs. 8A-D & S4**). This is especially prevalent along intrusive contacts between gabbroic and ultramafic rocks, where secondary amphibole accommodates further strain localization contemporaneous with ductile, and later cataclastic deformation of plagioclase (**Figs. 3A, 8C, S4**). Widespread ductile deformation in Hole U1601C is not observed in albite-epidote hornfels/greenschist facies or lower temperature alteration assemblages in gabbroic intervals (**Fig. 8E**), signalling a change in deformation modes and mechanism(s) of strain localization as the footwall continued to cool. As such, our observations indicate that gabbroic intrusions and the lithological heterogeneity they create controlled ductile strain localization during the high-temperature lower lithospheric evolution of the Atlantis Massif footwall.

The lithospheric-scale structure and significance of high-temperature ductile deformation during the evolution of Atlantis Massif

The distribution of ductile deformation in Hole U1601C is summarised in **Fig. 9**. Our observations demonstrate the significance of high-temperature ductile deformation in the lower lithosphere of Atlantis Massif, however, the structural relationship(s) of this deformation to the larger OCC system is less clear. Ductile deformation fabrics located at intrusive contacts between gabbroic and ultramafic rocks typically display contact-parallel orientations, indicating that the meter-scale magmatic architecture of the net-vein complex (Domain 2) and larger intrusive layers (Domain 3) (Fig. 9) control the local orientation of high-temperature ductile deformation, rather than the strain field of the spreading-ridge. Whether or not the magmatic architecture of the system places a similar control on the 3D kilometre-scale structure(s) and orientation(s) of the HSZs is unclear.

Whilst the structural continuity and detail preserved in core recovered from Hole U1601C provides an outstanding record of OCC processes within ultramafic and intrusive gabbroic rocks, we acknowledge that our field of view is restricted with respect to the full structural evolution of the Atlantis Massif OCC. Local-scale variations in deformation kinematics could be explained by strain partitioning, which summates to a consistent and systematic strain-field at a larger scale. Additionally, the strain field and deformation kinematics within the OCC footwall may differ from that of the detachment fault zone and axial ridge **[17, 18]**. These hypotheses remain untested as we currently have no constraint on the local-scale declination or kinematics of high-temperature ductile deformation. This problem is exacerbated further by the unconstrained degree of footwall rotation that must have occurred at Site U1601. Paleomagnetic restoration of Hole U1309D indicates footwall rotation of ≥60-70°, with 46±6° rotation recorded after exhumation through ~580 °C **[19]**. Therefore, the observed high-temperature ductile deformation in Hole U1601C likely occurred prior to footwall rotation (**Fig. 10A**).

Based on these limitations, three viable hypotheses can be proposed to explain the observed deformation in terms of the lithospheric-scale structural evolution of Atlantis Massif:

(1) The lower-lithospheric ductile root of the detachment fault zone **[e.g., 25, 27, 37, 48]**: Whilst conceptually simple, this model does not easily explain why ductile deformation only becomes prominent from ~630 m below the detachment fault surface; one possibility is that high-temperature ductile deformation close to the detachment fault was mostly unrecovered in the upper 200 m of the hole. The small concentration of high-temperature ductile deformation in the upper 200 mbsf, along with high-temperature ductile deformation in gabbroic and peridotite samples collected from the top of the Southern Ridge **[40, 56]** could represent parts of a shallow-depth HSZ coincident with the detachment fault.

(2) Internal deformation of the OCC footwall during exhumation via bending and rotation **[e.g., 17, 18]**: In Hole U1601C the apparent 630 m disconnect between the HSZs and the seafloor detachment surface may indicate that the observed deformation corresponds to a form of internal footwall deformation rather than a higher-temperature component of the detachment fault zone.

(3) Transform-related deformation **[e.g., 28, 30, 34, 74-77]**: Numerical modelling and active seismicity suggest that transform-related deformation contributes to OCCs located on inside corners of ridge-transform intersections **[76, 77]**. However, the exact role or influence of transforms on detachment fault systems remains largely unconstrained **[34, 75]**.

It is possible that more than one and perhaps all of these hypotheses are valid. Future analyses of the paleomagnetic remanence directions combined with borehole imaging datasets **[e.g., 19, 78, 79]** will

provide a vitally important pre- and post-rotation geographic framework with which to test these hypotheses, as well as a valuable opportunity to constrain the orientations of intrusive contacts, serpentine and peridotite fabrics and magmatic flow directions.

The importance of lithological heterogeneity and intrusive contacts for high-temperature ductile deformation, melt infiltration, and fluid flow

Despite the uncertainty of how the observed high-temperature ductile deformation relates to the larger structural architecture of Atlantis Massif, the spatial, temporal, and lithologic distribution of this deformation provide new constraints on the factors that control strain localization in the lower lithosphere of Atlantis Massif. The paucity of ductile deformation towards the centres of gabbro-dominated portions of Hole U1601C (**Fig. 9**) indicates that the volume of gabbroic intrusions is not the only controlling property for ductile strain localization. Rather, our observations demonstrate that strain localization occurs in gabbroic intrusions within zones of high lithological heterogeneity, typically towards and/or along intrusive contacts. This includes zones with high concentrations of meter- and submeter-scale gabbroic intrusions, typifying the net-vein complex structure of Domain 2 (HSZs 1, 2, and 4), or zones at the margins of thicker gabbroic bodies (HSZs 3, 5, and 6) that characterise Domain 3 (**Fig. 9**). We propose that the localization of high-temperature ductile deformation towards the margins of gabbroic intrusions occurs in response to changes in rheological properties as the intrusions cool and crystallize.

This influence of lithological contacts on high-temperature ductile strain localization is highlighted by the distribution of oxide-bearing gabbroic rock types (**Fig. 4**) and loci of significant colourless-to-pale-green-brown amphibole alteration (concentrated at contacts; **Figs. 8C & S4**). This highlights a strong spatial relationship between (1) the location of gabbroic-ultramafic contacts (**Fig. 10C**); (2) the localization of high-temperature ductile strain (**Fig. 10D**); (3) the concentration of late-stage evolved melt infiltration (**Fig. 10E**); and (4) the concentration of fluids which resulted in significant amphibole growth (**Fig. 10F**).

Given the paucity of oxide-bearing intervals at undeformed contacts (**Fig. 4**), we argue that late evolved melt infiltration was drawn towards actively deforming zones close to and along gabbroic-ultramafic, contacts (e.g., **[80]**) during the high-temperature, lower-lithospheric evolution of the Atlantis Massif footwall (**Fig. 10E**). Once localized, the concentration of this late evolved melt then promoted and enhanced further high-temperature strain localization at these contacts (**Fig. 10E**).

The controlling relationships that govern the localization of fluids and associated colourless-to-pale-green-brown amphibole alteration at gabbroic-ultramafic contacts is less certain. This alteration assemblage is found at both deformed and undeformed contacts (**Fig. S4**) suggesting that the presence of the contact has a greater control on the localization of fluids and alteration than the prior localization of deformation. It remains possible that temporally and spatially overlapping deformation could enhance fluid flow and alteration at these contacts (**Fig. 10F**), but this hypothesis requires further investigation.

Importantly, once this scenario is established, this deforming regime has the potential to sustain itself further as melt-rock and fluid-rock interactions create new weak mineral assemblages that continue to deform with decreasing temperature into and through sub-solidus conditions (**Fig. 10E-F**). Furthermore, this scenario naturally creates the conditions required for the eventual localization of the detachment fault within highly altered amphibole-talc assemblages prior to the onset of serpentinization as proposed by **Picazo et. al [37]** for MM-OCCs at 13°N and 14’45°N, MAR.

Lithological heterogeneity and melt-present deformation as controlling factors for lower lithosphere strain localization in MM-OCCs

Our observations from Hole U1601C lead us to hypothesize that lithologic heterogeneity created by high concentrations of meter-scale to submeter-scale gabbroic intrusions within peridotite applies a fundamental control on high-temperature ductile strain localization, late melt infiltration and subsequent fluid flow and alteration in the lower lithosphere of Atlantis Massif (**Fig. 10**). Our hypothesis also provides a reasonable explanation for the paucity of high-temperature ductile deformation reported from Hole U1309D (**Fig. 2D-E**) at the Central Dome of Atlantis Massif **[e.g., 26, 53]**. In that hole, the dominance of gabbroic rocks leads to significantly lower occurrences of gabbroic-ultramafic contacts and thus lower concentrations and less widely distributed intervals of high-temperature ductile deformation (**Fig. 2D-E**). Furthermore, where recorded, the limited occurrences of high-temperature ductile deformation in Hole U1309D are commonly localized at gabbroic-ultramafic contacts and oxide-bearing gabbroic-gabbroic contacts **[53]**. Our proposed mechanism for the localization of high-temperature ductile deformation in Hole U1601C is therefore entirely consistent with observation from Hole U1309D.

The lithologic heterogeneity observed in Hole U1601C (**Fig. 10B**) is, in part, a function of the volume of magmatism during the formation of Atlantis Massif. Consequently, we propose that the controlling relationships between the magmatic architecture of the Atlantis Massif footwall (**Fig. 10B**) and the localization of (1) high-temperature melt-present to subsolidus solid-state ductile deformation (**Fig. 10D**); (2) late evolved melt infiltration (**Fig. 10E**); and (3) fluid flow and amphibole alteration (**Fig. 10F**), are a distinct characteristic of MM-OCCs.

For comparison, drill core from the Atlantis Bank HM-OCC show significantly wider zones of continuous high-temperature ductile deformation and a significantly greater portion of magmatic deformation (which is rarely reported from U1601C), neither of which show a consistent spatial relationship with the recorded lithologic heterogeneity **[34]**. Likewise, in near-amagmatic detachment systems, there are simply not enough gabbroic intrusions for lithological heterogeneity to play an important role, at least with respect to the distribution of gabbroic-ultramafic contacts **[c.f., 33, 41]**.

Recent subsurface tomographic modelling of the Rainbow MM-OCC on the MAR led **Jian et. al [29]** to propose that intrusive contacts beneath OCCs control fluid flow on a lithospheric scale. Our observations from Hole U1601C support this interpretation and suggest that the distribution and kinematics of late melt infiltration and fluid flow may also be distinct between amagmatic detachment systems, MM-OCCs, and HM-OCCs, due to differences in their magmatic architecture. Given the concentration of MM-OCCs within the Atlantic Ocean, and their relative paucity in the SW Indian Ocean and Arctic Ocean, any such differences between OCC-endmember styles may translate into important basin-scale to tectonic plate-scale differences in the composition, hydrology, and rheology of the lower oceanic lithosphere. The findings of our study therefore highlight a potential systematic pathway to (1) constrain lower-lithospheric processes within OCCs, based on their endmember-style (near amagmatic, moderately magmatic, highly magmatic); and (2) to predict or model global variations in the properties of slow/ultraslow-spread oceanic lithosphere, based on the basin-scale distribution of OCC end-member style(s).

MATERIALS AND METHODS

Core analyses

Core from IODP Hole U1601C was recovered during Spring 2023 using the JOIDES Resolution scientific drilling vessel during IODP Expedition 399 and was described by the authors. The science party analysed split cores both at sea and onshore at the IODP core repository at TAMU (College Station, TX). Petrographic observations were made from thin sections cut from core pieces during the expedition and subsequently during post-expedition analyses.

Intervals of ductile deformation were reported from core observations during core description. Interval thicknesses were reported and measured from the down-hole drilled thickness, and do not consider the dip of the ductile fabrics. Ductile deformation intervals were ranked qualitatively from 1 to 5 in terms of deformation intensity, defined as (1) weakly foliated; (2) strongly foliated; (3) protomylonite; (4) mylonite; (5) ultramylonite. Ranks 3 to 5 are defined based on the amount of recrystallized mylonitic matrix versus porphyroclasts, whereby protomylonite = 10-50% recrystallized matrix; mylonite = 50-90% recrystallized matrix; ultramylonite = >90% recrystallized matrix. Ranks (1) and (2) are classed as 'low strain', whereas ranks (3) to (5) are classed as 'high strain'. This excludes coarse-grained protogranular and porphyroblastic fabrics created by pyroxene (or bastite) within peridotite (or serpentinite) which were classified and reported separately as mantle fabrics during shipboard analyses and generally interpreted to have formed at asthenospheric conditions **[62]**. Further details of the analytical procedures used in this study with a detailed record of all observations and shipboard data collected during Expedition 399 are presented in the Expedition 399 Proceedings **[16, 62]**.

Note that the term "ductile" deformation in this study, is referred to in the original ship-based analyses as "crystal plastic" deformation **[16, 62]**. We have made this change in recognition of the fact some of our reported mylonitic fabrics formed by diffusion-controlled processes that lack a threshold yield stress (i.e., not plastic). "Ductile deformation" is therefore a more appropriate term that accounts for mylonitic fabrics produced by both crystal plastic and diffusive deformation processes.

Electron Microscopy

Back-scatter electron (BSE) images and electron-dispersive spectroscopy (EDS) spot analyses and EDS-element maps were recorded from thin sections using the JEOL IT800 Field Emission scanning electron microscope operated at 20 keV at the Plymouth Electron Microscopy Centre (PEMC), University of Plymouth, UK. EDS spot analyses and element maps were collected using the Oxford Instruments Ultimax 65 mm^2 EDX detector. Oxford Instruments Aztec 6.1 software was used for data acquisition and processing including final output of BSE-element map montages.

ACKNOWLEDGEMENTS

Acknowledgments: We would like to thank the captain and crew of the *JOIDES Resolution* for their dedicated work in making Expedition 399 a success. IODP staff at Texas A&M University are thanked for their efforts to (re)image and (re)curate the cores, and for organizing the post-cruise core description workshop. AP thanks Michelle Harris, Benoit Ildefonse and Catriona McCleary for helpful discussion during write up.

Funding: This research used samples and data provided by the International Ocean Discovery Program (IODP). Funding for the operation and management of the scientific drilling vessel JOIDES Resolution was provided by the U.S. National Science Foundation (NSF) award OCE – 1326927. Funding to join Expedition 399 was provided by UK Natural Environment Research Council grants NE/Y002350/1 and NE/Z000424/1 (AJP), NE/Y001737/1 (AMM), NE/X019098/1 (CJL), and NE/Y002415/1 (IPS); NSF grant OCE-1450528

for the U.S. Science Support Program Office associated with the International Ocean Discovery Program (USSSP-IODP Subcontract # 2O(GG009393-04) (SQL, MKR, JRD, FK, BEJ, ELL, WJB, KLD, JAR, K-YL), Juan de la Cierva fellowship FJC2021-047190-I (RC) funded by the Spanish Ministerio de Ciencia e Innovacion and the Agencia Estatal de Investigacion (MCIN/AEI/10.13039/501100011033); IODP France (RC, OJS, MG); IFPEN Project XBT01 (OJS); IODP Switzerland, funded by the Swiss National Science Foundation (ES); ANR Institut National des Sciences de l'Univers-CNRS grant ANR-22-EXOR-0001 Origins (MG); National Natural Science Foundation of China grant 42373003 (HL); Japan Society for the Promotion of Science grant KAKENHI 23K0352805 (TN), IODP-China Office and Natural Science Foundation of China grant 92251303 (FW); IODP Germany and DFG grant 546935067 (RK), J DESC (Japan Drilling Earth Science Consortium; NA), and National Centre for Polar and Ocean Research, Ministry of Earth Sciences, Government of India (VP).

REFERENCES

1. Escartín, J. and J.A. Olive, *8.31 - Mid-Ocean Ridges and Their Geomorphological Features*, in *Treatise on Geomorphology (Second Edition)*, J.F. Shroder, Editor. 2022, Academic Press: Oxford. p. 847-881.
2. Palin, R.M., et al. (2020) *Secular change and the onset of plate tectonics on Earth.* Earth-Science Reviews. **207**: p. 103172.
3. Cannat, M., et al. (2006) *Modes of seafloor generation at a melt-poor ultraslow-spreading ridge.* Geology. **34**(7): p. 605-608.
4. Escartín, J., et al. (2008) *Central role of detachment faults in accretion of slow-spreading oceanic lithosphere.* Nature. **455**(7214): p. 790-794.
5. John, B.E. and M.J. Cheadle, *Deformation and Alteration Associated With Oceanic And Continental Detachment Fault Systems: Are They Similar?*, in *Diversity Of Hydrothermal Systems On Slow Spreading Ocean Ridges*. 2010. p. 175-205.
6. Boschi, C., et al. (2006) *Mass transfer and fluid flow during detachment faulting and development of an oceanic core complex, Atlantis Massif (MAR 30°N).* Geochemistry, Geophysics, Geosystems. **7**(1).
7. Früh-Green, G.L., et al. (2022) *Diversity of magmatism, hydrothermal processes and microbial interactions at mid-ocean ridges.* Nature Reviews Earth & Environment. **3**(12): p. 852-871.
8. Karson, J.A., et al. (2006) *Detachment shear zone of the Atlantis Massif core complex, Mid-Atlantic Ridge, 30°N.* Geochemistry, Geophysics, Geosystems. **7**(6).
9. Alt, J.C., et al. (2013) *The role of serpentinites in cycling of carbon and sulfur: Seafloor serpentinization and subduction metamorphism.* Lithos. **178**: p. 40-54.
10. Kelley, D.S., et al. (2001) *An off-axis hydrothermal vent field near the Mid-Atlantic Ridge at 30° N.* Nature. **412**(6843): p. 145-149.
11. Schrenk, M.O., W.J. Brazelton, and S.Q. Lang. (2013) *Serpentinization, Carbon, and Deep Life.* Reviews in Mineralogy and Geochemistry. **75**(1): p. 575-606.
12. Lang, S.Q., et al. (2025) *Hydrogen, single-carbon compounds, and thermal regime in the oceanic ultramafic-dominated lithosphere: insights from a deep borehole on the Atlantis Massif.* Geochimica et Cosmochimica Acta. **408**: p. 84-104.
13. Cannat, M. (1993) *Emplacement of mantle rocks in the seafloor at mid-ocean ridges.* Journal of Geophysical Research: Solid Earth. **98**(B3): p. 4163-4172.
14. McCaig, A.M., et al., *Expedition 399 summary*, in *Building Blocks of Life, Atlantis Massif*, A.M. McCaig, et al., Editors. 2025, International Ocean Discovery Program: College Station, TX.
15. Lissenberg, C.J., et al. (2024) *A long section of serpentinized depleted mantle peridotite.* Science. **385**(6709): p. 623-629.
16. Lang, S.Q., et al., *Site U1601*, in *Building Blocks of Life, Atlantis Massif*, A.M. McCaig, et al., Editors. 2025, International Ocean Discovery Program: College Station, TX.
17. Parnell-Turner, R., et al. (2017) *Oceanic detachment faults generate compression in extension.* Geology. **45**(10): p. 923-926.

18. Jackson, J. and D. McKenzie. (2023) *Reverse-faulting earthquakes and the tectonics of slowly-spreading mid-ocean ridge axes.* Earth and Planetary Science Letters. **618**: p. 118279.
19. Morris, A., et al. (2009) *Footwall rotation in an oceanic core complex quantified using reoriented Integrated Ocean Drilling Program core samples.* Earth and Planetary Science Letters. **287**(1): p. 217-228.
20. Cannat, M., et al. (2009) *Oceanic corrugated surfaces and the strength of the axial lithosphere at slow spreading ridges.* Earth and Planetary Science Letters. **288**(1): p. 174-183.
21. Howell, S.M., et al. (2019) *Seafloor expression of oceanic detachment faulting reflects gradients in mid-ocean ridge magma supply.* Earth and Planetary Science Letters. **516**: p. 176-189.
22. Tucholke, B.E., J. Lin, and M.C. Kleinrock. (1998) *Megamullions and mullion structure defining oceanic metamorphic core complexes on the Mid-Atlantic Ridge.* Journal of Geophysical Research: Solid Earth. **103**(B5): p. 9857-9866.
23. Ohara, Y., et al. (2001) *Giant megamullion in the Parece Vela backarc basin.* Marine Geophysical Researches. **22**(1): p. 47-61.
24. MacLeod, C.J., et al. (2009) *Life cycle of oceanic core complexes.* Earth and Planetary Science Letters. **287**(3): p. 333-344.
25. Escartín, J., et al. (2003) *Constraints on deformation conditions and the origin of oceanic detachments: The Mid-Atlantic Ridge core complex at 15°45′N.* Geochemistry, Geophysics, Geosystems. **4**(8).
26. Ildefonse, B., et al. (2007) *Oceanic core complexes and crustal accretion at slow-spreading ridges.* Geology. **35**(7): p. 623-626.
27. MacLeod, C.J., et al. (2002) *Direct geological evidence for oceanic detachment faulting: The Mid-Atlantic Ridge, 15°45′N.* Geology. **30**(10): p. 879-882.
28. Cannat, M., et al. (1997) *Drilling tectonic windows into the lower crust and upper mantle: ODP leg 153.* JOIDES Journal. **23**(1): p. 14-15.
29. Jian, H., et al. (2024) *Hydrothermal flow and serpentinization in oceanic core complexes controlled by mafic intrusions.* Nature Geoscience. **17**(6): p. 566-571.
30. Reston, T.J., et al. (2002) *A rifted inside corner massif on the Mid-Atlantic Ridge at 5°S.* Earth and Planetary Science Letters. **200**(3): p. 255-269.
31. Escartín, J., et al. (2017) *Tectonic structure, evolution, and the nature of oceanic core complexes and their detachment fault zones (13°20′N and 13°30′N, Mid Atlantic Ridge).* Geochemistry, Geophysics, Geosystems. **18**(4): p. 1451-1482.
32. Michael, P.J., et al. (2003) *Magmatic and amagmatic seafloor generation at the ultraslow-spreading Gakkel ridge, Arctic Ocean.* Nature. **423**(6943): p. 956-961.
33. Bickert, M., L. Lavier, and M. Cannat. (2020) *How do detachment faults form at ultraslow mid-ocean ridges in a thick axial lithosphere?* Earth and Planetary Science Letters. **533**: p. 116048.
34. Dick, H.J.B., et al. (2019) *Dynamic Accretion Beneath a Slow-Spreading Ridge Segment: IODP Hole 1473A and the Atlantis Bank Oceanic Core Complex.* Journal of Geophysical Research: Solid Earth. **124**(12): p. 12631-12659.
35. Mahato, S. and M. Cannat. (2025) *Footwall Geology and Deformation at Flip-Flop Mid-Ocean Ridge Detachment Faults: 64°35′E Southwest Indian Ridge (SWIR).* Geochemistry, Geophysics, Geosystems. **26**(1): p. e2024GC011769.
36. Bonnemains, D., et al. (2017) *Pervasive silicification and hanging wall overplating along the 13°20′N oceanic detachment fault (Mid-Atlantic Ridge).* Geochemistry, Geophysics, Geosystems. **18**(6): p. 2028-2053.
37. Picazo, S., et al. (2012) *Deformation associated with the denudation of mantle-derived rocks at the Mid-Atlantic Ridge 13°–15°N: The role of magmatic injections and hydrothermal alteration.* Geochemistry, Geophysics, Geosystems. **13**(9).
38. Gardner, R.L., et al. (2020) *Microstructures reveal multistage melt present strain localisation in mid-ocean gabbros.* Lithos. **366-367**: p. 105572.
39. Casini, L., et al. (2021) *High-Temperature Strain Localization and the Nucleation of Oceanic Core Complexes (16.5°N, Mid-Atlantic Ridge).* Journal of Geophysical Research: Solid Earth. **126**(9): p. e2021JB022215.

40. Schroeder, T. and B.E. John. (2004) *Strain localization on an oceanic detachment fault system, Atlantis Massif, 30°N, Mid-Atlantic Ridge.* Geochemistry, Geophysics, Geosystems. **5**(11).
41. Bickert, M., et al. (2021) *Strain Localization in the Root of Detachment Faults at a Melt-Starved Mid-Ocean Ridge: A Microstructural Study of Abyssal Peridotites From the Southwest Indian Ridge.* Geochemistry, Geophysics, Geosystems. **22**(5): p. e2020GC009434.
42. Mehl, L. and G. Hirth. (2008) *Plagioclase preferred orientation in layered mylonites: Evaluation of flow laws for the lower crust.* Journal of Geophysical Research: Solid Earth. **113**(B5).
43. Miranda, E.A. and B.E. John. (2010) *Strain localization along the Atlantis Bank oceanic detachment fault system, Southwest Indian Ridge.* Geochemistry, Geophysics, Geosystems. **11**(4).
44. Gardner, R.L., N.R. Daczko, and S. Piazolo. (2023) *The critical role of deformation-assisted melt migration in the formation of oceanic core complexes.* Australian Journal of Earth Sciences: p. 1-21.
45. McCaig, A.M., et al., *Detachment Fault Control on Hydrothermal Circulation Systems: Interpreting the Subsurface Beneath The Tag Hydrothermal Field Using The Isotopic and Geological Evolution of Oceanic Core Complexes in The Atlantic*, in *Diversity Of Hydrothermal Systems On Slow Spreading Ocean Ridges*. 2010. p. 207-239.
46. Agar, S.M. and G.E. Lloyd. *Deformation of Fe-Ti oxides in gabbroic shear zones from the MARK area*. in *Proceedings-Ocean Drilling Program Scientific Results*. 1997. National Science Foundation.
47. deMartin, B.J., et al. (2007) *Kinematics and geometry of active detachment faulting beneath the Trans-Atlantic Geotraverse (TAG) hydrothermal field on the Mid-Atlantic Ridge.* Geology. **35**(8): p. 711-714.
48. Schoolmeesters, N., et al. (2012) *The cooling history and the depth of detachment faulting at the Atlantis Massif oceanic core complex.* Geochemistry, Geophysics, Geosystems. **13**(10).
49. Escartín, J., et al. (2022) *Tectonic termination of oceanic detachment faults, with constraints on tectonic uplift and mass wasting related erosion rates.* Earth and Planetary Science Letters. **584**: p. 117449.
50. Grimes, C.B., et al. (2011) *Cooling rates and the depth of detachment faulting at oceanic core complexes: Evidence from zircon Pb/U and (U-Th)/He ages.* Geochemistry, Geophysics, Geosystems. **12**(3).
51. McCaig, A.M. and M. Harris. (2012) *Hydrothermal circulation and the dike-gabbro transition in the detachment mode of slow seafloor spreading.* Geology. **40**(4): p. 367-370.
52. Blackman, D.K., et al. (2011) *Drilling constraints on lithospheric accretion and evolution at Atlantis Massif, Mid-Atlantic Ridge 30°N.* Journal of Geophysical Research: Solid Earth. **116**(B7).
53. Blackman, D., et al., *Proceedings of the Integrated Ocean Drilling Program volume 304/305*. 2006: IODP.
54. Früh-Green, G.L., et al. (2016) *Expedition 357 preliminary report: Atlantis Massif serpentinization and life.* International Ocean Discovery Program.
55. Grimes, C.B., et al. (2009) *On the occurrence, trace element geochemistry, and crystallization history of zircon from in situ ocean lithosphere.* Contributions to Mineralogy and Petrology. **158**(6): p. 757-783.
56. Früh-Green, G.L., et al. (2018) *Magmatism, serpentinization and life: Insights through drilling the Atlantis Massif (IODP Expedition 357).* Lithos. **323**: p. 137-155.
57. Kuehn, R., et al. (2021) *Deformation, CPO, and Elastic Anisotropy in Low-Grade Metamorphic Serpentinites, Atlantis Massif Oceanic Core Complex.* Geophysical Research Letters. **48**(8): p. e2021GL092986.
58. Ferrando, C., et al. (2020) *Retrieving timescales of oceanic crustal evolution at Oceanic Core Complexes: Insights from diffusion modelling of geochemical profiles in olivine.* Lithos. **376-377**: p. 105727.
59. Martel, S.J. (1999) *Analysis of fracture orientation data from boreholes.* Environmental & Engineering Geoscience(2): p. 213-233.
60. Allard, M., et al. (2021) *Plastic Deformation of Plagioclase in Oceanic Gabbro Accreted at a Slow-Spreading Ridge (Hole U1473A, Atlantis Bank, Southwest Indian Ridge).* Journal of Geophysical Research: Solid Earth. **126**(10): p. e2021JB021964.
61. Ghatak, H., et al. (2022) *Oxide enrichment by syntectonic melt-rock interaction.* Lithos. **414-415**: p. 106617.
62. Lang, S.Q., et al., *Expedition 399 methods*, in *Building Blocks of Life, Atlantis Massif*, A.M. McCaig, et al., Editors. 2025, International Ocean Discovery Program: College Station, TX.

63. Koepke, J., R.E. Botcharnikov, and J.H. Natland. (2018) *Crystallization of late-stage MORB under varying water activities and redox conditions: Implications for the formation of highly evolved lavas and oxide gabbro in the ocean crust.* Lithos. **323**: p. 58-77.
64. Lissenberg, C.J. and C.J. MacLeod. (2016) *A Reactive Porous Flow Control on Mid-ocean Ridge Magmatic Evolution.* Journal of Petrology. **57**(11-12): p. 2195-2220.
65. Sanfilippo, A., et al. (2020) *Early-Stage Melt-Rock Reaction in a Cooling Crystal Mush Beneath a Slow-Spreading Mid-Ocean Ridge (IODP Hole U1473A, Atlantis Bank, Southwest Indian Ridge).* Frontiers in Earth Science. **8**(473).
66. Basch, V., et al. (2022) *Genesis of Oceanic Oxide Gabbros and Gabbronorites During Reactive Melt Migration at Transform Walls (Doldrums Megatransform System; 7–8°N Mid-Atlantic Ridge).* Journal of Petrology. **63**(9).
67. Buddington, A.F. and D.H. Lindsely. (1964) *Iron-Titanium Oxide Minerals and Synthetic Equivalents.* Journal of Petrology. **5**(2): p. 310-357.
68. Tan, W., et al. (2016) *Mineralogy and Origin of Exsolution in Ti-rich Magnetite from Different Magmatic Fe-ti Oxide-bearing Intrusions.* The Canadian Mineralogist. **54**(3): p. 539-553.
69. Ferrando, C., et al. (2022) *Brown Amphibole as Tracer of Tectono-Magmatic Evolution of the Atlantis Bank Oceanic Core Complex (IODP Hole U1473A).* Journal of Petrology. **63**(9).
70. Homburg, J.M., G. Hirth, and P.B. Kelemen. (2010) *Investigation of the strength contrast at the Moho: A case study from the Oman Ophiolite.* Geology. **38**(8): p. 679-682.
71. Renner, J., B. Evans, and G. Hirth. (2000) *On the rheologically critical melt fraction.* Earth and Planetary Science Letters. **181**(4): p. 585-594.
72. Rosenberg, C.L. and M.R. Handy. (2005) *Experimental deformation of partially melted granite revisited: implications for the continental crust.* Journal of Metamorphic Geology. **23**(1): p. 19-28.
73. Till, J.L., et al. (2019) *High-Temperature Deformation Behavior of Synthetic Polycrystalline Magnetite.* Journal of Geophysical Research: Solid Earth. **124**(3): p. 2378-2394.
74. Bialas, J., A. Dannowski, and T.J. Reston. (2015) *Interplay between magmatic accretion, spreading asymmetry and detachment faulting at a segment end: Crustal structure south of the Ascension Fracture Zone.* Earth and Planetary Science Letters. **432**: p. 84-94.
75. Ghose, I., M. Cannat, and M. Seyler. (1996) *Transform fault effect on mantle melting in the MARK area (Mid-Atlantic Ridge south of the Kane transform).* Geology. **24**(12): p. 1139-1142.
76. Collins, J.A., D.K. Smith, and J.J. McGuire. (2012) *Seismicity of the Atlantis Massif detachment fault, 30°N at the Mid-Atlantic Ridge.* Geochemistry, Geophysics, Geosystems. **13**(10).
77. Schierjott, J.C., et al. (2023) *How transform fault shear influences where detachment faults form near mid-ocean ridges.* Scientific Reports. **13**(1): p. 9259.
78. Pressling, N., et al. (2012) *The internal structure of an oceanic core complex: An integrated analysis of oriented borehole imagery from IODP Hole U1309D (Atlantis Massif).* Geochemistry, Geophysics, Geosystems. **13**(9).
79. Deans, J.R.L. and A.S. Yoshinobu. (2019) *Geographically re-oriented magmatic and metamorphic foliations from ODP Hole 735B Atlantis Bank, Southwest Indian Ridge: Magmatic intrusion and crystal-plastic overprint in the footwall of an oceanic core complex.* Journal of Structural Geology. **126**: p. 1-10.
80. Petford, N., M.A. Koenders, and J.D. Clemens. (2020) *Igneous differentiation by deformation.* Contributions to Mineralogy and Petrology. **175**(5): p. 45.

Figure Captions

Fig. 1. Schematic cartoons depicting our classifications for (A) Near-Amagmatic Detachment Fault Systems; (B) Moderately-Magmatic Oceanic Core Complexes (MM-OCCs); and (C) Highly-Magmatic Oceanic Core Complexes (HM-OCCs). Previous classifications used to describe these models are shown, along with specific examples for each classification. MAR – Mid-Atlantic Ridge; PSP – Philippine Sea Plate; SWIR – South West Indian Ridge.

Fig. 2. The Atlantis Massif OCC. (A) Bathymetric map of Atlantis Massif with locations of IODP Holes U1601C and U1309D, the Lost City Hydrothermal Field (LCHF), and the location Meg4 seismic line **[14, 16]**. (B) Recovered lithologies from Hole U1601C (10 m running average) **[**after **15]** showing locations of Domains 1 to 3. (C) U1601C Ductile deformation intensity rank (see methods for explanation). (D-E) Recovered lithologies from Hole U1309D (20 m running average) and U1309D ductile deformation intensity rank (see methods for explanation) **[after 15, 53]**. (F) Percentage distribution of lithologies throughout Hole U1601C. (G) Percentage distribution of lithologies in ductile deformation intervals in Hole U1601C **[**from **15]**. Data presented in (B), (C), (F), and (G) is listed in **Data S1**.

Fig. 3. Core photographs of representative mylonitic deformation in gabbroic intervals and at gabbroic-ultramafic contacts. (A) Ultramylonitic gabbro. Brown colouration due to secondary amphibole. Talc veins are sheared at bottom of sample. Undeformed talc veins crosscut mylonitic foliation (U1601C-134R-2W 110-114cm; ~666mbsf). (B) Protomylonitic to mylonitic oxide-bearing gabbro (U1601C-176R-1W 81-90cm; ~867mbsf). (C) Mylonitic to ultramylonitic oxide gabbro and gabbro. Deformation is preferential localized within oxide gabbro (U1601C-130R-4A 30-45cm; ~643mbsf). (D) Mylonitic deformation across contact between serpentinized harzburgite and gabbro with static alteration (amphibole, talc, chlorite) overprinting the gabbro (U1601C-129R-3A 67-73cm; ~642mbsf; see **Fig. S4J** for photomicrograph of contact). (E) Mylonitic deformation across contact between serpentinized harzburgite and olivine gabbro (U1601C-178R-2W 15-22cm; ~876mbsf).

Fig. 4. Downhole distribution of lithospheric ductile deformation intervals grouped as Low Strain Ductile Deformation (grey bars; weak foliation, strong foliation) and High Strain Ductile Deformation (black bars; protomylonite, mylonite, ultramylonite). Core lithologies are displayed as a function of proportion of mafic to ultramafic lithologies per core, grouped as (1) >66% ultramafic (dark green); (2) 33% to 66% mafic and 33% to 66% ultramafic (teal); (3) >66% mafic (blue). Discrete lithology intervals (i.e. not grouped) are shown to the right of each column; oxide-bearing intervals shown protruding outwards from the right side of each discrete lithology column. Colourless sections show zones of no recovery. Depth distribution of Domains 1 to 3, ductile high strain zones (HSZs) 1 to 6, and the shallow mylonite zone are shown.

Fig. 5. (A-F) Pie charts showing the lithology distribution (%) of ductile intervals reported from HSZs 1 to 6.

Fig. 6. Photomicrographs of ductile deformation fabrics. (A) U1601C-258R-1, 82-86 cm (TS273 – 1259 mbsf): Gabbronorite protomylonite showing dynamic recrystallization and grainsize reduction of plagioclase, orthopyroxene, and clinopyroxene. (B) U1601C-131R-1, 43-46 cm (TS80 – 649 mbsf): Olivine-bearing gabbro mylonite showing dynamic recrystallization and grainsize reduction of plagioclase, olivine, and clinopyroxene. Plagioclase microstructure is indicative of lower temperature dynamic recrystallization. Secondary amphibole after clinopyroxene and secondary orthopyroxene after olivine, are also deformed within the mylonitic foliation (**see Fig. S7A** for SEM image). (C) U1601C-206R-1, 35-38 cm (TS120 – 1013 mbsf): Oxide gabbronorite ultramylonite (top right) in sheared contact with gabbronorite protomylonite. (D) U1601C-159R-3, 29-32 cm (TS99 – 788 mbsf): Oxide gabbronorite ultramylonite. Multigrain clasts of plagioclase neoblasts in Fe-Ti oxide vein (white arrowheads) and Fe-Ti oxide strain shadows on pyroxene porphyroclasts indicate deformation occurred prior to and during late melt intrusion. White box shows location of 6E. Yellow box shows area of SEM image in **Fig. 7B**. (E) Zoomed in portion of 6D (white box) showing resorption microstructures and rounded pyroxene grains (yellow arrowheads) suspended in Fe-Ti oxide matrix due to melt-rock reaction during melt-reactive porous flow of a late evolved melt. (F) U1601C-211R-1, 52-55 cm (TS121 – 1037 mbsf): Oxide gabbronorite protomylonite. Thick and irregular shape of Fe-Ti oxide intrusion indicates intrusion occurred after deformation. Yellow arrowheads show resorption microstructures due to melt-rock reaction (same as 6D and 6E). Abbreviations: amp – amphibole; cb – carbonate; chl – chlorite; cpx – clinopyroxene; il – ilmenite; mg – magnetite; opx – orthopyroxene; ox – Fe-Ti oxide (undetermined); pl – plagioclase; px – pyroxene; S – iron sulfide; sp – serpentine; tl – talc.

Fig. 7. Back scatter electron (BSE) plus electron dispersive spectroscopy (EDS) element map montage images of melt-present ductile deformation fabrics and alteration assemblages. Grey scale BSE images show distribution of elementally heavy (bright) vs. elementally light (dark) minerals. Colour image overlays are layered images of Mg (green), Ca (purple), Al (blue), Na (turquoise), Ti (red), and S (yellow) EDS element maps. (A) U1601C-131R-1, 43-46 cm (TS80 – 649 mbsf): Olivine-bearing gabbro mylonite. Olivine (light green) porphyroclasts are recrystallised to olivine neoblasts and secondary orthopyroxene (dark green). Clinopyroxene (pink) neoblasts form clast within dynamically recrystallized secondary amphibole (turquoise). Plagioclase (blue-to-indigo) rims (white arrowheads) show enrichment in Na relative to Al and Ca. (B) U1601C-159R-3, 29-32 cm (TS99 – 788 mbsf): Oxide gabbronorite ultramylonite showing clinopyroxene porphyroclasts (lower left) with a mylonitized pressure shadow of clinopyroxene (purple) and orthopyroxene (green) neoblasts and interstitial ilmenite (pale red), magnetite (white), and iron sulfide (yellow). SEM image location shown in **Fig. 6D** (yellow box). (C) Same sample as 7B showing Fe-Ti oxide domains of ilmenite (purple), magnetite (white), and rare Fe-sulfide (yellow) forming a pseudomorph of melt containing isolated neoblasts of clinopyroxene (green) and plagioclase (blue). Interstitial secondary amphibole (turquoise – black arrowheads) forms melt-pseudomorphs between plagioclase neoblasts. (D) U1601C-206R-1, 35-38 cm (TS120 – 1013 mbsf): Oxide gabbronorite ultramylonite showing interstitial ilmenite (pink) and magnetite (white) forming melt-pseudomorphs with low dihedral grain boundary triple junction (black arrowheads) angles between plagioclase (blue), clinopyroxene (purple), and orthopyroxene (green) neoblasts. (E) Same sample as 7A, showing dynamically recrystallized secondary amphibole (turquoise) with a foliation-parallel grain shape alignment (black double-headed arrows), indicating growth during mylonitic deformation. (F) U1601C-133R-1, 19-22 cm (TS85 – 689 mbsf): Gabbro

mylonite showing ultramylonitic granular flow band with dynamically recrystallized plagioclase (blue) and amphibole (green). Mineral abbreviations are listed in Fig. 6. caption.

Fig. 8. Photomicrographs of secondary mineral assemblages. (A) U1601C-133R-1, 19-22 cm (TS85 – 689 mbsf): Gabbro mylonite showing foliation-parallel, wing-shaped pressure shadows of secondary brown amphibole mantling clinopyroxene neoblasts (black arrowheads). SEM image of central clinopyroxene neoblast is shown in **Fig. S7F**. (B) U1601C-163R-1, 33-36 cm (TS101 – 804 mbsf): Gabbro mylonite showing brown amphibole and Fe-Ti oxide domain (right) and solid-state dynamic recrystallized brown amphibole (left – black arrowheads). (C) U1601C-147R-1, 95-97 cm (TS130 – 727 mbsf): Gabbro mylonite in contact with serpentinized dunite, cut by undeformed carbonate veins. Cataclasis and brecciation overprints low-temperature plagioclase mylonitic fabric (black arrowheads) alongside dynamic recrystallization of secondary colourless-to-pale-green-brown amphibole (white arrowheads). White box shows location of 8D. (D) U1601C-147R-1, 95-97 cm (TS130 – 727 mbsf): Close-up of 8C showing plane polar (PPL) and cross-polar (XPL) views of low-temperature mylonitic plagioclase fabric overprinted by cataclasis and brecciation alongside dynamic recrystallization of secondary colourless-to-pale-green-brown amphibole. (E) U1601C-133R-1, 19-22 cm (TS85 – 689 mbsf): Plane polar (PPL) and cross-polar (XPL) views of a gabbro mylonite showing ultramylonitic granular flow band of plagioclase and amphibole (top-right) (see **Fig 8F**. for SEM image). Secondary green-brown amphibole alteration overprint on coarse-grained domain is undeformed. Mineral abbreviations are listed in Fig. 6. caption.

Fig. 9. Summary diagram showing distribution of ductile deformation with respect to lithology. High strain ductile deformation concentrates in Domain 2 and 3 where lithological heterogeneity is highest.

Fig. 10. Summary of findings: (A) Sketch section of an OCC with a generalized thermal structure based on **[22, 50]**, showing distributed zone of high-temperature ductile deformation in the lower lithosphere. (B) Schematic cartoon representation of the spatial relationships between lithological heterogeneity and high-temperature ductile deformation as reported from Hole U1601C. Deformation localizes in lithological heterogeneity zone, with high density of mafic intrusive contacts (HSZs shown by hatched zones). Note: the declination of contacts and ductile deformation fabrics is unconstrained. (C-F) Cartoon sequence of events shown at a micro-scale (not to scale) with key shown below: (C) Gabbroic intrusion ± emplacement-related magmatic deformation. (D) High-temperature solid-state ductile deformation ± melt-present deformation of plagioclase, pyroxene, and olivine localized at intrusive contact. (E) Focused late melt infiltration and Fe-Ti oxide precipitation localized at deforming intrusive contact. Melt infiltration enhances and sustains further deformation. (F) Fluid flow and alteration forms early amphibole alteration assemblage at intrusive contacts which accommodates further ductile deformation.

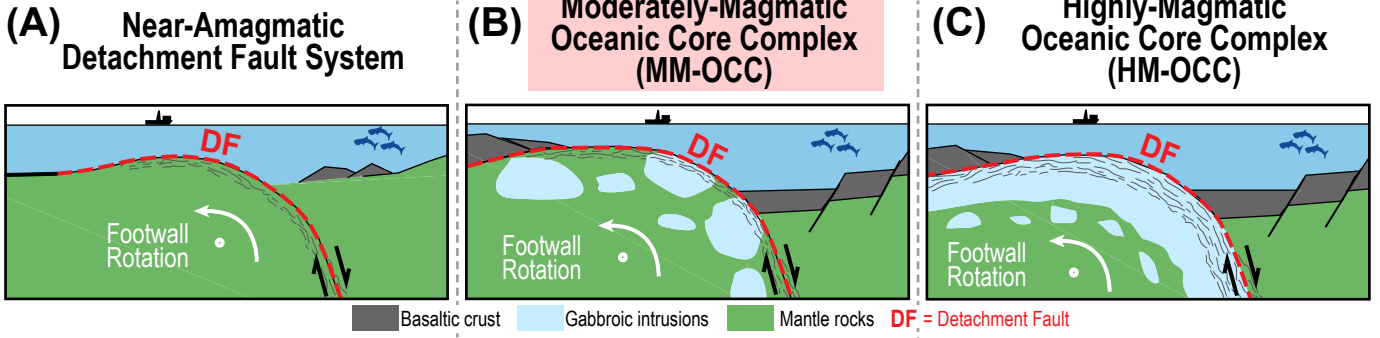

Prior Classifications

Smooth Detachment Fault	*Corrugated Detachment Fault*	*Corrugated Detachment Fault*
Near-Amagmatic Detachment	*Oceanic Core Complex (OCC)*	*Oceanic Core Complex (OCC)*
	Megamullion	*Megamullion*

Examples

Ultraslow MORs:	**Slow MORs:**	**Slow to Ultraslow MORs:**
Eastern SWIR	***Atlantis Massif (MAR)***	*Atlantis Bank (SWIR)*
Gakkel Ridge	*13°N & 15°N (MAR)*	*Godzilla (PSP)*
	EMARK & Kane (MAR)	

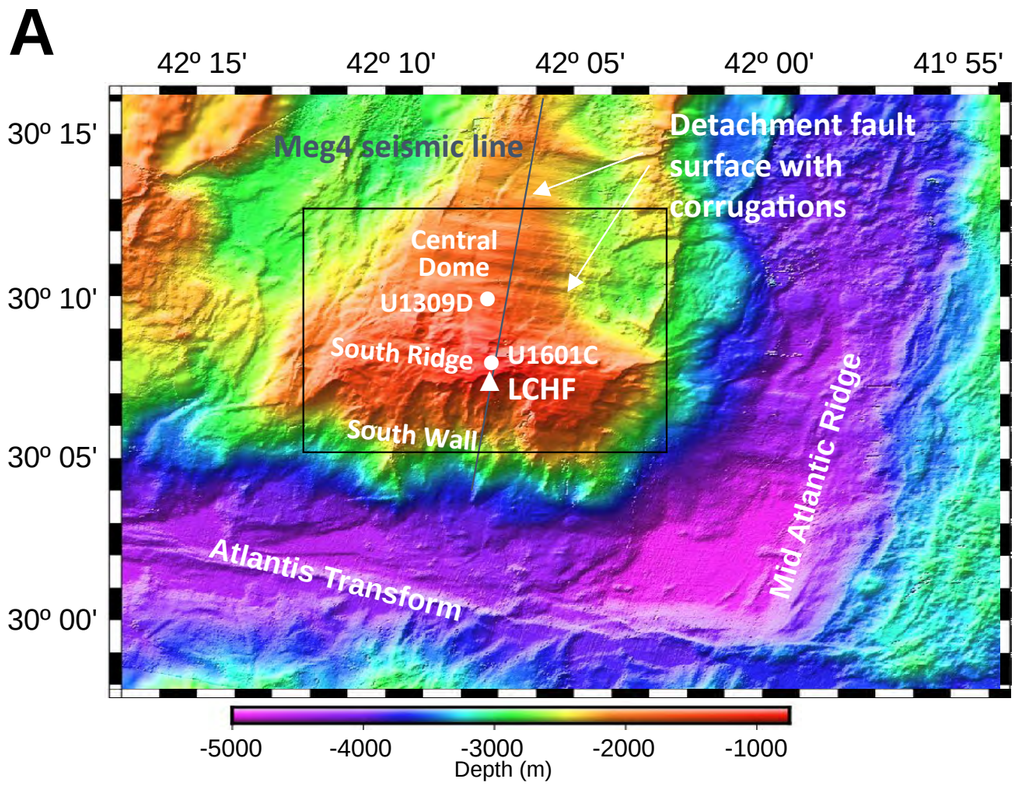
A
42º 15'
42º 10'
42º 05'
42º 00'
41º 55'
30º 15'
30º 10'
30º 05'
30º 00'
Meg4 seismic line
Detachment fault surface with corrugations
Central Dome
U1309D
South Ridge
U1601C
LCHF
South Wall
Atlantis Transform
Mid Atlantic Ridge
-5000
-4000
-3000
-2000
-1000
Depth (m)

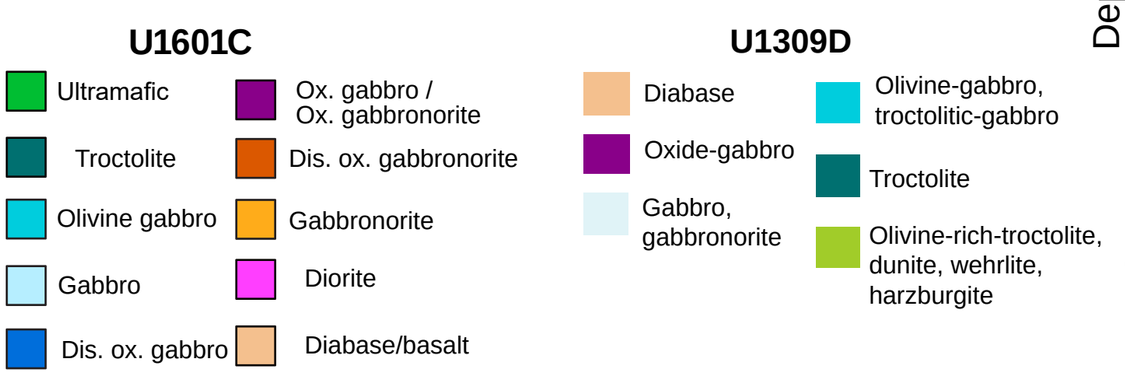
U1601C
Ultramafic
Troctolite
Olivine gabbro
Gabbro
Dis. ox. gabbro
Ox. gabbro / Ox. gabbronorite
Dis. ox. gabbronorite
Gabbronorite
Diorite
Diabase/basalt
U1309D
Diabase
Oxide-gabbro
Gabbro, gabbronorite
Olivine-gabbro, troctolitic-gabbro
Troctolite
Olivine-rich-troctolite, dunite, wehrlite, harzburgite

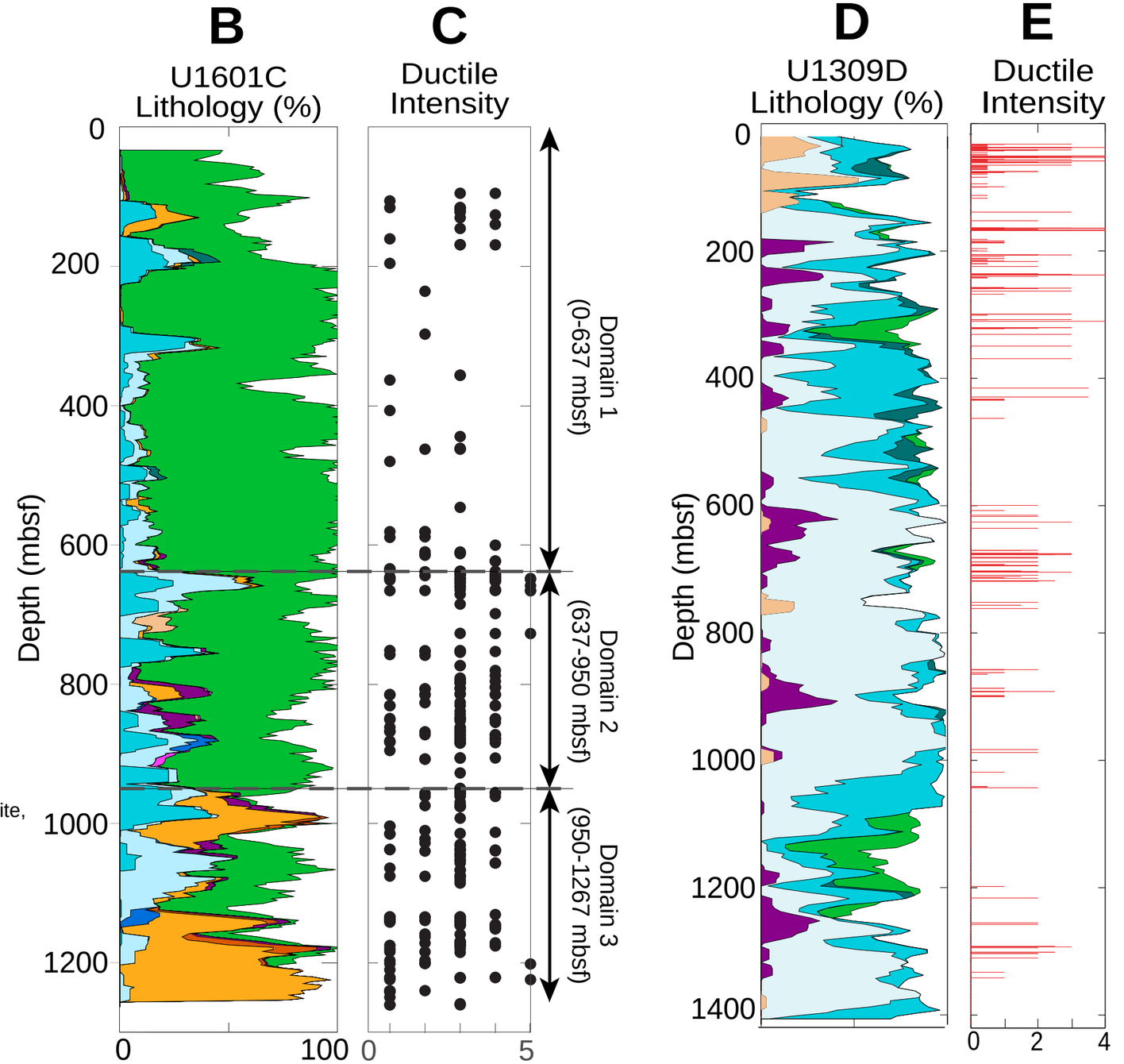
B
U1601C Lithology (%)
C
Ductile Intensity
D
U1309D Lithology (%)
E
Ductile Intensity
Depth (mbsf)
0
200
400
600
800
1000
1200
1400
0
100
0
5
0
2
4
Domain 1 (0-637 mbsf)
Domain 2 (637-950 mbsf)
Domain 3 (950-1267 mbsf)

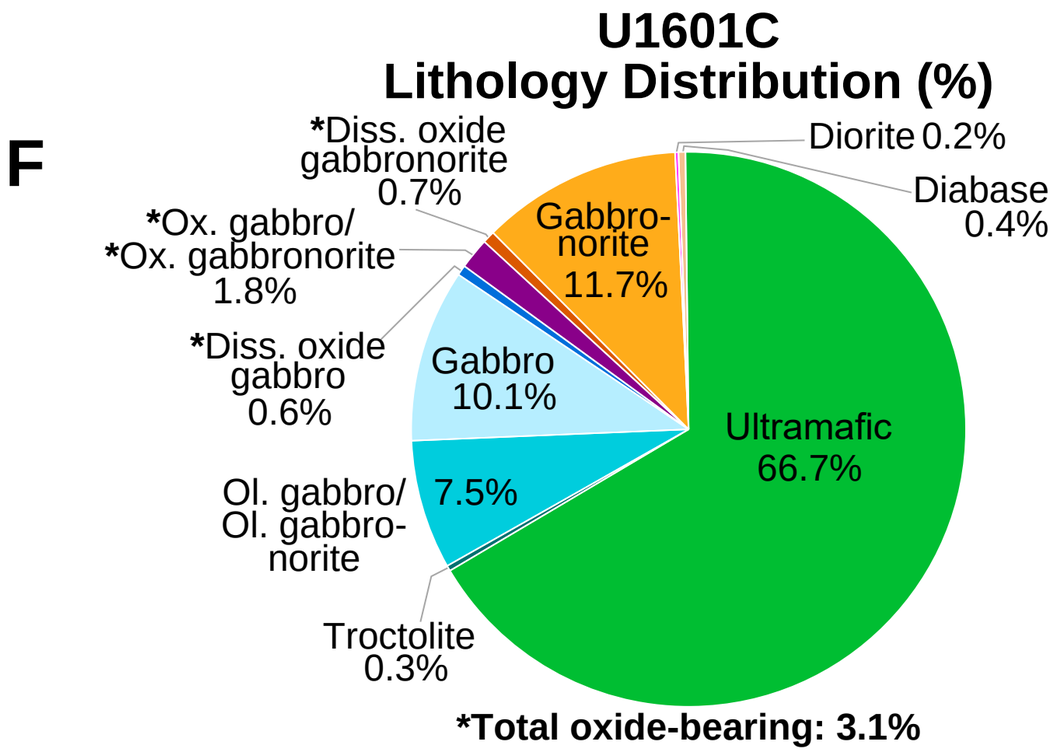
F
U1601C
Lithology Distribution (%)
*Diss. oxide gabbronorite 0.7%
Diorite 0.2%
Diabase 0.4%
*Ox. gabbro/ *Ox. gabbronorite 1.8%
Gabbro-norite 11.7%
*Diss. oxide gabbro 0.6%
Gabbro 10.1%
Ultramafic 66.7%
Ol. gabbro/ Ol. gabbro-norite 7.5%
Troctolite 0.3%
*Total oxide-bearing: 3.1%

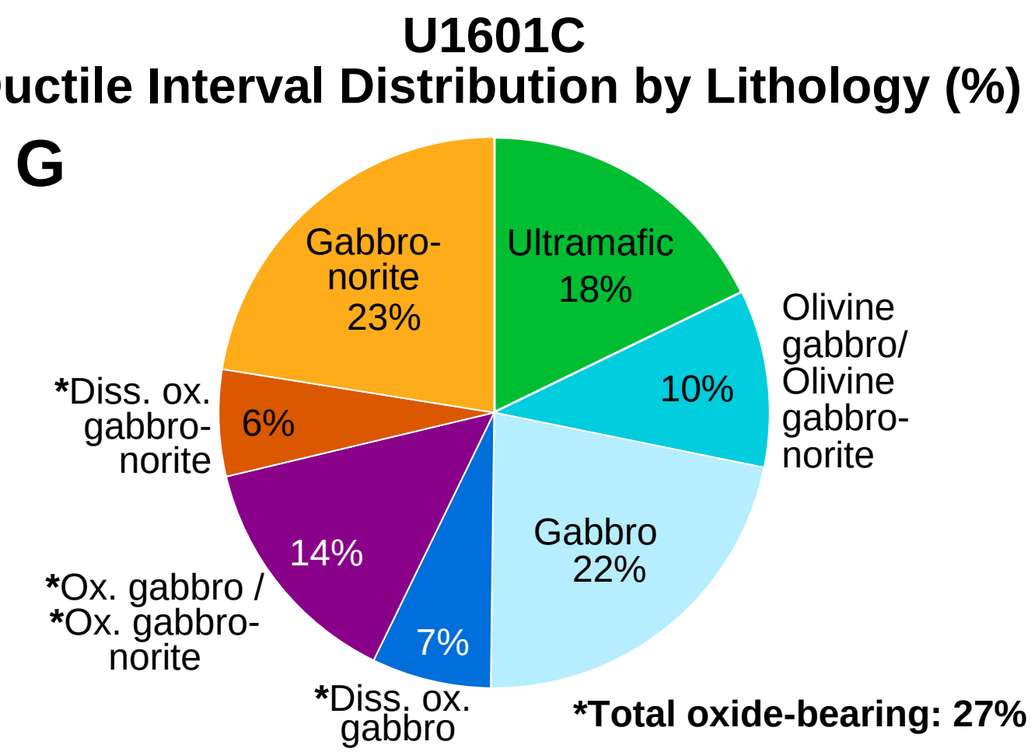
G
U1601C
Ductile Interval Distribution by Lithology (%)
Gabbro-norite 23%
Ultramafic 18%
Olivine gabbro/ Olivine gabbro-norite 10%
*Diss. ox. gabbro-norite 6%
Gabbro 22%
*Ox. gabbro / *Ox. gabbro-norite 14%
7%
*Diss. ox. gabbro
*Total oxide-bearing: 27%

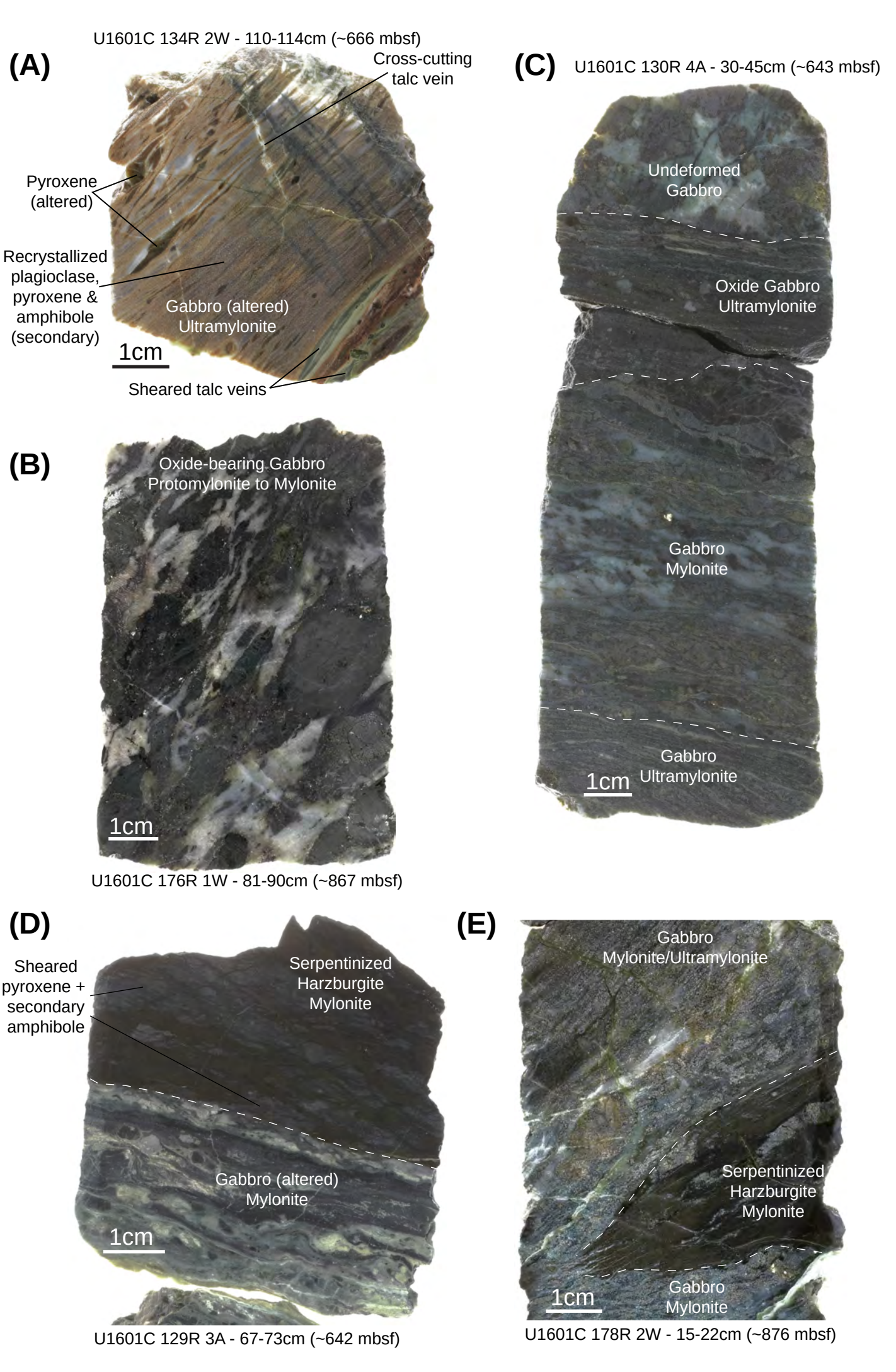
(A)
U1601C 134R 2W - 110-114cm (~666 mbsf)
Cross-cutting talc vein
Pyroxene (altered)
Recrystallized plagioclase, pyroxene & amphibole (secondary)
Gabbro (altered) Ultramylonite
1cm
Sheared talc veins
(B)
Oxide-bearing Gabbro Protomylonite to Mylonite
1cm
U1601C 176R 1W - 81-90cm (~867 mbsf)
(C)
U1601C 130R 4A - 30-45cm (~643 mbsf)
Undeformed Gabbro
Oxide Gabbro Ultramylonite
Gabbro Mylonite
Gabbro Ultramylonite
1cm
(D)
Sheared pyroxene + secondary amphibole
Serpentinized Harzburgite Mylonite
Gabbro (altered) Mylonite
1cm
U1601C 129R 3A - 67-73cm (~642 mbsf)
(E)
Gabbro Mylonite/Ultramylonite
Serpentinized Harzburgite Mylonite
Gabbro Mylonite
1cm
U1601C 178R 2W - 15-22cm (~876 mbsf)

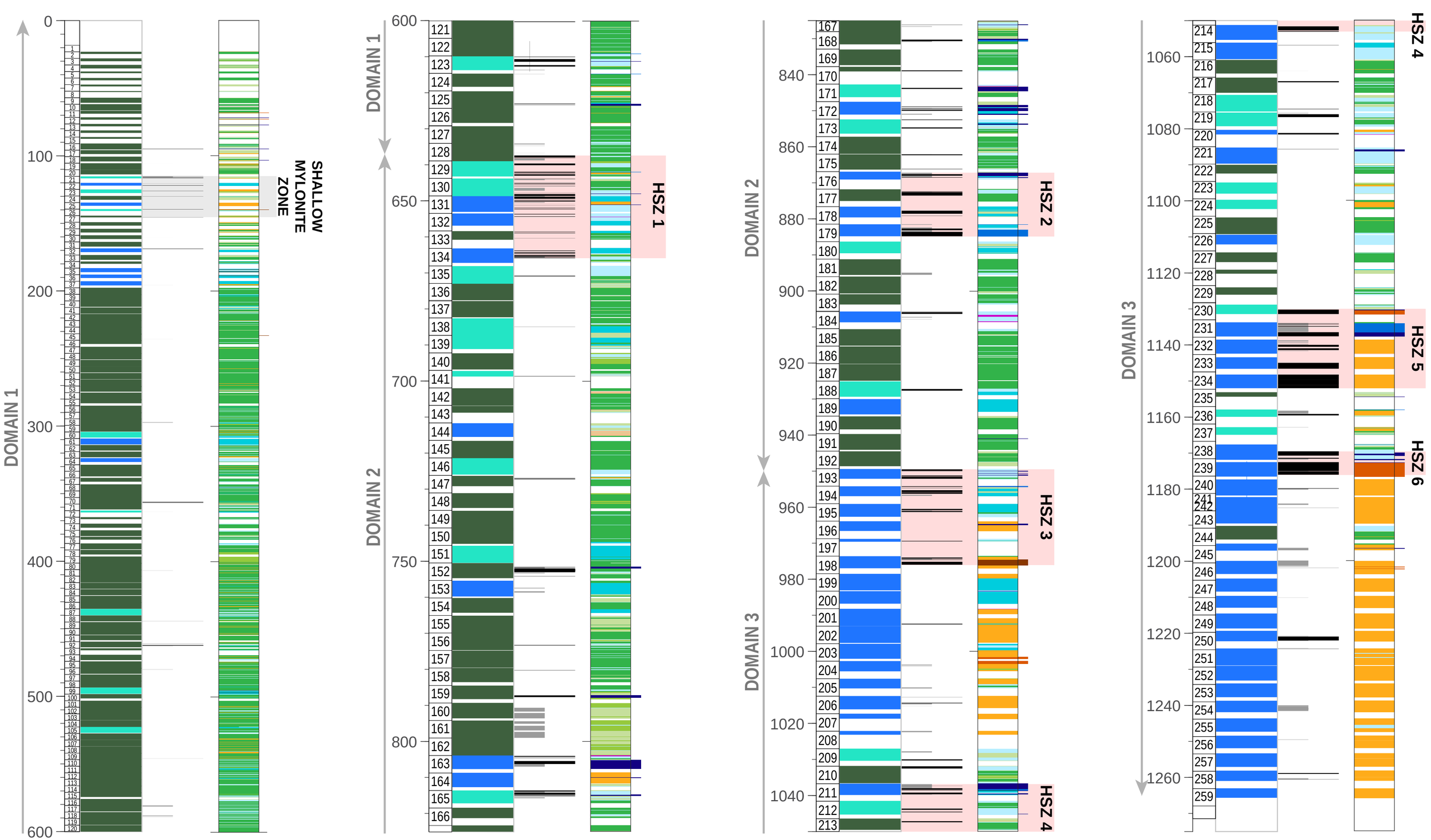
DOMAIN 1
DOMAIN 2
DOMAIN 3
SHALLOW MYLONITE ZONE
HSZ 1
HSZ 2
HSZ 3
HSZ 4
HSZ 5
HSZ 6
>66% Ultramafic
33%>66% Mafic, 33%>66% Ultramafic
>66% Mafic
Low strain ductile interval (weak / strong foliation)
High strain ductile interval (protomylonite / mylonite / ultramylonite)
HSZ (HIGH STRAIN ZONE) 1 TO 6
SHALLOW MYLONITE ZONE
diabase
diorite
gabbro
disseminated oxide gabbro
oxide gabbro
gabbronorite
disseminated oxide gabbronorite
oxide gabbronorite
olivine gabbro
troctolite
harzburgite
dunite
opx-bearing dunite
pyroxenite

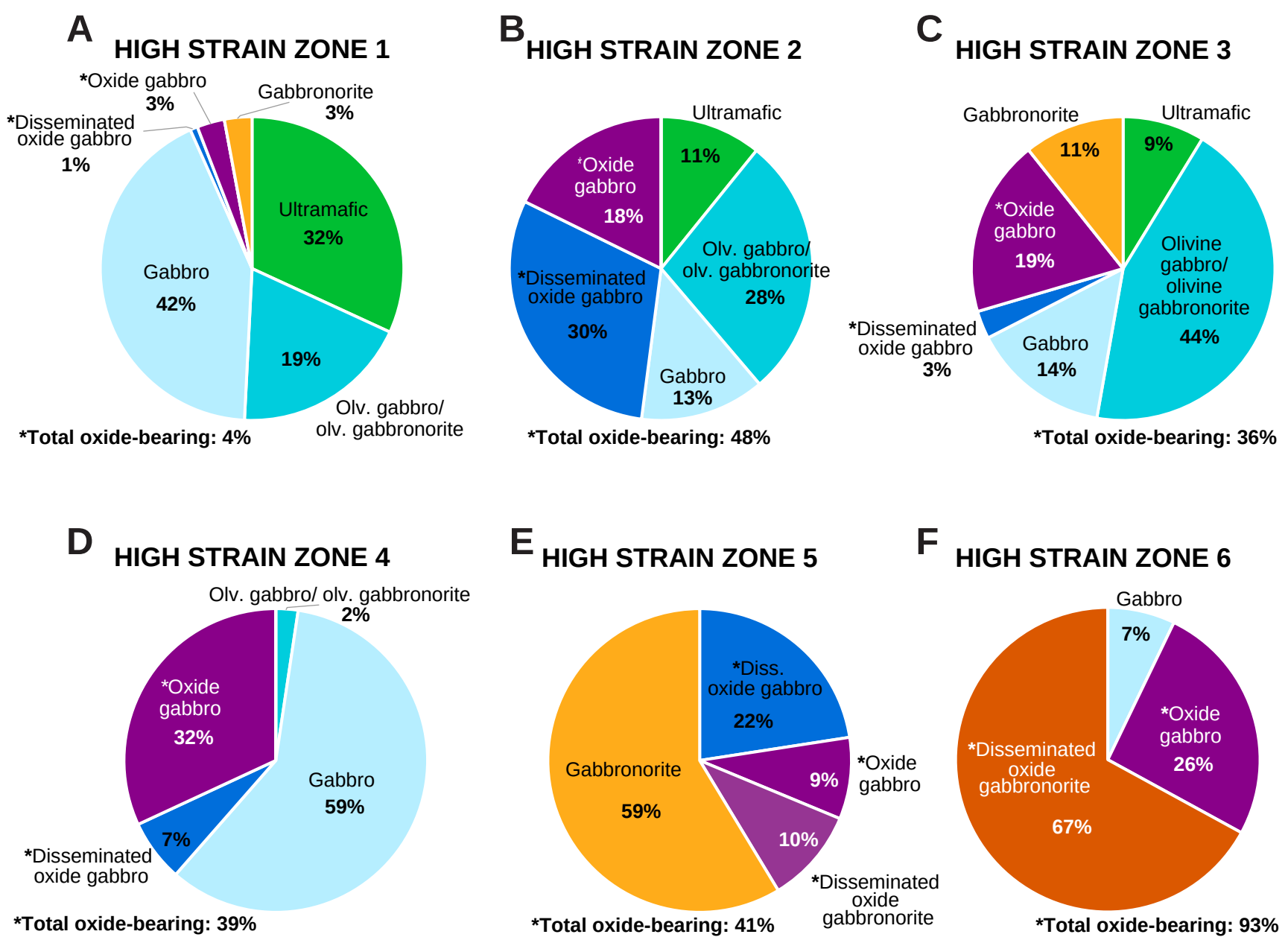
A
HIGH STRAIN ZONE 1
*Oxide gabbro 3%
Gabbronorite 3%
*Disseminated oxide gabbro 1%
Ultramafic 32%
Gabbro 42%
19%
Olv. gabbro/ olv. gabbronorite
*Total oxide-bearing: 4%
B
HIGH STRAIN ZONE 2
Ultramafic 11%
*Oxide gabbro 18%
Olv. gabbro/ olv. gabbronorite 28%
*Disseminated oxide gabbro 30%
Gabbro 13%
*Total oxide-bearing: 48%
C
HIGH STRAIN ZONE 3
Gabbronorite 11%
Ultramafic 9%
*Oxide gabbro 19%
Olivine gabbro/ olivine gabbronorite 44%
*Disseminated oxide gabbro 3%
Gabbro 14%
*Total oxide-bearing: 36%
D
HIGH STRAIN ZONE 4
Olv. gabbro/ olv. gabbronorite 2%
*Oxide gabbro 32%
Gabbro 59%
7%
*Disseminated oxide gabbro
*Total oxide-bearing: 39%
E
HIGH STRAIN ZONE 5
*Diss. oxide gabbro 22%
*Oxide gabbro 9%
Gabbronorite 59%
10%
*Disseminated oxide gabbronorite
*Total oxide-bearing: 41%
F
HIGH STRAIN ZONE 6
Gabbro 7%
*Oxide gabbro 26%
*Disseminated oxide gabbronorite 67%
*Total oxide-bearing: 93%

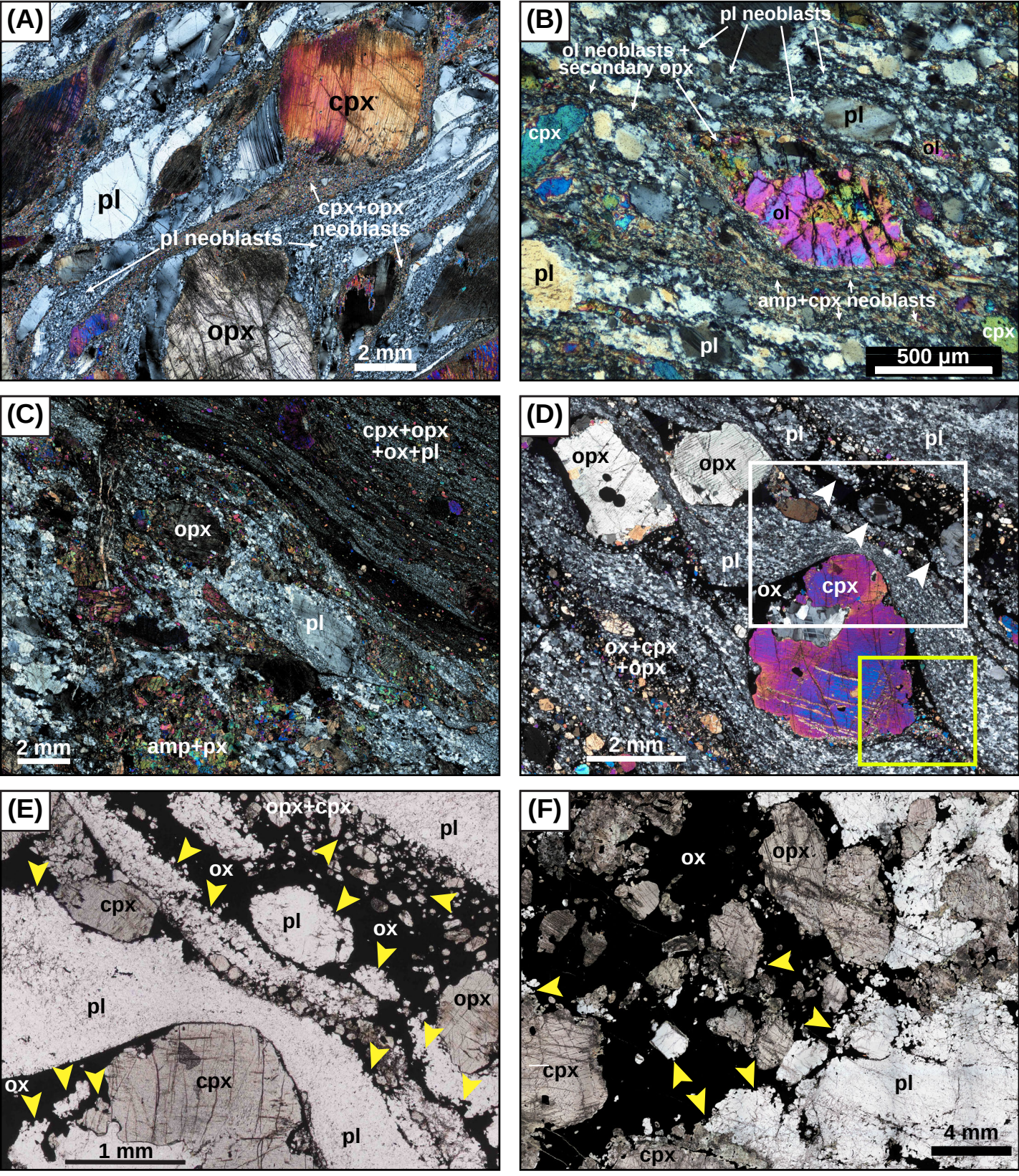
(A)
cpx
pl
cpx+opx
neoblasts
pl neoblasts
opx
2 mm
(B)
pl neoblasts
ol neoblasts +
secondary opx
pl
cpx
ol
ol
pl
amp+cpx neoblasts
cpx
pl
500 µm
(C)
cpx+opx
+ox+pl
opx
pl
2 mm
amp+px
(D)
pl
pl
opx
opx
pl
ox
cpx
ox+cpx
+opx
2 mm
(E)
opx+cpx
pl
ox
cpx
pl
ox
pl
opx
ox
cpx
pl
1 mm
(F)
ox
opx
cpx
pl
4 mm
cpx

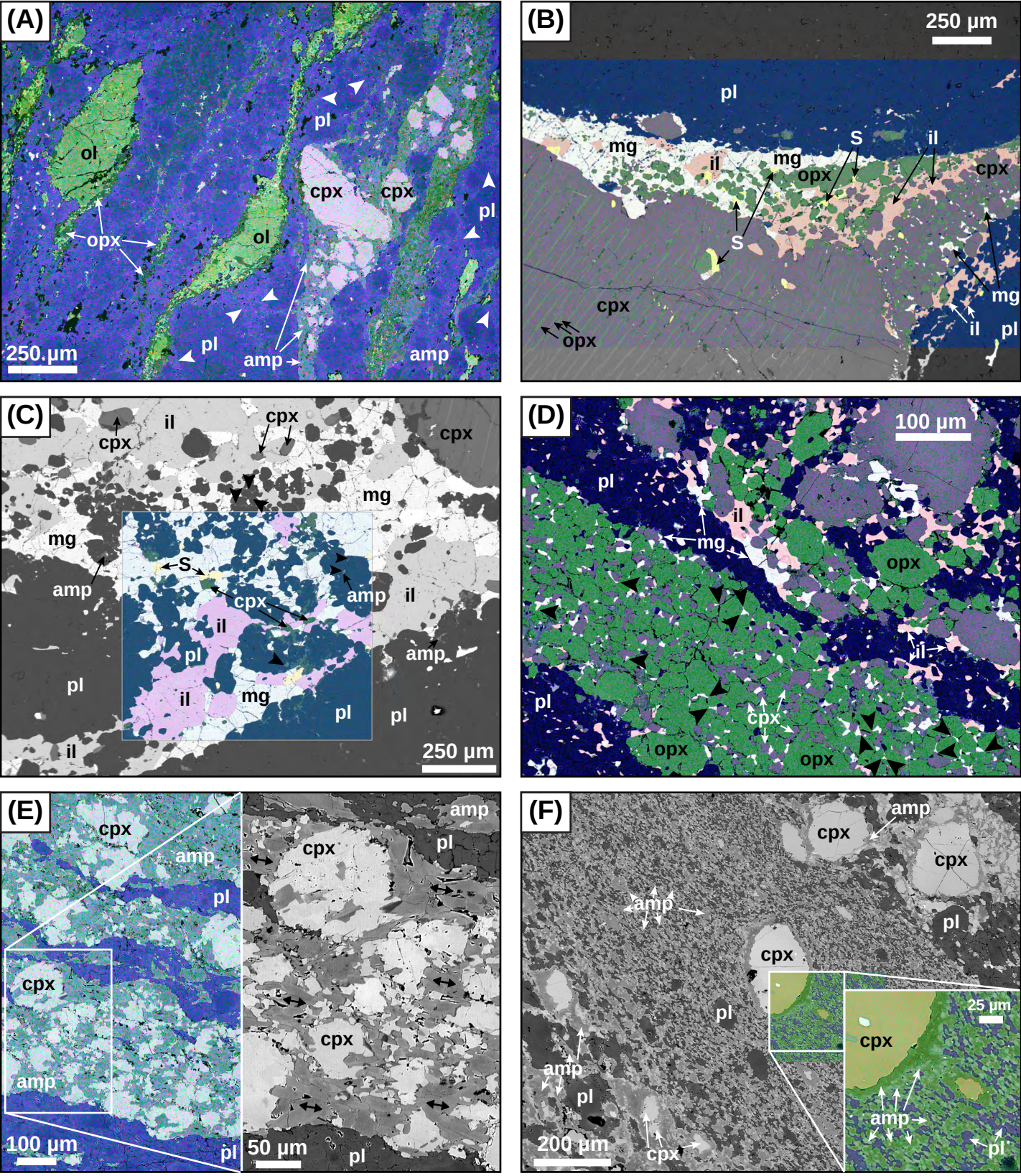
(A)
ol
pl
cpx
cpx
opx
ol
pl
pl
amp
amp
250 µm
(B)
250 µm
pl
mg
il
mg
S
il
opx
cpx
S
cpx
opx
mg
il
pl
(C)
il
cpx
cpx
cpx
mg
mg
S
amp
cpx
amp
il
il
pl
amp
pl
il
mg
pl
pl
il
250 µm
(D)
100 µm
pl
il
mg
opx
il
pl
cpx
opx
opx
(E)
cpx
amp
pl
cpx
amp
100 µm
pl
amp
pl
cpx
cpx
50 µm
pl
(F)
amp
cpx
cpx
amp
pl
cpx
pl
amp
pl
200 µm
cpx
25 µm
cpx
amp
amp
pl

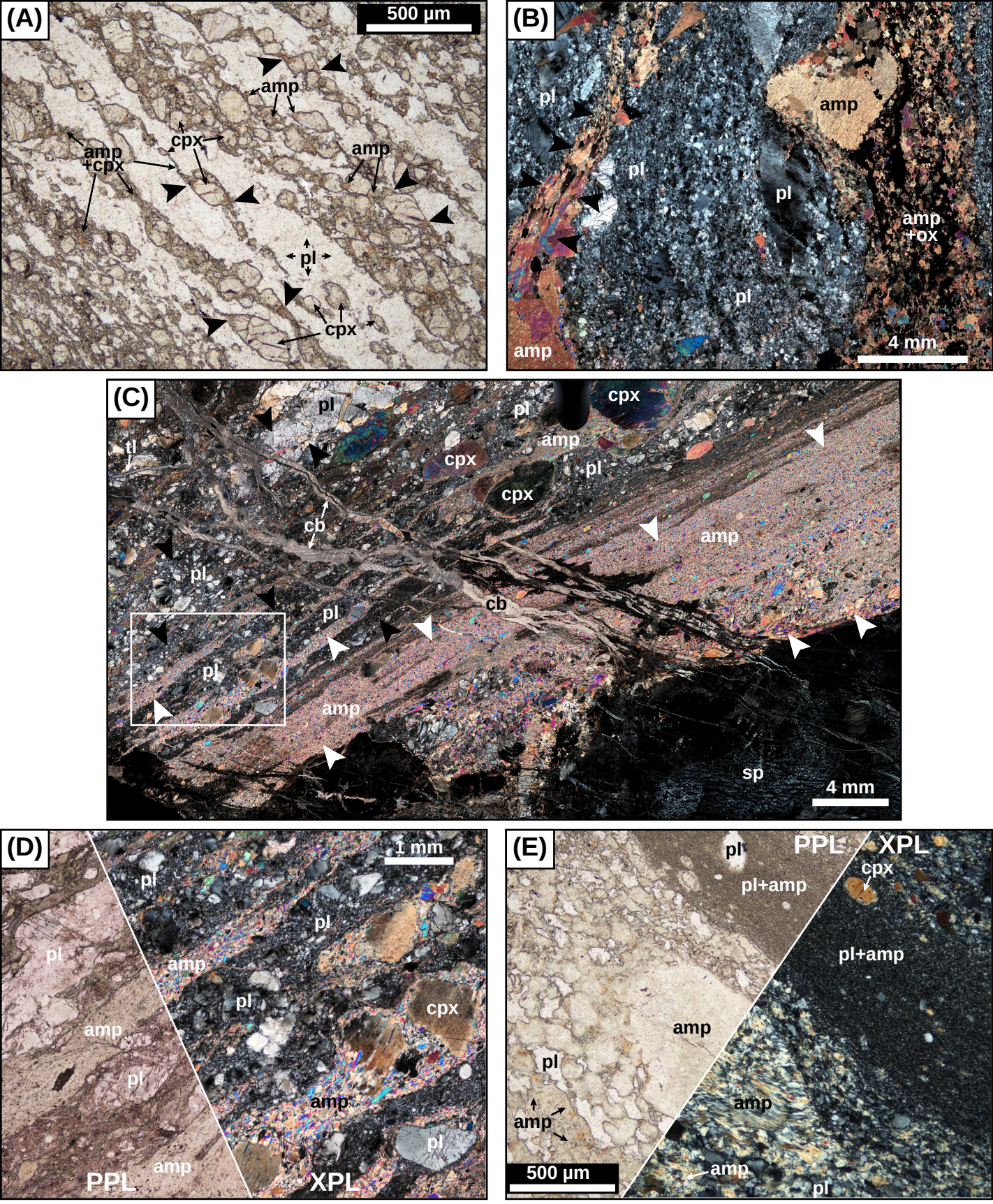
(A)
500 µm
amp
amp
+cpx
cpx
amp
pl
cpx
(B)
pl
amp
pl
pl
amp
+ox
pl
amp
4 mm
(C)
pl
pl
cpx
tl
amp
cpx
pl
cpx
cb
amp
pl
cb
pl
pl
amp
sp
4 mm
(D)
1 mm
pl
pl
pl
amp
pl
amp
cpx
pl
amp
amp
pl
PPL
XPL
(E)
PPL
XPL
pl
pl+amp
cpx
pl+amp
amp
pl
amp
amp
500 µm
amp
pl

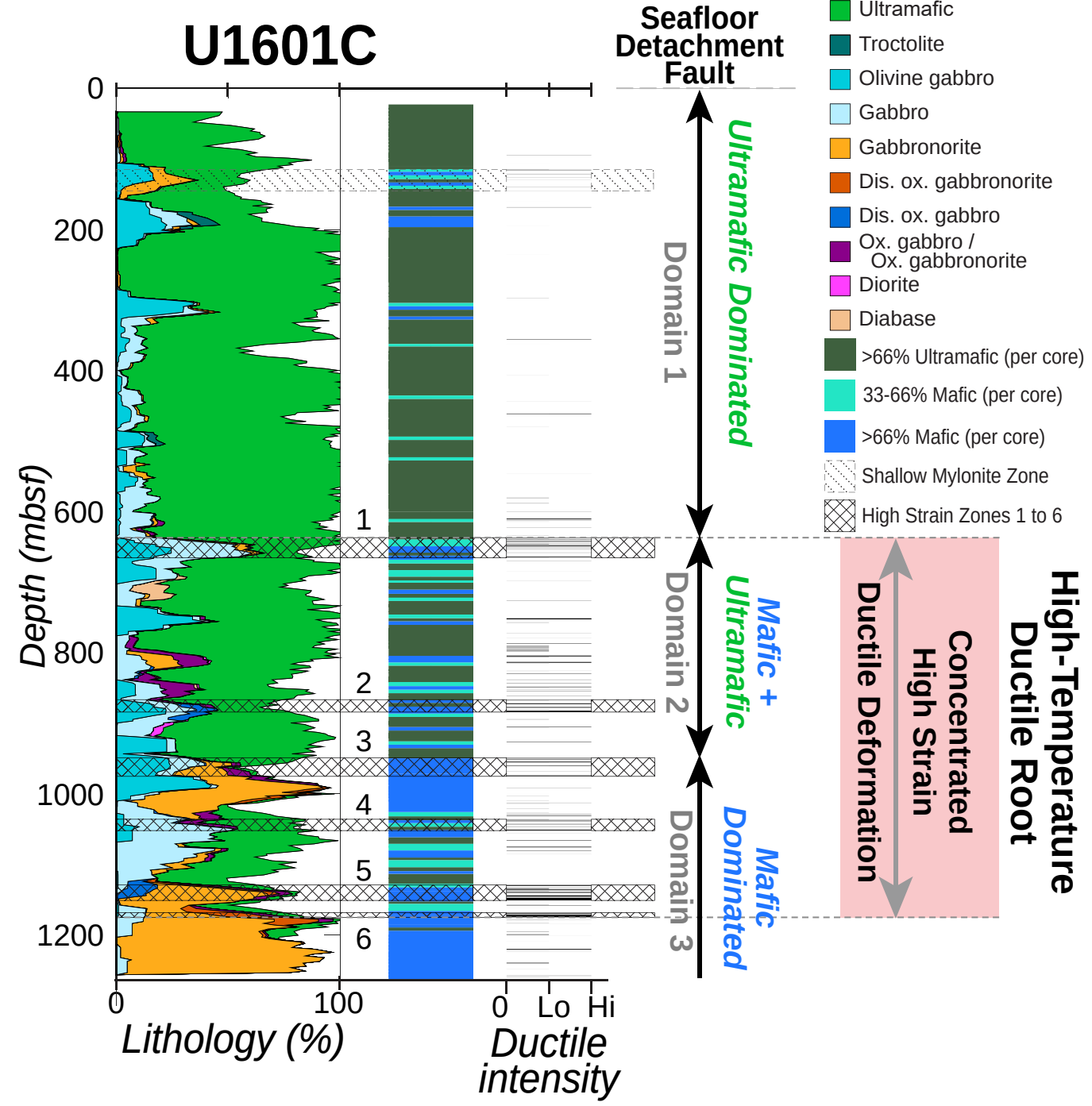
U1601C
Seafloor Detachment Fault
Ultramafic
Troctolite
Olivine gabbro
Gabbro
Gabbronorite
Dis. ox. gabbronorite
Dis. ox. gabbro
Ox. gabbro / Ox. gabbronorite
Diorite
Diabase
>66% Ultramafic (per core)
33-66% Mafic (per core)
>66% Mafic (per core)
Shallow Mylonite Zone
High Strain Zones 1 to 6
Ultramafic Dominated
Domain 1
Mafic + Ultramafic
Domain 2
Mafic Dominated
Domain 3
High-Temperature Ductile Root
Concentrated High Strain Ductile Deformation
Depth (mbsf)
0
200
400
600
800
1000
1200
1
2
3
4
5
6
0
100
Lithology (%)
0
Lo
Hi
Ductile intensity

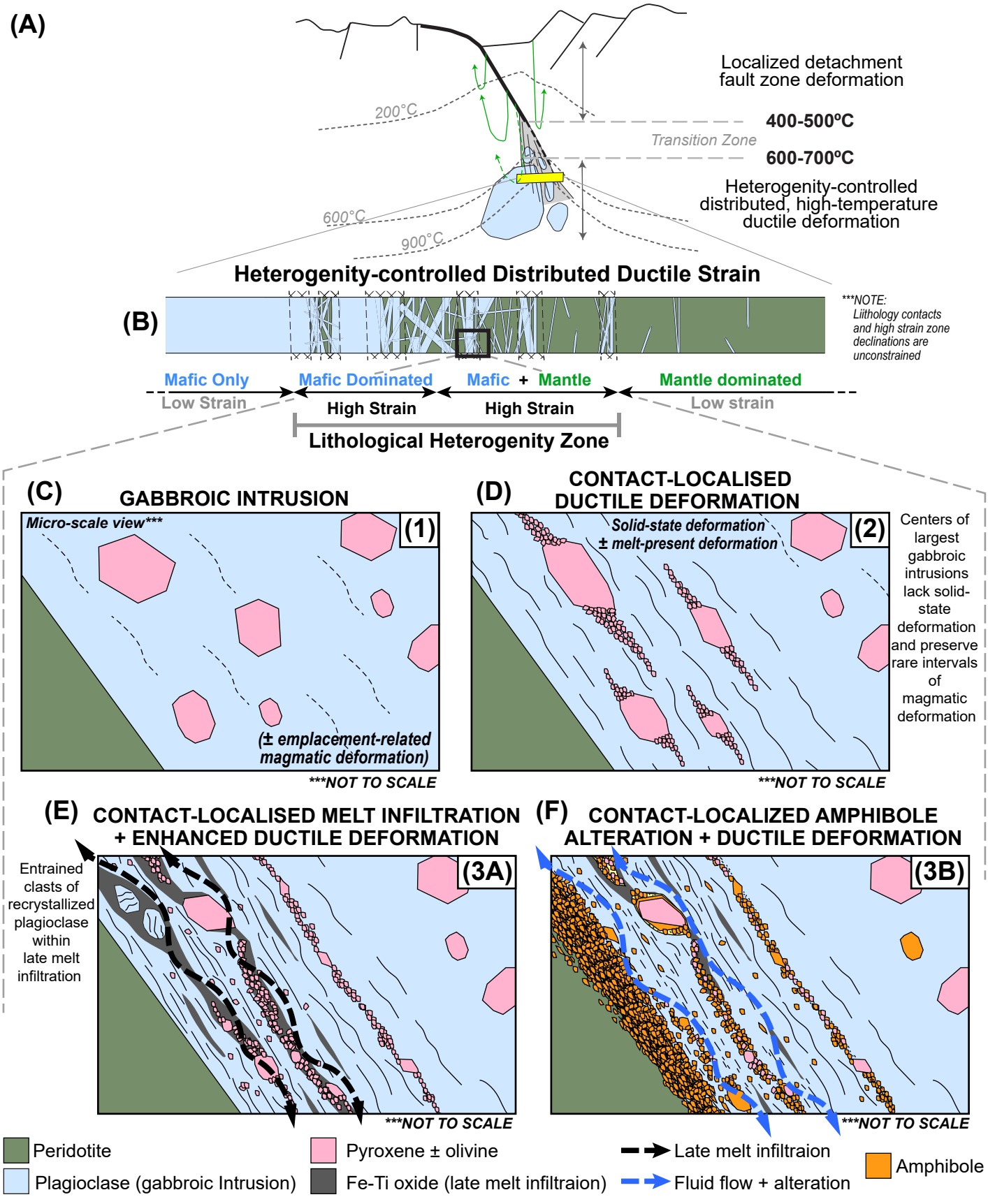
(A)
Localized detachment fault zone deformation
200°C
400-500ºC
Transition Zone
600-700ºC
Heterogenity-controlled distributed, high-temperature ductile deformation
600°C
900°C
Heterogenity-controlled Distributed Ductile Strain
(B)
***NOTE: Liithology contacts and high strain zone declinations are unconstrained
Mafic Only
Mafic Dominated
Mafic + Mantle
Mantle dominated
Low Strain
High Strain
High Strain
Low strain
Lithological Heterogenity Zone
(C)
GABBROIC INTRUSION
Micro-scale view***
(1)
(± emplacement-related magmatic deformation)
***NOT TO SCALE
(D)
CONTACT-LOCALISED DUCTILE DEFORMATION
Solid-state deformation ± melt-present deformation
(2)
***NOT TO SCALE
Centers of largest gabbroic intrusions lack solid-state deformation and preserve rare intervals of magmatic deformation
(E)
CONTACT-LOCALISED MELT INFILTRATION + ENHANCED DUCTILE DEFORMATION
Entrained clasts of recrystallized plagioclase within late melt infiltration
(3A)
***NOT TO SCALE
(F)
CONTACT-LOCALIZED AMPHIBOLE ALTERATION + DUCTILE DEFORMATION
(3B)
***NOT TO SCALE
Peridotite
Plagioclase (gabbroic Intrusion)
Pyroxene ± olivine
Fe-Ti oxide (late melt infiltraion)
Late melt infiltraion
Fluid flow + alteration
Amphibole

Science Advances
AAAS

Supplementary Materials for

Intrusive contacts localize high-temperature deformation and late melt infiltration in moderately-magmatic oceanic core complexes

Andrew J. Parsons *et al.*

*Corresponding author. Email: andy.parsons@plymouth.ac.uk

This PDF file includes:

Figs. S1 to S7
Tables S1 to S4

Other Supplementary Materials for this manuscript include the following:

Data S1

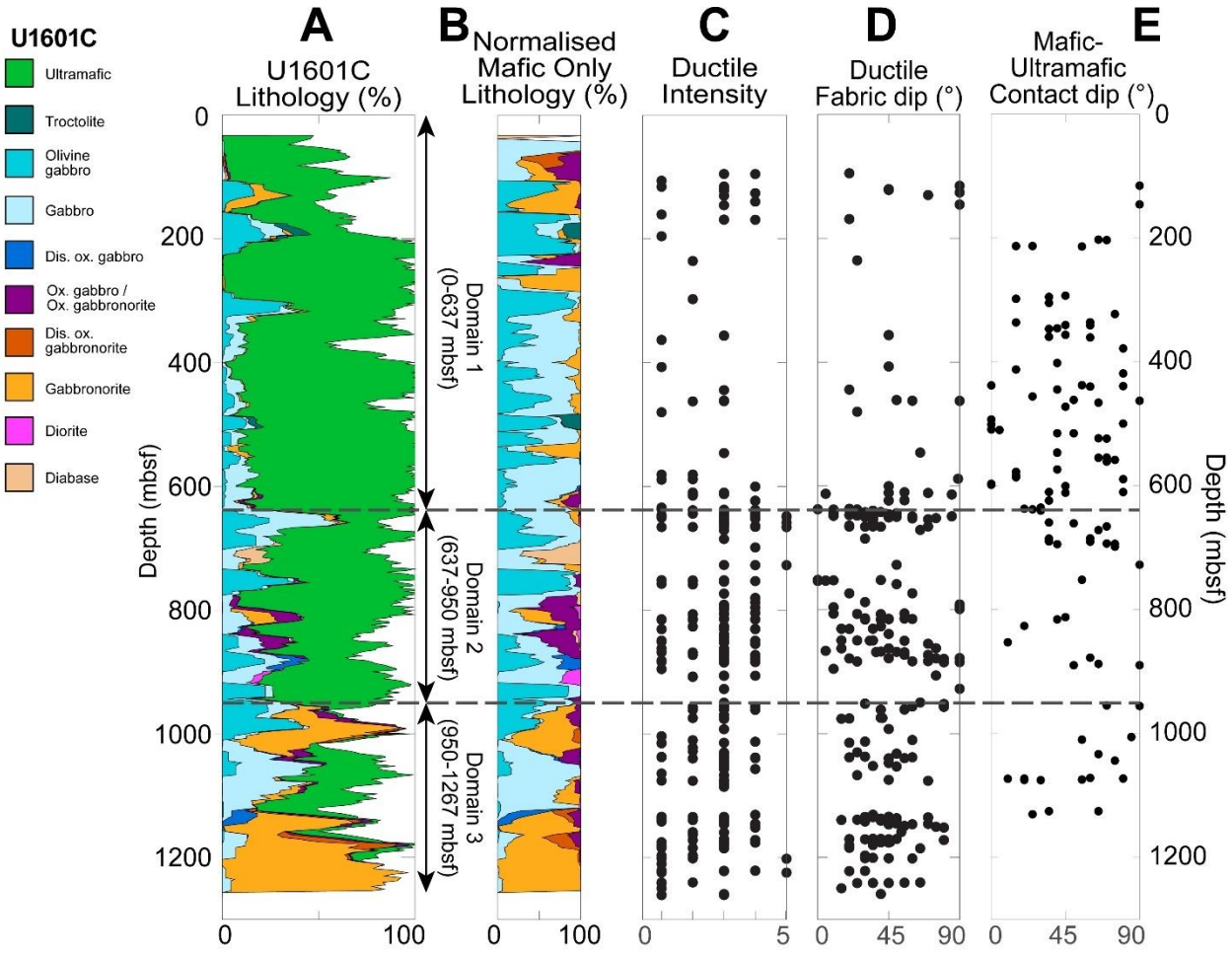

Fig. S1.

Summary of downhole lithology and ductile deformation fabrics in Hole U1601C. (A) Percentage distribution of lithologies as a rolling average. White portions show percentage of no recovery. (B) Normalized percentage distribution of mafic lithologies normalized as a rolling average, not including intervals of no recovery. (C) Downhole distribution of ductile deformation intervals, plotted as a function of Ductile Fabric Intensity; 1 = weak foliation; 2 = strong foliation; 3 = protomylonite; 4 = mylonite; 5= ultramylonite. (D) Ductile fabric dip (0° to 90°). (E) Mafic-ultramafic contact dip (0° to 90°). Data presented in (C), (D), and (E) is listed in **Data S1**.

Fig. S2A-K.

Close-up core images, thin-section scans, and photomicrographs of representative high-strain ductile deformation intervals, including protomylonite, mylonite, and ultramylonite.

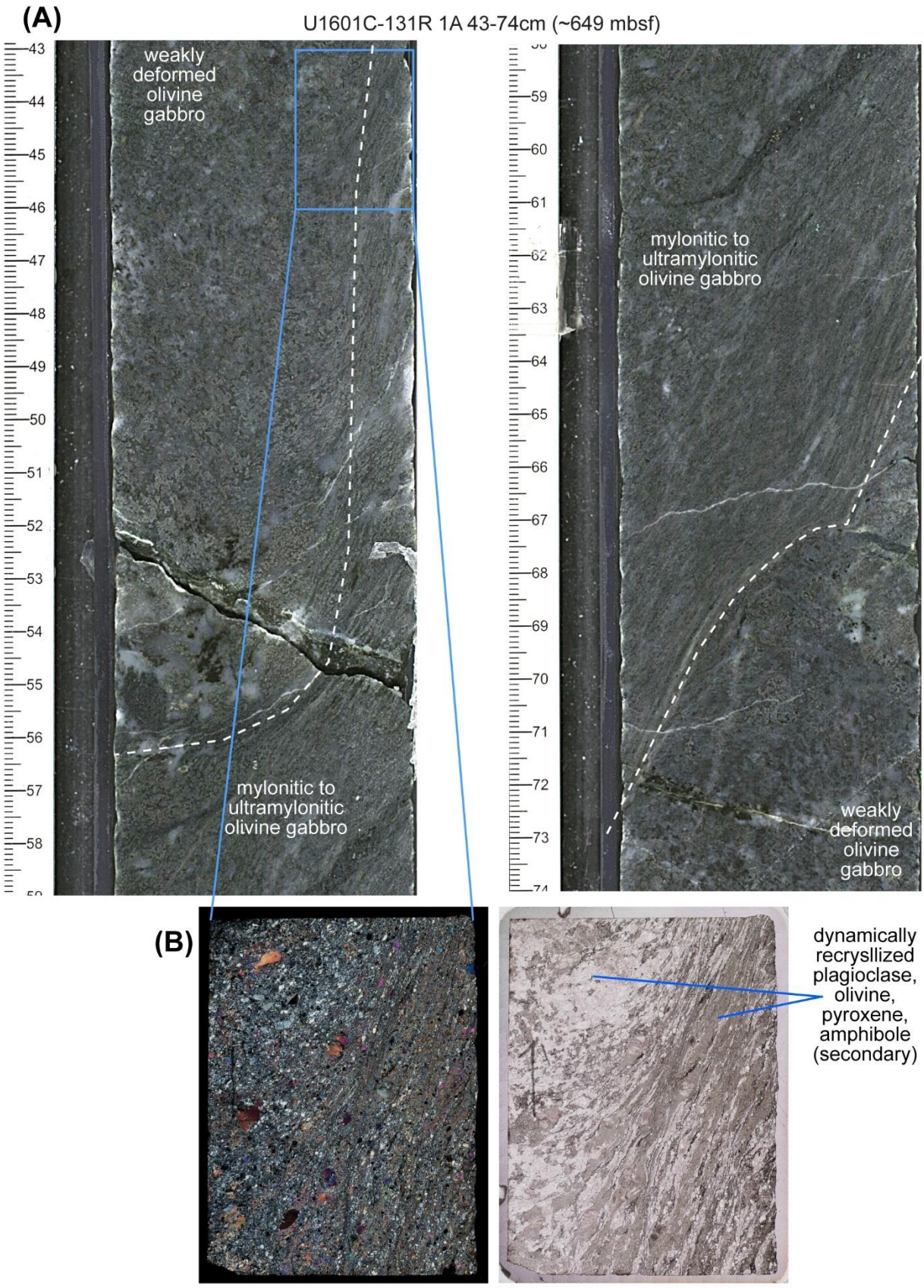
(A)
U1601C-131R 1A 43-74cm (~649 mbsf)
weakly deformed olivine gabbro
mylonitic to ultramylonitic olivine gabbro
mylonitic to ultramylonitic olivine gabbro
weakly deformed olivine gabbro
(B)
dynamically recrysllized plagioclase, olivine, pyroxene, amphibole (secondary)

Fig. S2

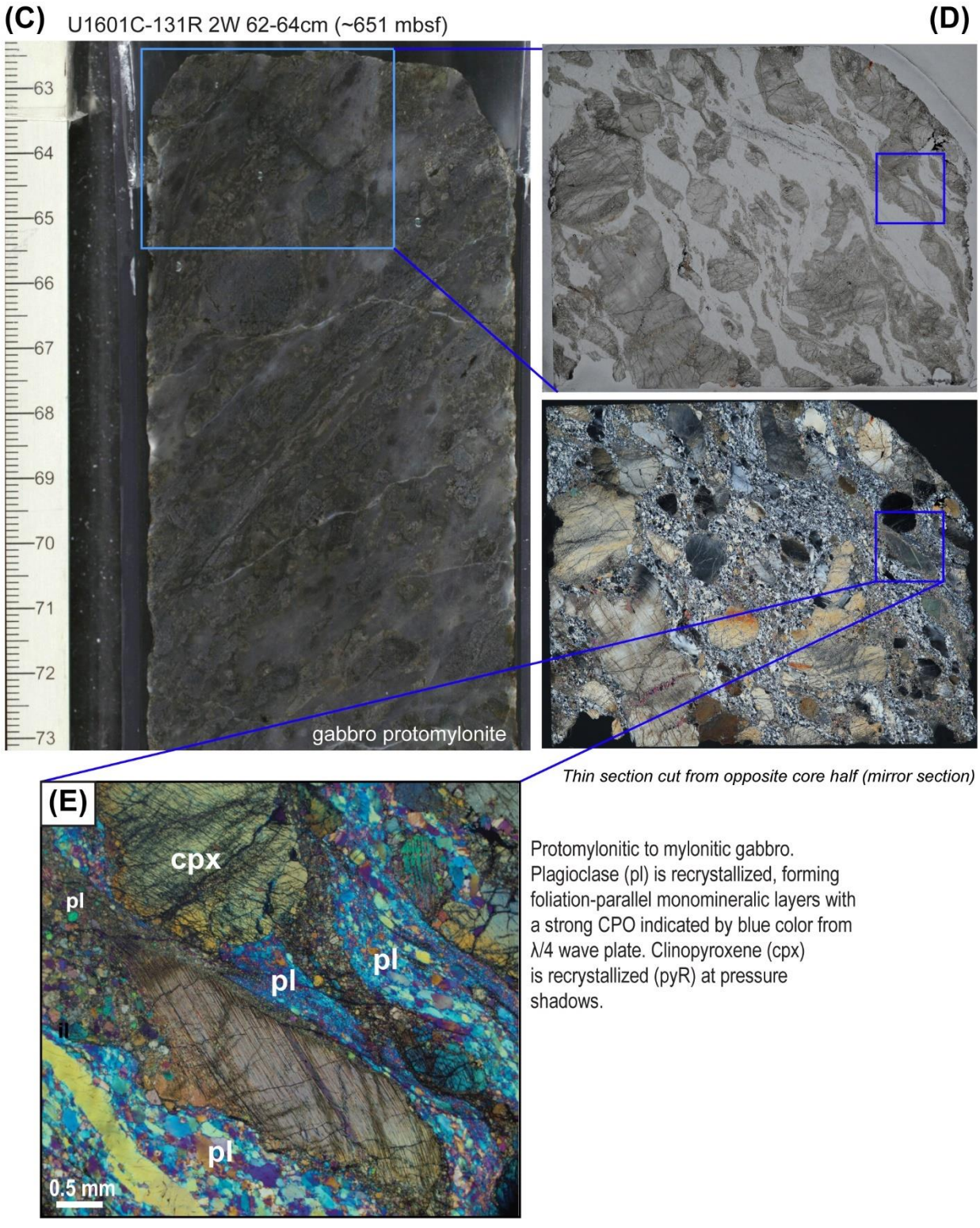

Fig. S2 continued.

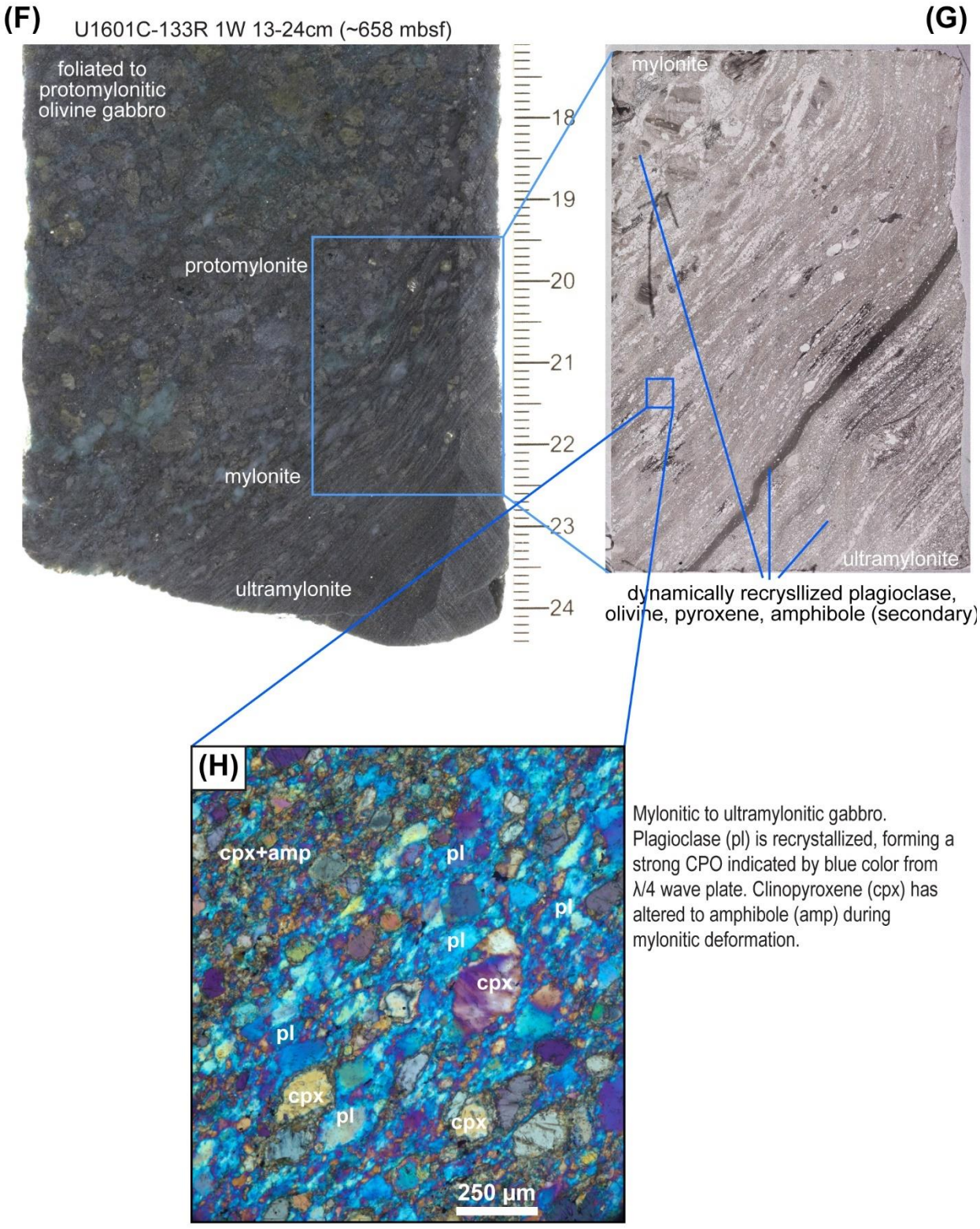

Fig. S2 continued.

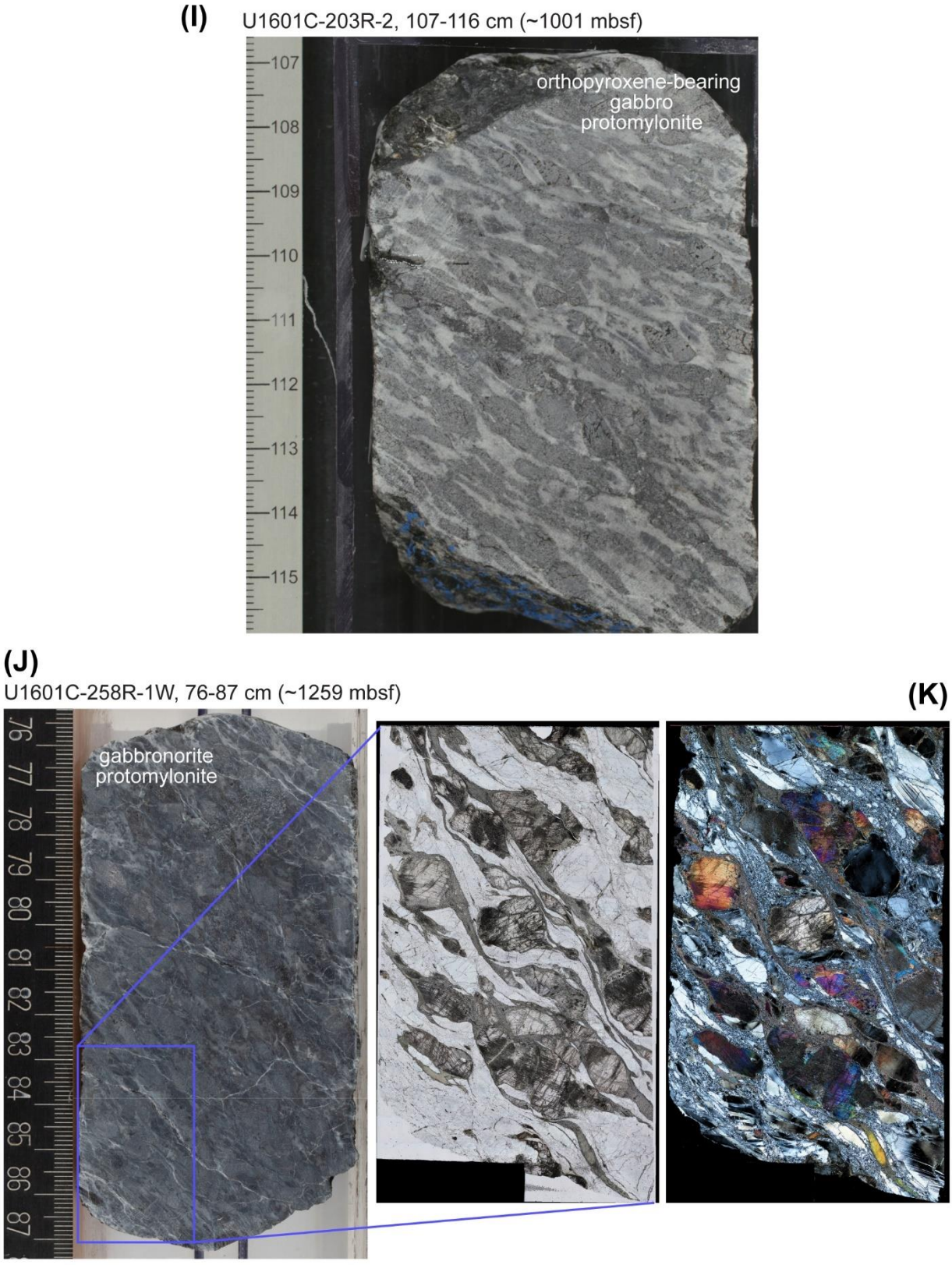

Fig. S2 continued.

Fig. S3A-O.

Close-up core images, thin-section scans, and photomicrographs of representative high-strain ductile deformation intervals in oxide-bearing gabbroic lithologies.

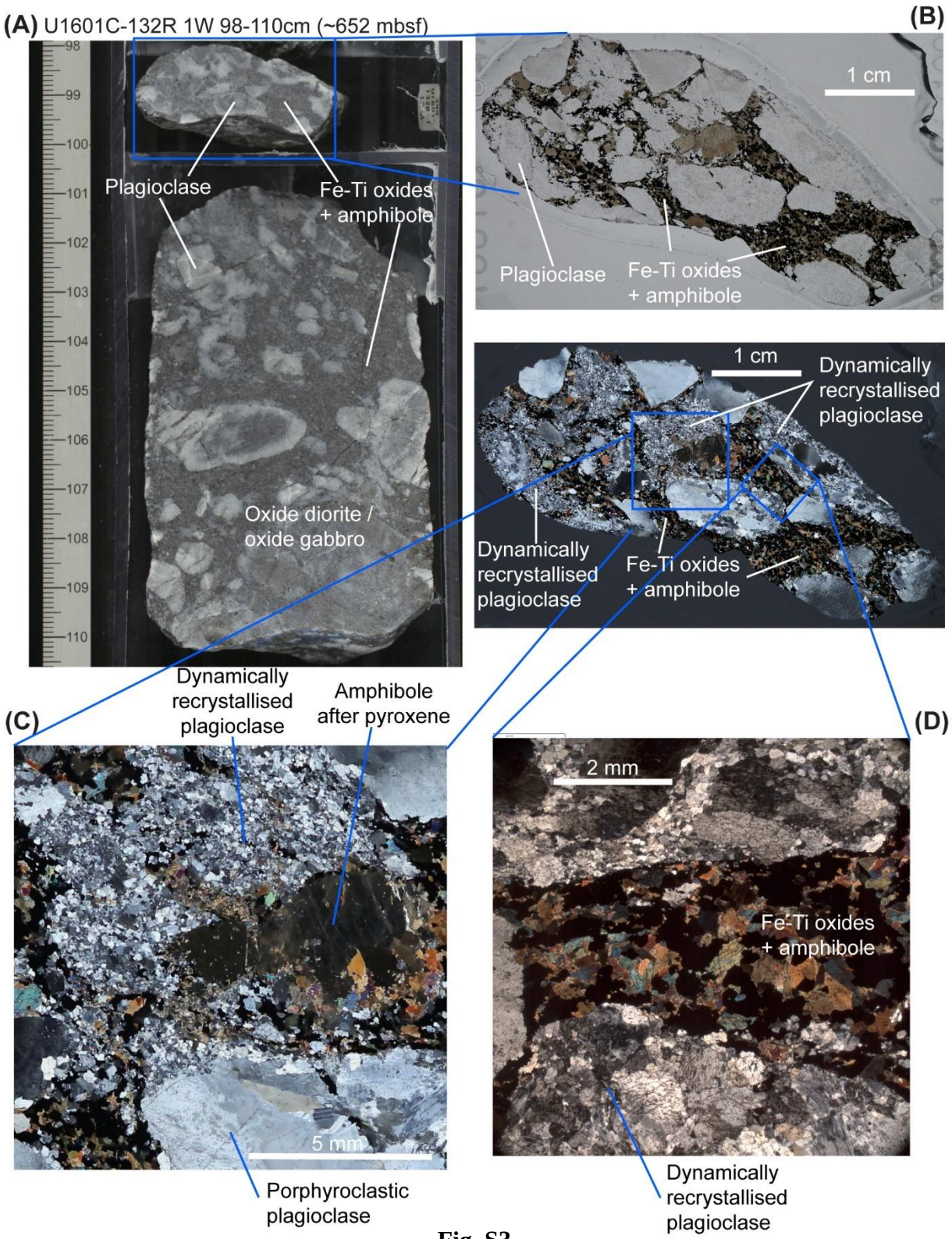
(A) U1601C-132R 1W 98-110cm (~652 mbsf)
Plagioclase
Fe-Ti oxides
+ amphibole
Oxide diorite /
oxide gabbro
(B)
1 cm
Plagioclase
Fe-Ti oxides
+ amphibole
1 cm
Dynamically
recrystallised
plagioclase
Dynamically
recrystallised
plagioclase
Fe-Ti oxides
+ amphibole
(C)
Dynamically
recrystallised
plagioclase
Amphibole
after pyroxene
5 mm
Porphyroclastic
plagioclase
(D)
2 mm
Fe-Ti oxides
+ amphibole
Dynamically
recrystallised
plagioclase

Fig. S3

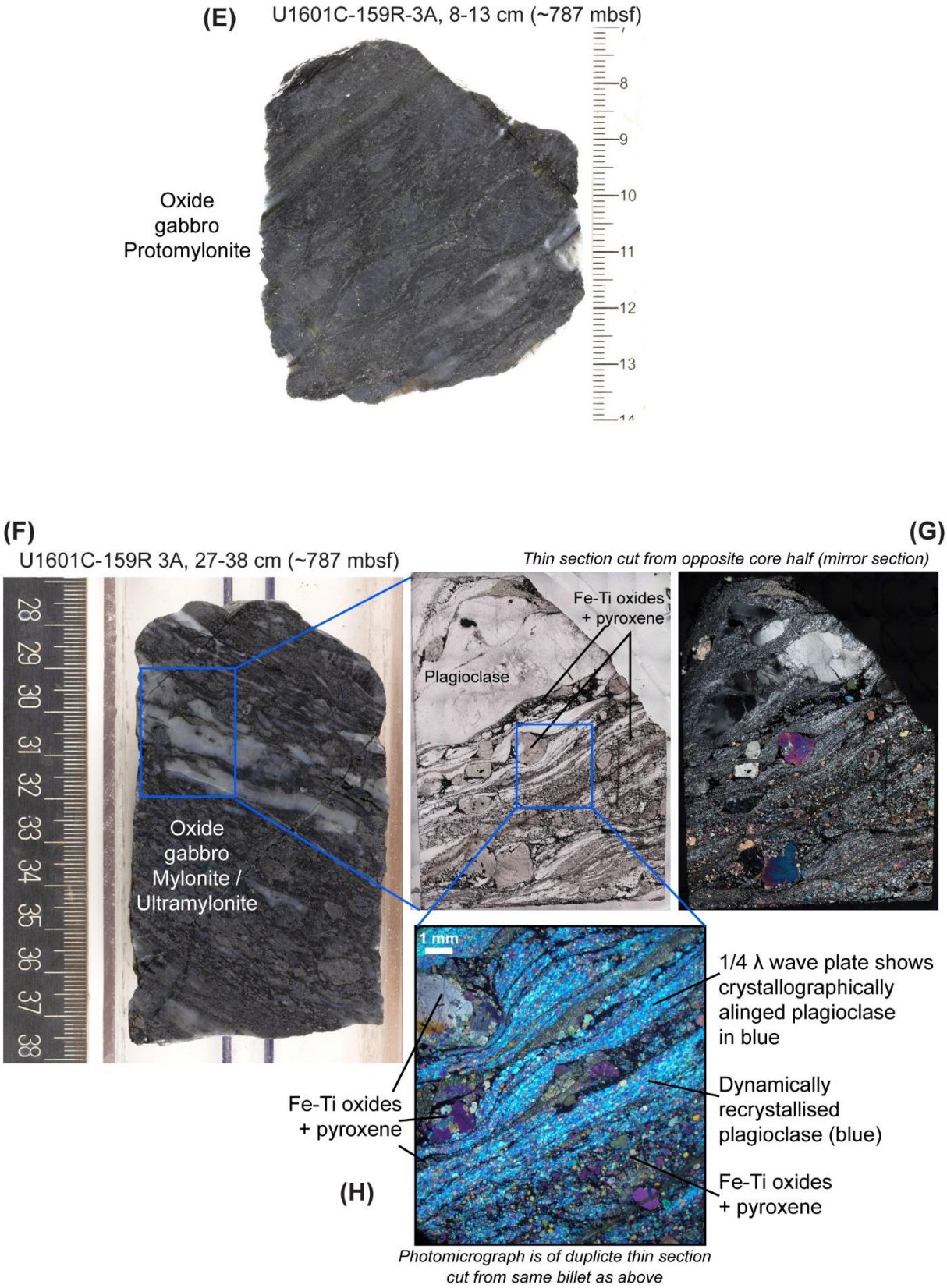

Fig. S3 continued.

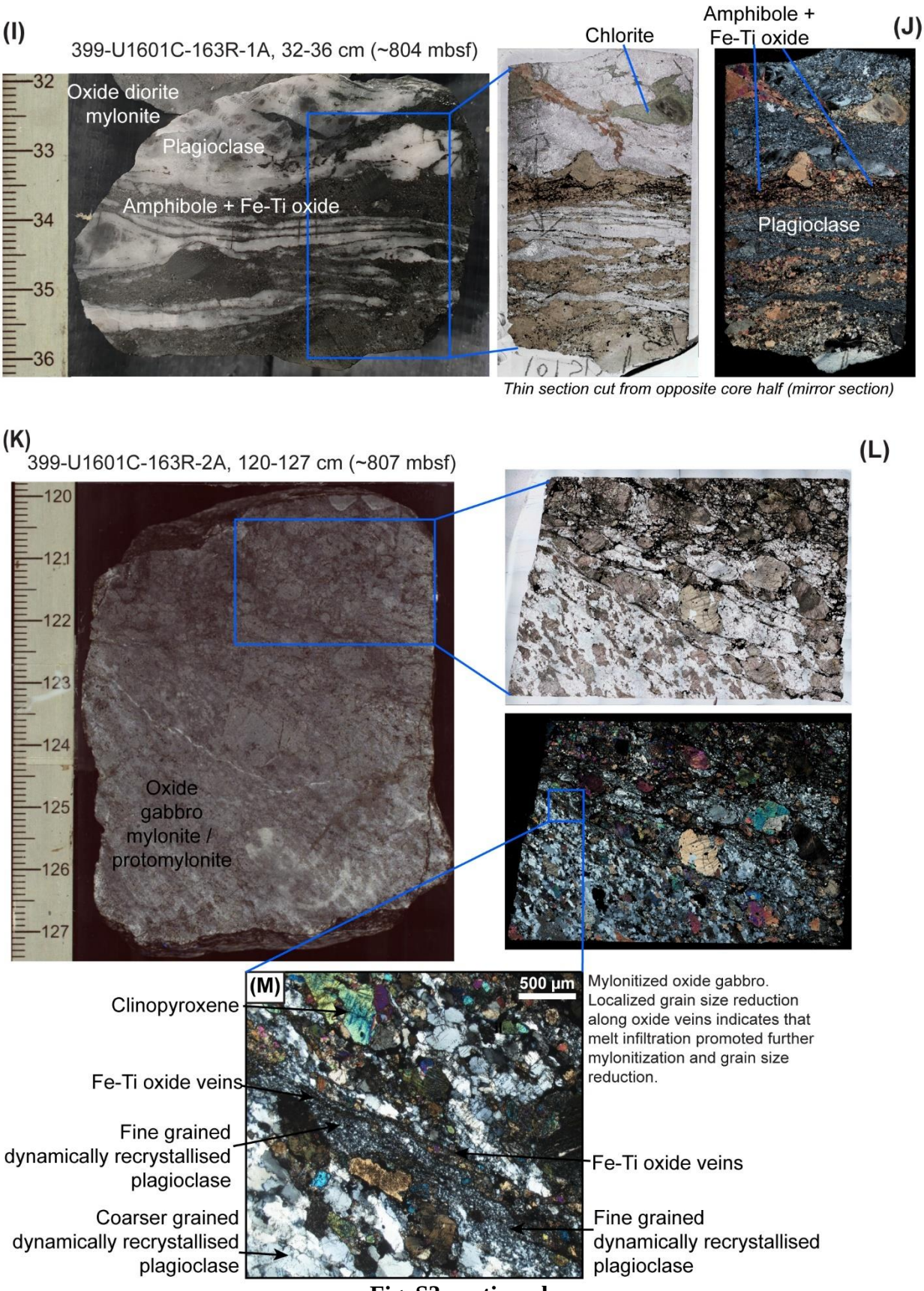

Fig. S3 continued.

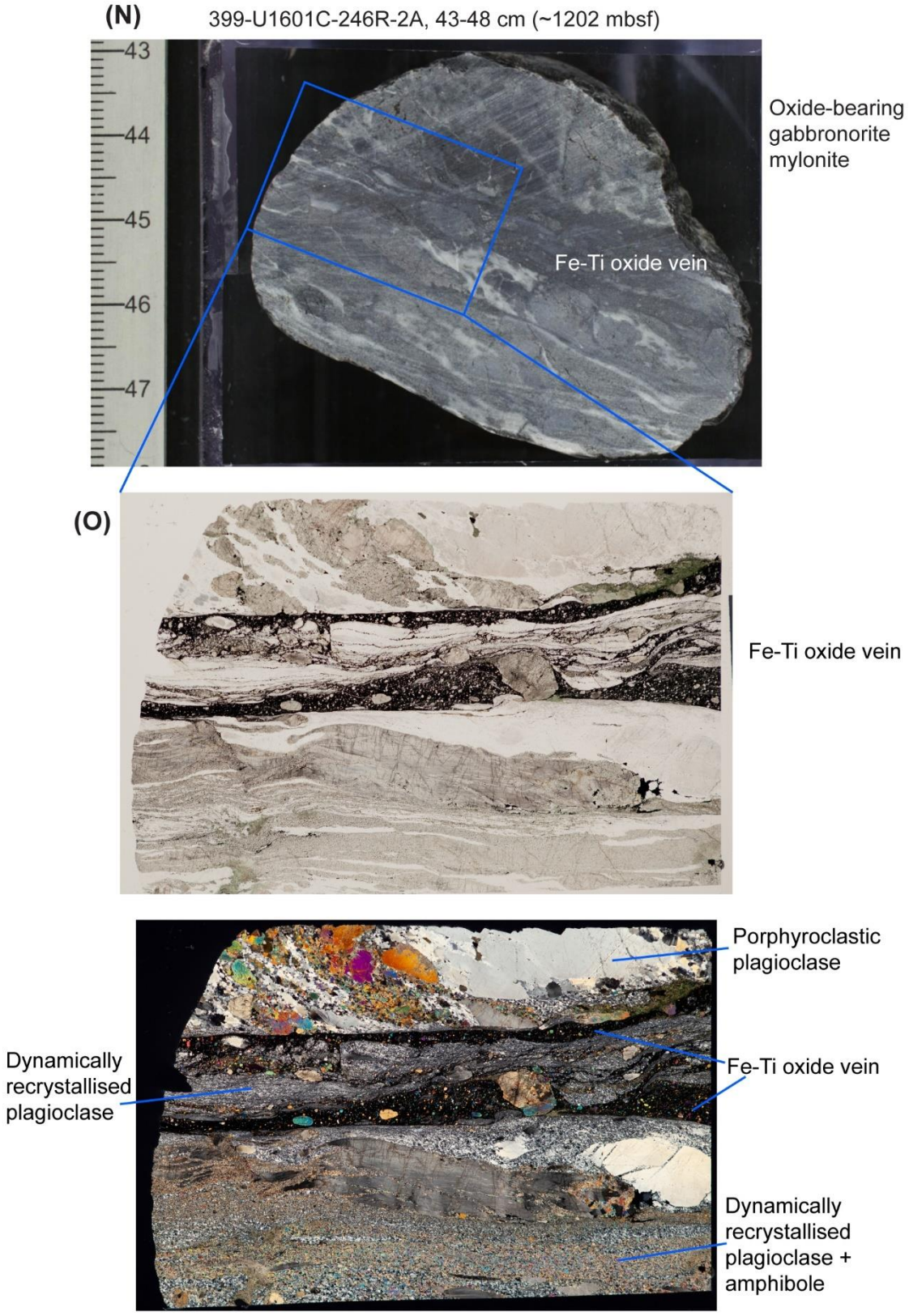

Fig. S3 continued.

Fig. S4A-O.

Close-up core images, thin-section scans, and photomicrographs of representative high-strain ductile deformation intervals localizing at ultramafic-mafic contacts.

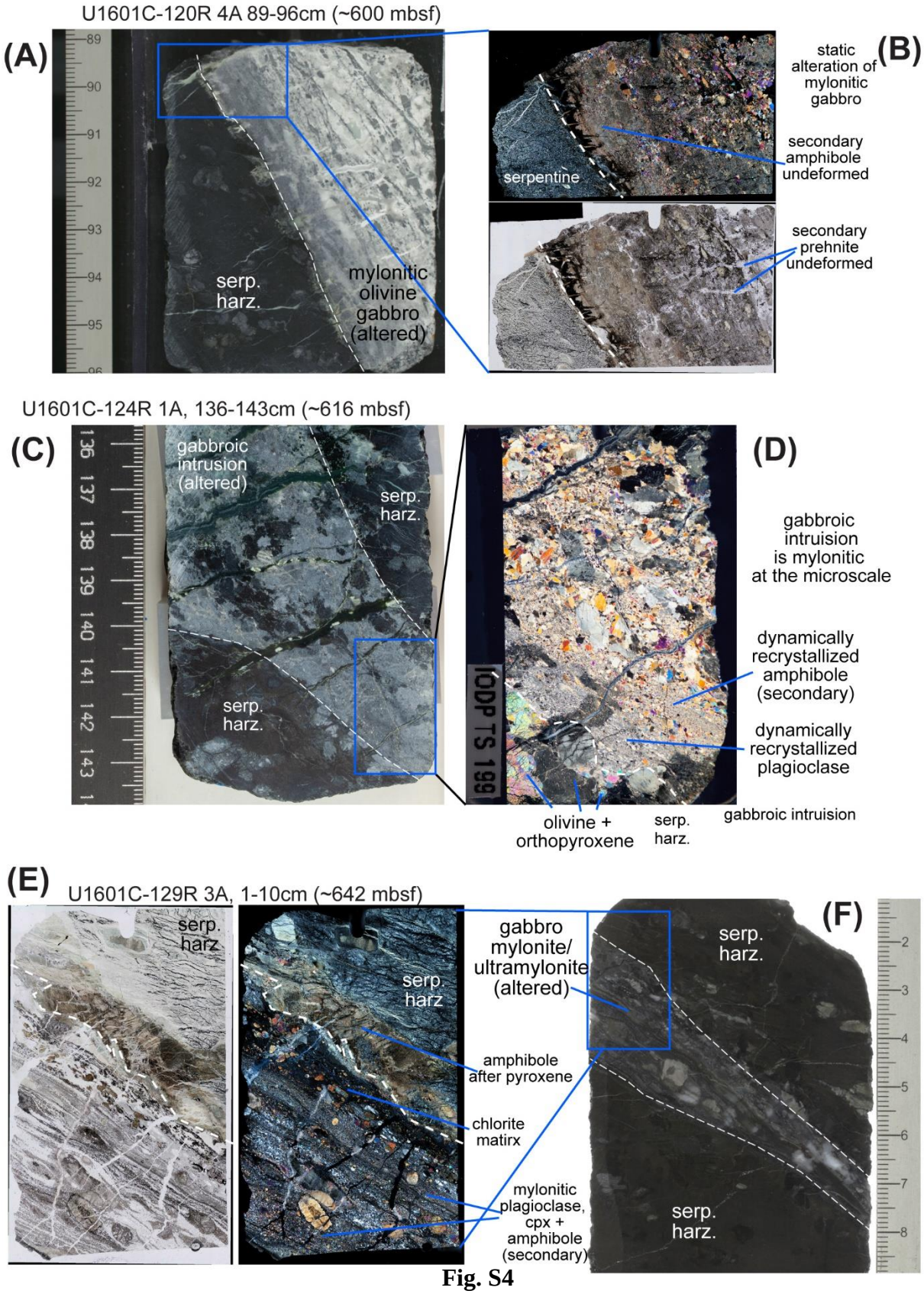
U1601C-120R 4A 89-96cm (~600 mbsf)
(A)
(B)
serp. harz.
mylonitic olivine gabbro (altered)
serpentine
static alteration of mylonitic gabbro
secondary amphibole undeformed
secondary prehnite undeformed
U1601C-124R 1A, 136-143cm (~616 mbsf)
(C)
(D)
gabbroic intrusion (altered)
serp. harz.
serp. harz.
IODP TS 199
gabbroic intruision is mylonitic at the microscale
dynamically recrystallized amphibole (secondary)
dynamically recrystallized plagioclase
olivine + orthopyroxene
serp. harz.
gabbroic intrusion
(E)
U1601C-129R 3A, 1-10cm (~642 mbsf)
(F)
serp. harz
serp. harz
gabbro mylonite/ ultramylonite (altered)
amphibole after pyroxene
chlorite matirx
mylonitic plagioclase, cpx + amphibole (secondary)
serp. harz.
serp. harz.

Fig. S4

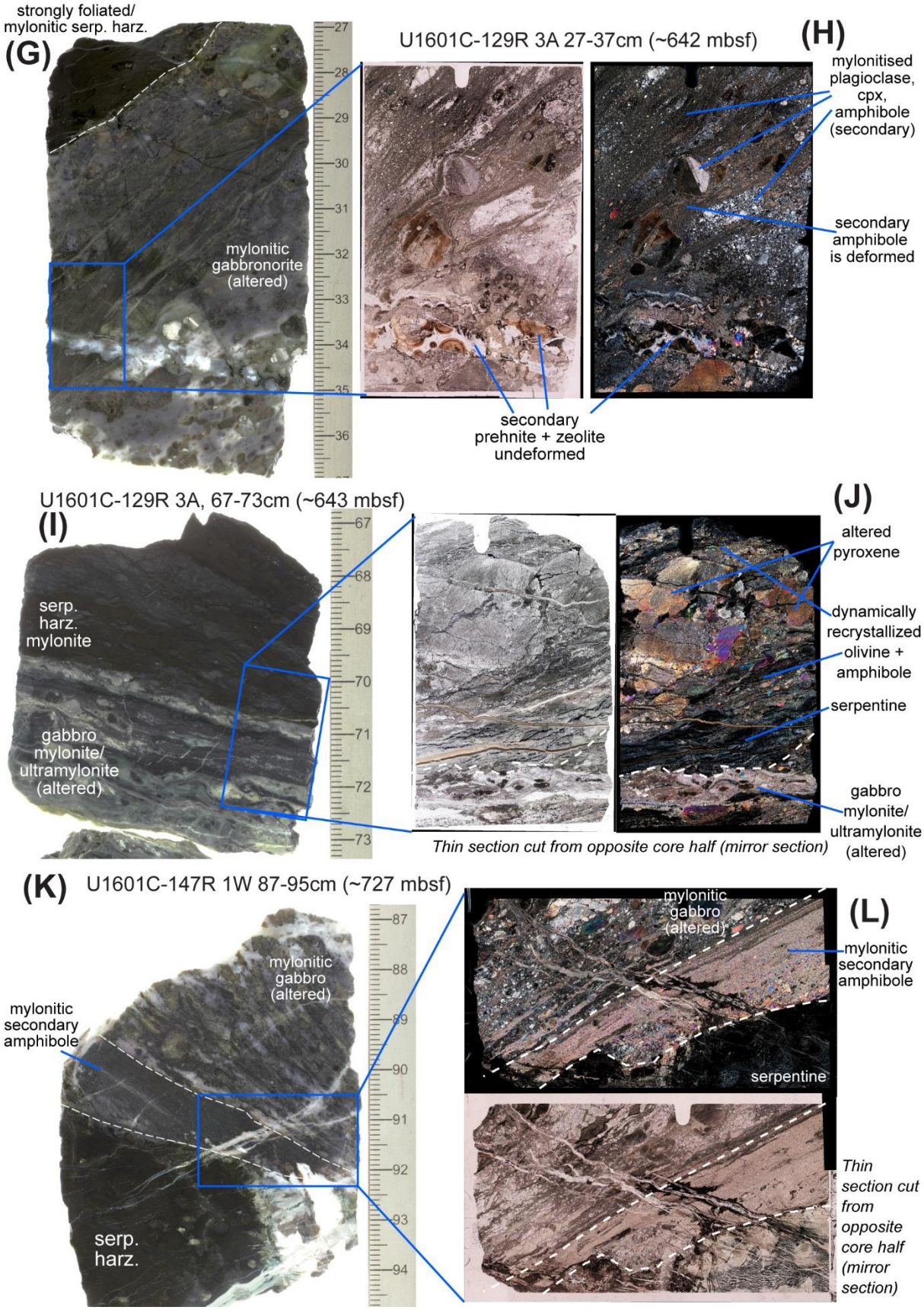

Fig. S4 continued.

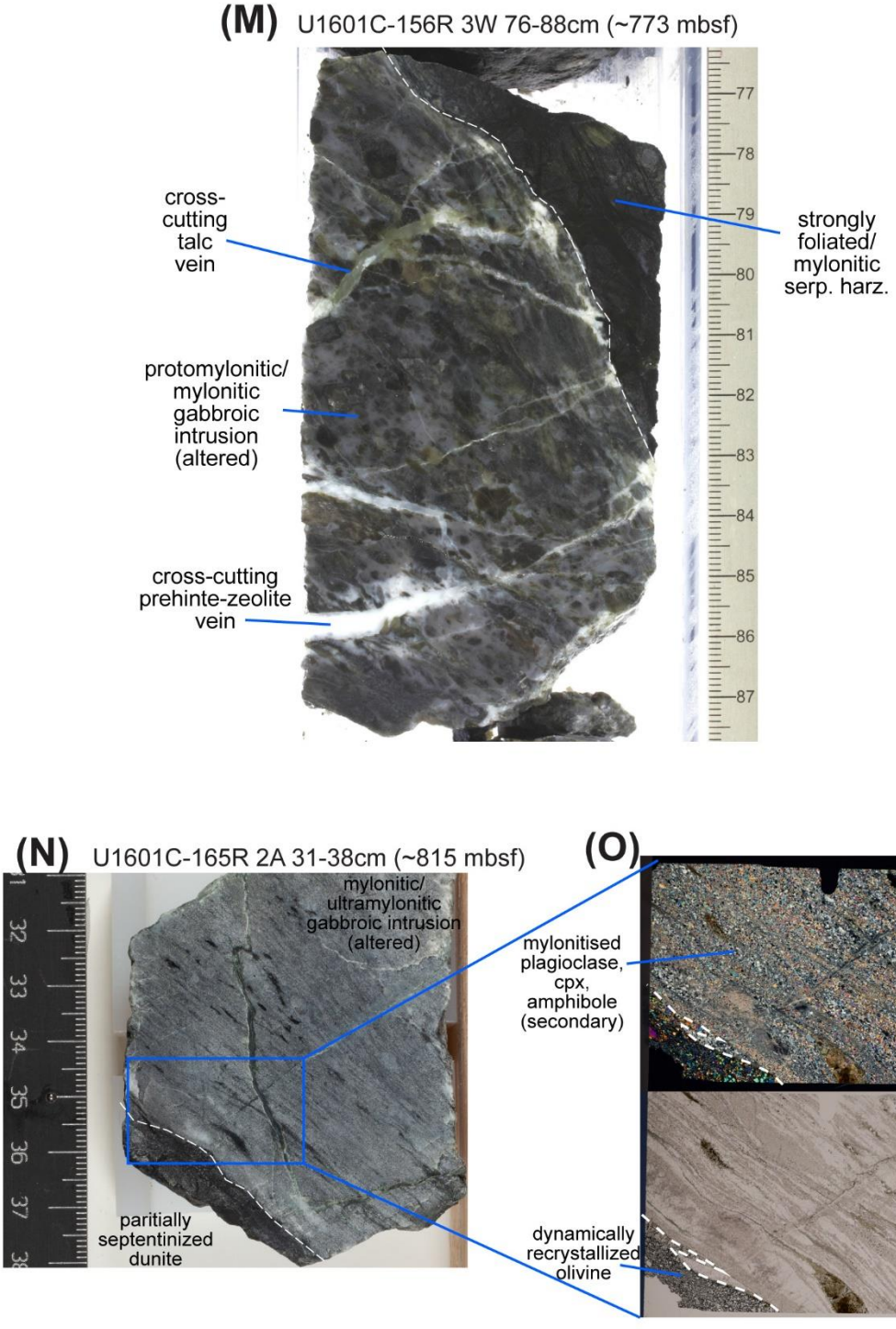

Fig. S4 continued.

Fig. S5A-I.

Close-up core images, thin-section scans, and photomicrographs of representative high-strain ductile deformation intervals localizing at mafic-mafic contacts.

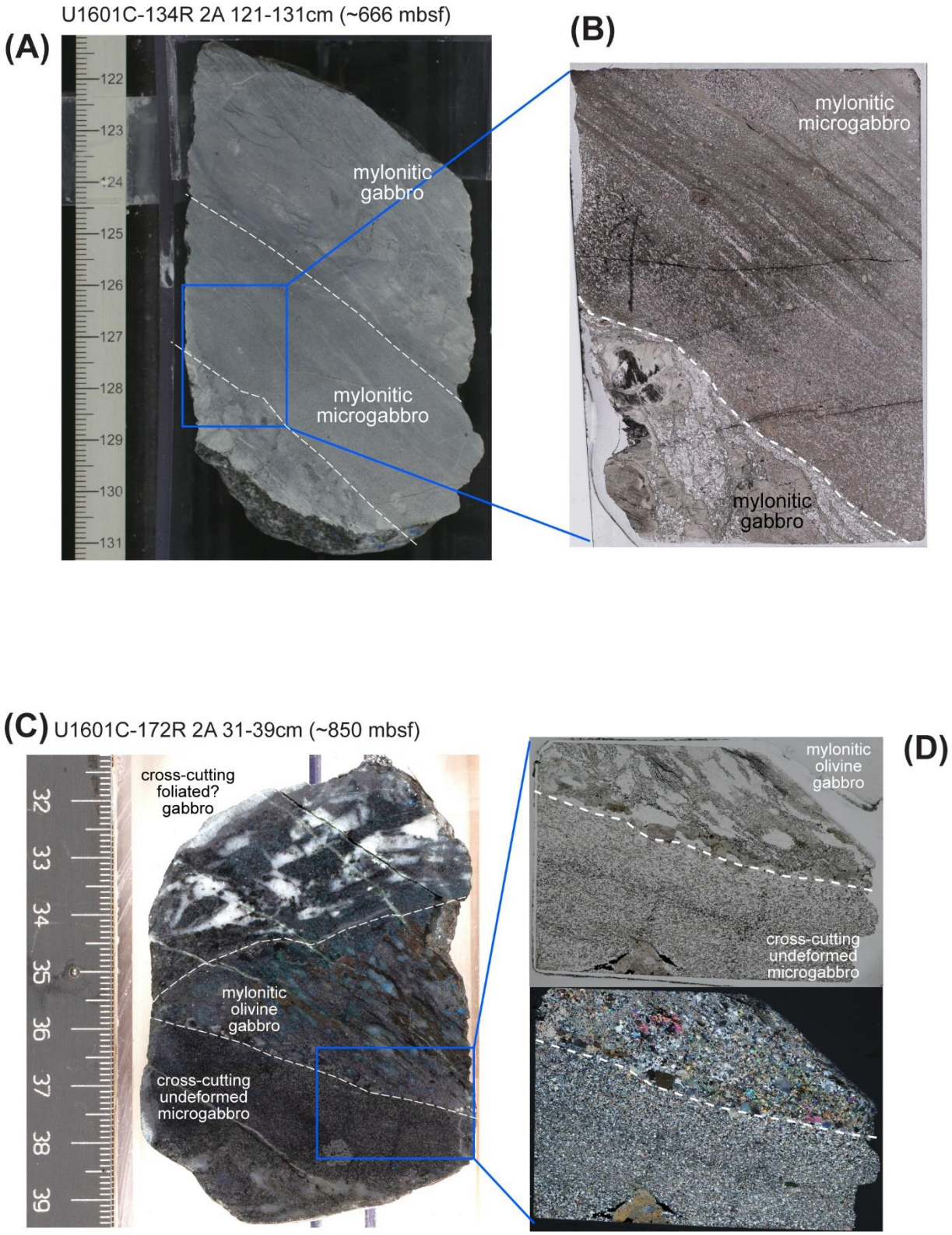
(A)
U1601C-134R 2A 121-131cm (~666 mbsf)
122
123
124
125
126
127
128
129
130
131
mylonitic gabbro
mylonitic microgabbro
(B)
mylonitic microgabbro
mylonitic gabbro
(C)
U1601C-172R 2A 31-39cm (~850 mbsf)
32
33
34
35
36
37
38
39
cross-cutting foliated? gabbro
mylonitic olivine gabbro
cross-cutting undeformed microgabbro
(D)
mylonitic olivine gabbro
cross-cutting undeformed microgabbro

Fig. S5

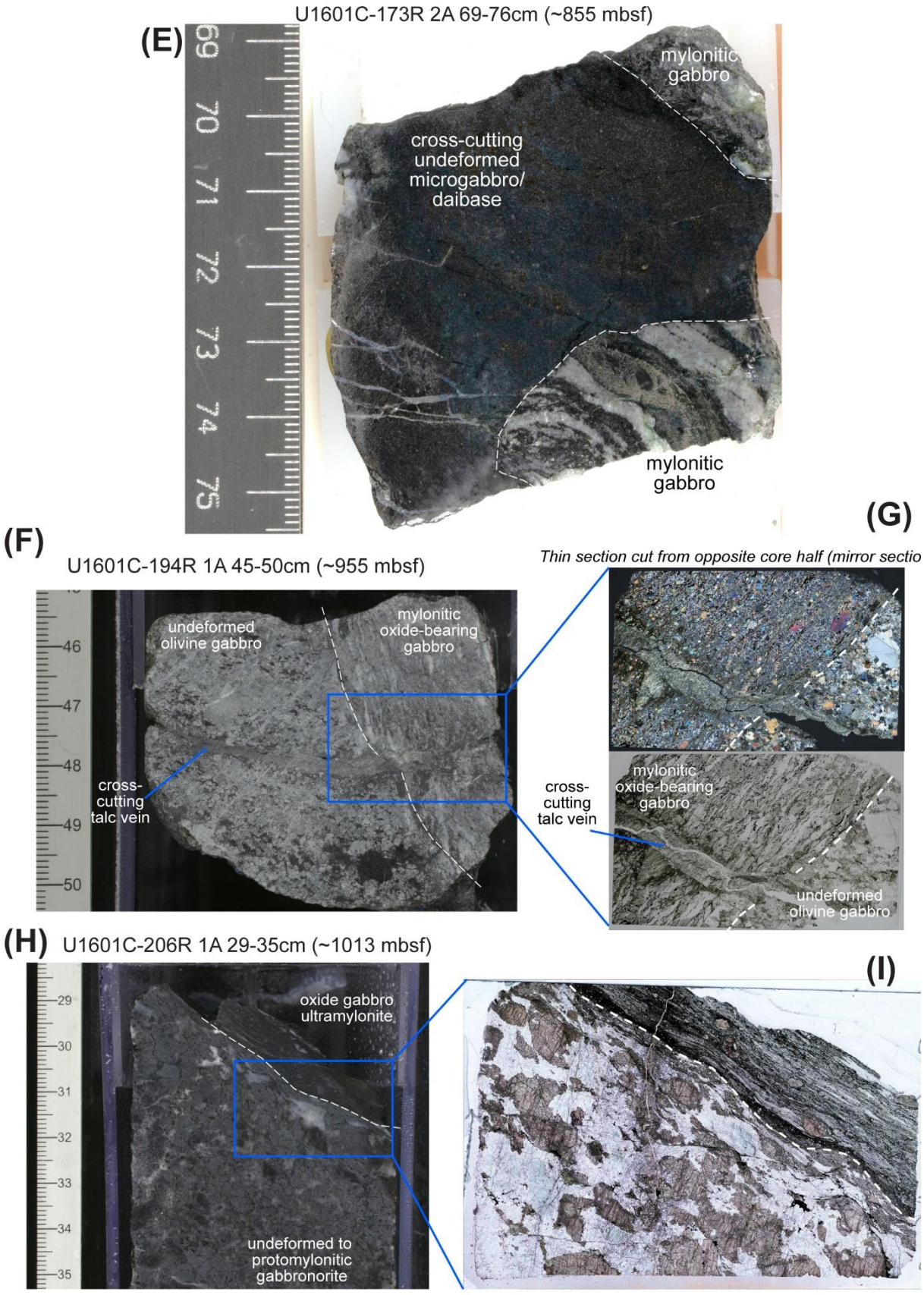

Fig. S5 continued.

Fig. S6.

Representative core images and thin section scans of serpentinized peridotite intervals within Hole U1601C, showing a range of mantle fabrics including protogranular, porphyroclastic – weakly foliated, porphyroclastic – strongly foliated, and porphyroclastic / protomylonitic. Further descriptions and explanations of mantle fabrics described from Hole U1601C are presented in McCaig et al 2025.

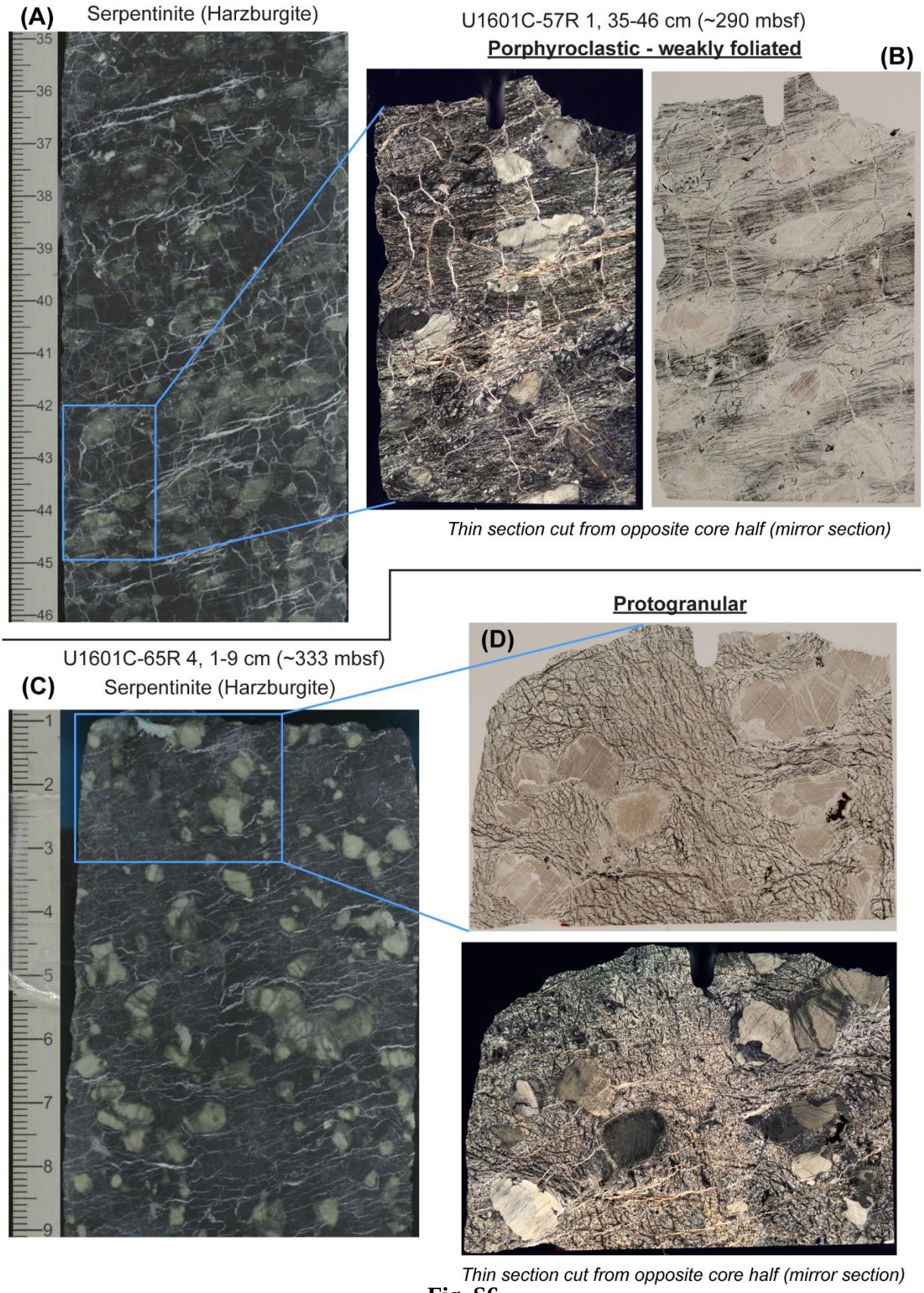
(A)
Serpentinite (Harzburgite)
U1601C-57R 1, 35-46 cm (~290 mbsf)
Porphyroclastic - weakly foliated
(B)
Thin section cut from opposite core half (mirror section)
Protogranular
(D)
U1601C-65R 4, 1-9 cm (~333 mbsf)
(C)
Serpentinite (Harzburgite)
Thin section cut from opposite core half (mirror section)

Fig. S6

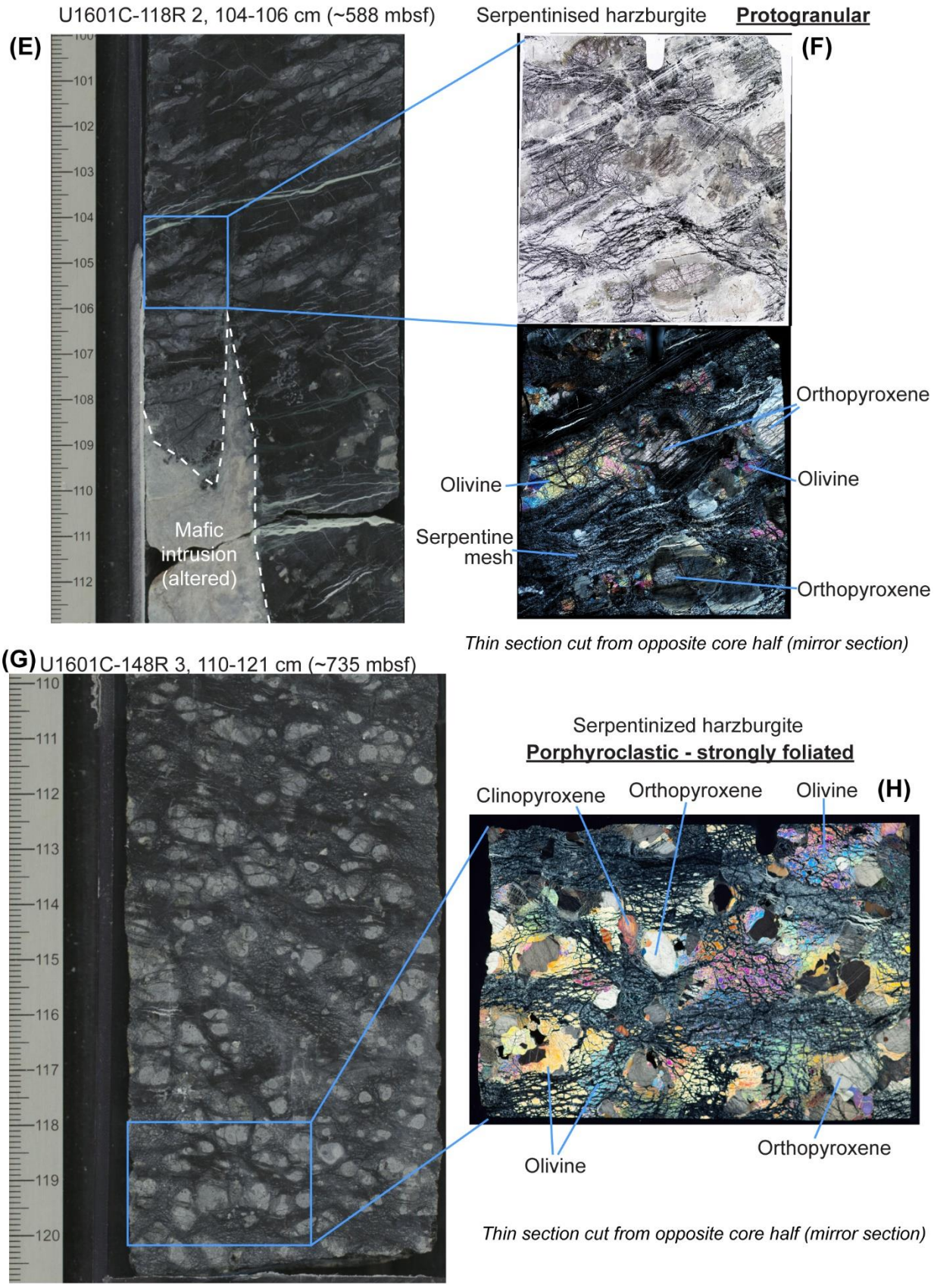

Fig. S6 continued.

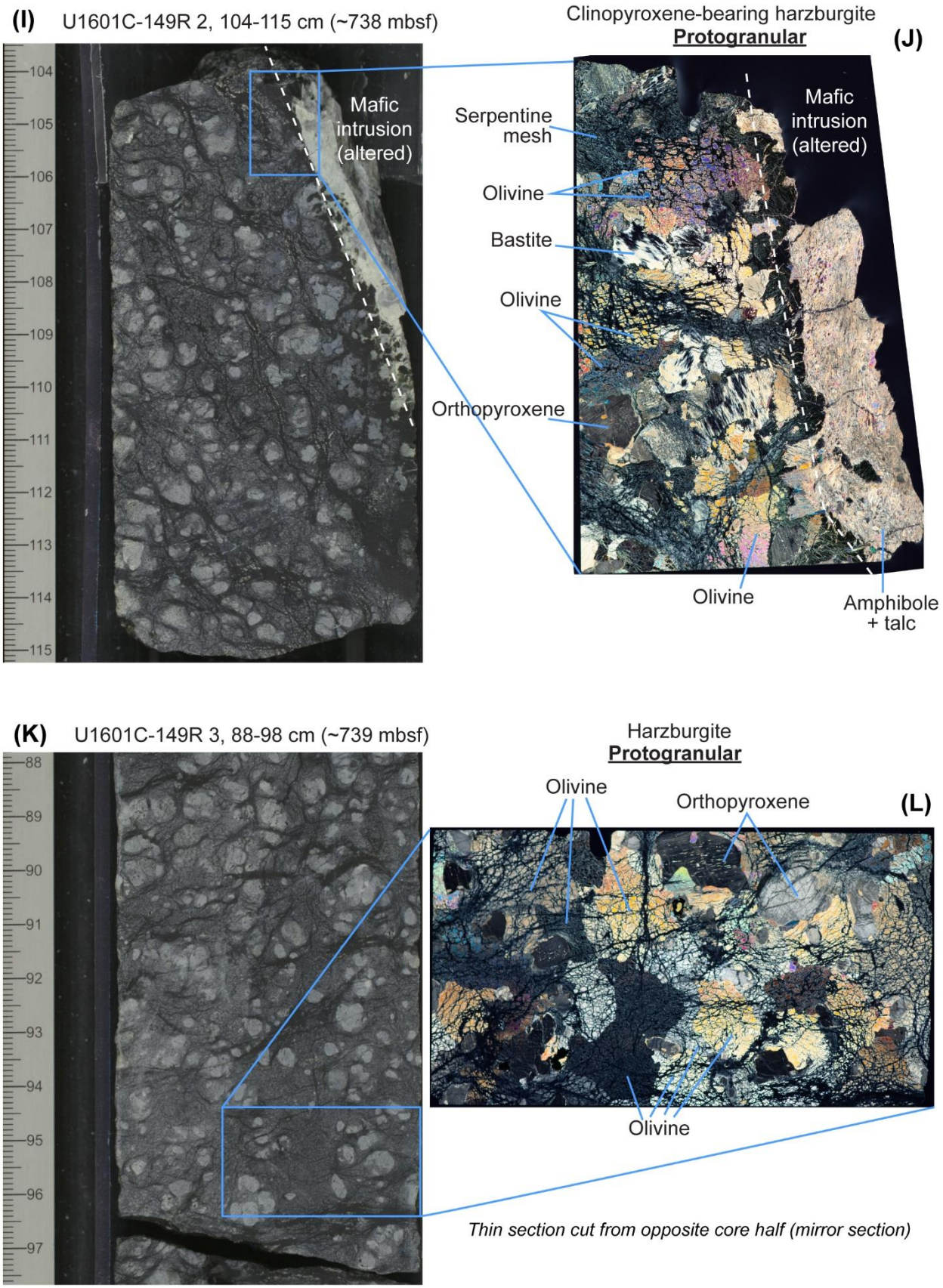

Fig. S6 continued.

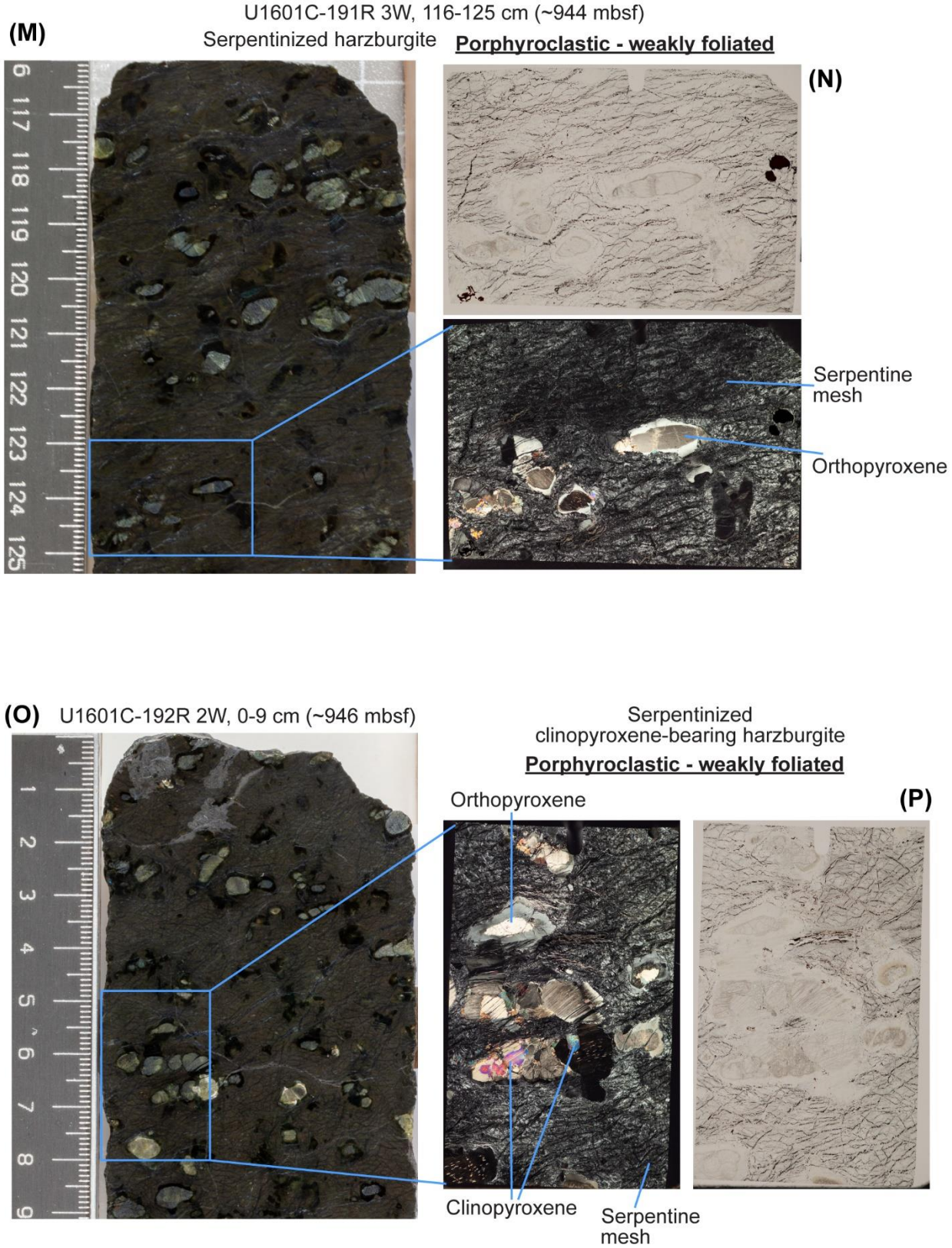

Fig. S6 continued.

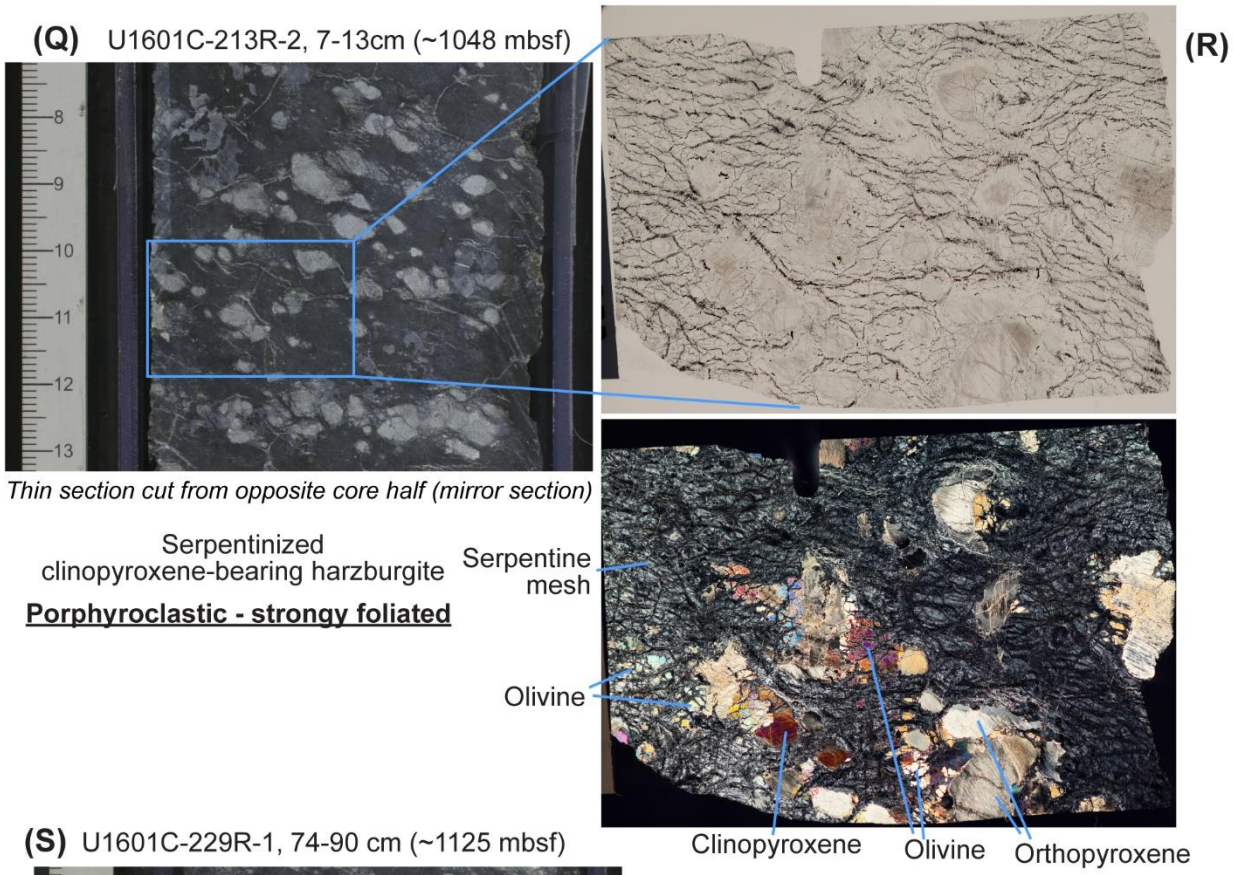

Fig. S6 continued.

Fig. S7.
Back scatter electron (BSE) plus electron dispersive spectroscopy (EDS) element map montage images of melt-present ductile deformation fabrics and alteration assemblages. Grey scale BSE images show distribution of elementally heavy (bright) vs elementally light (dark) minerals. Colour image overlays are layered images of Mg (green), Ca (purple), Al (blue), Na (turquoise), Ti (red), and S (yellow) EDS element maps. (A) U1601C-131R-1, 43-46 cm (TS80 – 649 mbsf): Olivine-bearing gabbro mylonite (BSE-EDS image of Fig. 6B), showing olivine (light green) porphyroclasts surrounded by olivine neoblasts and secondary orthopyroxene (dark green), and clinopyroxene (pink) neoblasts within foliation bands of dynamically recrystallized secondary amphibole (turquoise). Plagioclase (blue-to-indigo) rims show enrichment in Na relative to Al and Ca. (B) U1601C-206R-1, 35-38 cm (TS120 – 1013 mbsf): Oxide gabbronorite ultramylonite with ilmenite (pale red) and magnetite (white) forming melt pseudomorphs in sigmoidal pressure shadows of orthopyroxene, indicating melt-present mylonitic deformation. (C) Same sample as S7B showing irregular shaped interstitial grains of ilmenite and magnetite with low dihedral grain boundary triple junction angles indicative of melt-psuedomorphs. (D) U1601C-159R-3, 29-32 cm (TS99 – 788 mbsf): Oxide gabbronorite ultramylonite with magnetite grains showing ilmenite exsolution lamellae. (E) U1601C-131R-2, 62-64 cm (TS82 – 651 mbsf): Gabbronorite mylonite showing interstitial secondary amphibole with low dihedral grain boundary triple junction angles surrounded by plagioclase, indicative of melt-pseudomorphs. (F) U1601C-133R-1, 19-22 cm (TS85 – 689 mbsf): BSE image of Fig. 8A - Gabbro mylonite showing foliation-parallel, wing-shaped pressure shadows of secondary brown amphibole mantling clinopyroxene neoblasts. Mineral abbreviations are listed in Fig. 6. caption.

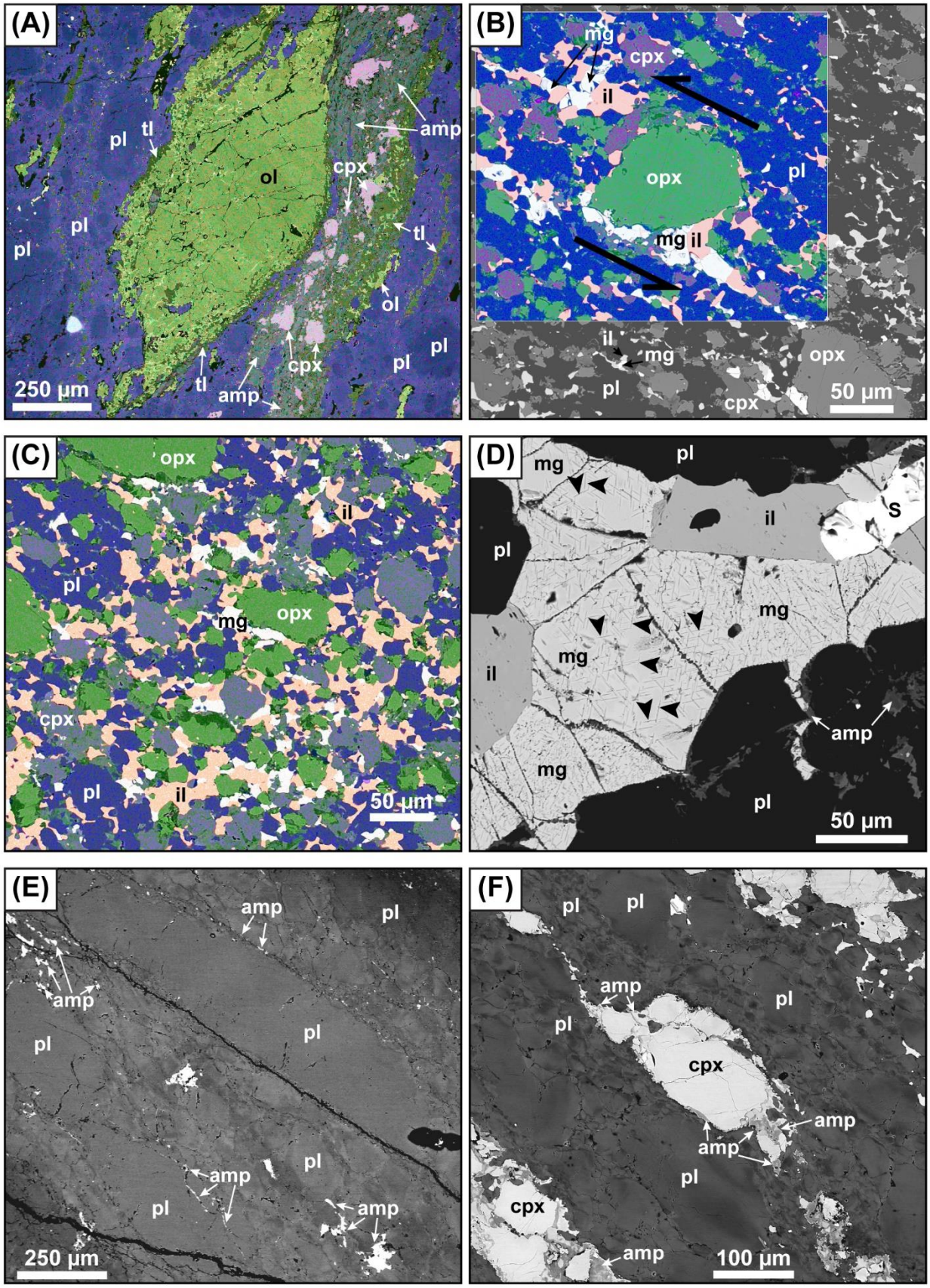
(A)
pl
tl
amp
ol
cpx
pl
pl
tl
ol
pl
pl
tl
amp
cpx
250 µm
(B)
mg
cpx
il
opx
pl
mg il
il
mg
opx
pl
cpx
50 µm
(C)
opx
il
pl
mg
opx
cpx
pl
il
50 µm
(D)
mg
pl
il
S
pl
mg
mg
il
amp
mg
pl
50 µm
(E)
amp
pl
amp
pl
pl
pl
amp
pl
amp
250 µm
(F)
pl
pl
amp
pl
pl
cpx
amp
amp
pl
cpx
amp
100 µm

Fig. S7

	Ductile Deformation Intervals	Interval Thickness (m)
Low Strain	weakly foliated/lineated	14.22
	strongly foliated/lineated	16.95
High Strain	protomylonite	33.27
	mylonitic	14.72
	ultramylonitic	0.60
	Total Thickness - All Ductile Intervals	**79.7 m**
	Total Thickness - All High Strain Intervals	**48.6 m**
	Total Thickness of Ductile Intervals Below 637 mbsf	**72.1 m**
	% of Ductile Intervals below 637 mbsf	**90.4%**

	% of U1601C Currated Thickness
Ductile Intervals	**8.2%**
High Strain Ductile Intervals	**5.0%**
Ductile Intervals below 637 mbsf	**15.1%**
High Strain Ductile Intervals below 637 mbsf	**9.2%**

Table S1.

Ductile deformation interval thicknesses

Lithology	Ductile Interval thickness (cm)	weakly foliated/lineated	strongly foliated/lineated	protomylonite	mylonite	ultramylonite		low strain	high strain
dunite	206	8	198	0	0	0		206	**0**
orthopyroxene-bearing dunite	635	56	486	30	63	0		542	**93**
Harzburgite	574	121	161	283	9	0		282	**292**
olivine-bearing gabbro	379	34	68	186	91	0		102	**277**
olivine gabbro	263	22	44	85	100	12		66	**197**
orthopyroxene-bearing olivine gabbro	16	0	0	5	0	11		0	**16**
olivine-bearing gabbronorite	160	0	29	97	34	0		29	**131**
olivine gabbronorite	8	0	0	8	0	0		0	**8**
Gabbro	1748.5	165	174.5	1034	348	27		339.5	**1409**
orthopyroxene-bearing gabbro	233	61	159	13	0	0		220	**13**
gabbronorite	1553.5	442.5	168	431	503	9		610.5	**943**
oxide-bearing gabbro	360	159	42	114	45	0		201	**159**
disseminated oxide gabbro	557	276	43	225	13	0		319	**238**
oxide gabbro	651.5	41	95	412	102.5	1		136	**515.5**
disseminated oxide gabbronorite	497	36	0	313	148	0		36	**461**
oxide gabbronorite	106	0	0	91	15	0		0	**106**
talc schist	27	0	27	0	0	0		27	**0**
SUM	7974.5	1421.5	1694.5	3327	1471.5	60		3116	4858.5

Lithology (Grouped)	Ductile Interval thickness (cm)	weakly foliated/lineated	strongly foliated/lineated	protomylonite	mylonite	ultramylonite		low strain	high strain
Ultramafic	**1415**	**185**	**845**	**313**	**72**	**0**		**1030**	**385**
Olivine gabbro/gabbronorite	**826**	**56**	**141**	**381**	**225**	**23**		**197**	**629**
Gabbro	**1748.5**	**165**	**174.5**	**1034**	**348**	**27**		**339.5**	**1409**
disseminated oxide gabbro	**557**	**276**	**43**	**225**	**13**	**0**		**319**	**238**
oxide gabbro	**1117.5**	**200**	**137**	**617**	**162.5**	**1**		**337**	**780.5**
disseminated oxide gabbronorite	**497**	**36**	**0**	**313**	**148**	**0**		**36**	**461**
gabbronorite	**1786.5**	**503.5**	**327**	**444**	**503**	**9**		**830.5**	**956**
	7974.5	**1421.5**	**1667.5**	**3327**	**1471.5**	**60**		**3089**	**4858.5**

Lithology	Ductile Interval thickness (cm)	weakly foliated/lineated	strongly foliated/lineated	protomylonite	mylonite	ultramylonite		low strain	high strain
dunite	2.58%	0.56%	11.68%	0.00%	0.00%	0.00%		6.61%	0.00%
orthopyroxene-bearing dunite	7.96%	3.94%	28.68%	0.90%	4.28%	0.00%		17.39%	1.91%
Harzburgite	7.20%	8.51%	9.50%	8.51%	0.61%	0.00%		9.05%	6.01%
olivine-bearing gabbro	4.75%	2.39%	4.01%	5.59%	6.18%	0.00%		3.27%	5.70%
olivine gabbro	3.30%	1.55%	2.60%	2.55%	6.80%	20.00%		2.12%	4.05%
orthopyroxene-bearing olivine gabbro	0.20%	0.00%	0.00%	0.15%	0.00%	18.33%		0.00%	0.33%
olivine-bearing gabbronorite	2.01%	0.00%	1.71%	2.92%	2.31%	0.00%		0.93%	2.70%
olivine gabbronorite	0.10%	0.00%	0.00%	0.24%	0.00%	0.00%		0.00%	0.16%
Gabbro	21.93%	11.61%	10.30%	31.08%	23.65%	45.00%		10.90%	29.00%
orthopyroxene-bearing gabbro	2.92%	4.29%	9.38%	0.39%	0.00%	0.00%		7.06%	0.27%
gabbronorite	19.48%	31.13%	9.91%	12.95%	34.18%	15.00%		19.59%	19.41%
oxide-bearing gabbro	4.51%	11.19%	2.48%	3.43%	3.06%	0.00%		6.45%	3.27%
disseminated oxide gabbro	6.98%	19.42%	2.54%	6.76%	0.88%	0.00%		10.24%	4.90%
oxide gabbro	8.17%	2.88%	5.61%	12.38%	6.97%	1.67%		4.36%	10.61%
disseminated oxide gabbronorite	6.23%	2.53%	0.00%	9.41%	10.06%	0.00%		1.16%	9.49%
oxide gabbronorite	1.33%	0.00%	0.00%	2.74%	1.02%	0.00%		0.00%	2.18%
talc schist	0.34%	0.00%	1.59%	0.00%	0.00%	0.00%		0.87%	0.00%
SUM	100.00%	100.00%	100.00%	100.00%	100.00%	100.00%		100.00%	100.00%

Lithology (Grouped)	Ductile Interval thickness (cm)	weakly foliated/lineated	strongly foliated/lineated	protomylonite	mylonite	ultramylonite		low strain	high strain
Ultramafic	18%	13%	50%	9%	5%	0%		33%	8%
Olivine gabbro/gabbronorite	10%	4%	8%	11%	15%	38%		6%	13%
Gabbro	22%	12%	10%	31%	24%	45%		11%	29%
disseminated oxide gabbro	7%	19%	3%	7%	1%	0%		10%	5%
oxide gabbro	14%	14%	8%	19%	11%	2%		11%	16%
disseminated oxide gabbronorite	6%	3%	0%	9%	10%	0%		1%	9%
gabbronorite	22%	35%	19%	13%	34%	15%		27%	20%
	100%	100%	98%	100%	100%	100%		99%	100%

Table S2.
Ductile deformation interval thickness and % distributed by lithology.

`	HSZ1	HSZ2	HSZ3	HSZ4	HSZ5	HSZ6
Top depth (mbsf)	637.41	867.2	949.5	1036.85	1130.175	1169.5
Bottom depth (mbsf)	665.89	884.83	975.95	1053.06	1151.98	1175.98
Top Core	128R3	176R1	193R1	211R1	230R2	238R2
Bottom Core	134R2	179R3	198R2	214R2	234R3	239R3
Hole thickness (m)	28.48	17.63	26.45	16.21	21.805	6.48
Currated thickness (m)	23.85	11.45	14.76	11.815	16.075	5.84
Recovered thickness (m)	21.51	11.49	11.05	10.98	14	3.91
Currated Thickness (% of Hole Thickness)	84%	65%	56%	73%	74%	90%
Recovered Thickness (% of Hole Thickness)	76%	65%	42%	68%	64%	60%
Ductile Intervals Combined Thickness (m)	7.5	6.655	5.04	4.23	12.19	5.31
Ductile Intervals Combined Thickness - Low Strain (m)	2.19	1.88	0.75	1.2	3.09	0.49
Ductile Intervals Combined Thickness - High Strain (m)	5.31	4.775	4.29	3.03	9.1	4.82
Ductile Intervals (% of Currated Thickness)	31%	58%	34%	36%	76%	91%
Low Strain Ductile Intervals (% of Currated Thickness)	9%	16%	5%	10%	19%	8%
High Strain Ductile Intervals (% of Currated Thickness)	22%	42%	29%	26%	57%	83%

Table S3.
Thicknesses of High Strain Zones (HSZs) 1 to 6 showing total ductile deformation interval thickness and % within each HSZ.

Lithology	HSZ1	HSZ2	HSZ3	HSZ4	HSZ5	HSZ6
orthopyroxene-bearing dunite	0.15	0.63	0	0	0	0
Harzburgite	2.24	0.09	0.44	0	0	0
olivine-bearing gabbro	0.73	1.06	0.97	0	0	0
olivine gabbro	0.58	0.8	0.44	0.1	0	0
orthopyroxene-bearing olivine gabbro	0.11	0	0	0	0	0
olivine-bearing gabbronorite	0	0	0.81	0	0	0
olivine gabbronorite	0	0	0	0	0	0
Gabbro	3.19	0.885	0.74	2.5	0	0.38
orthopyroxene-bearing gabbro	0	0	0	0	0	0
gabbronorite	0.22	0	0.54	0	7.15	0
oxide-bearing gabbro	0	0.77	0	1.35	0	0.31
disseminated oxide gabbro	0.06	2.01	0.15	0.28	2.75	0
oxide gabbro	0.22	0.41	0.04	0	1.06	1.06
disseminated oxide gabbronorite	0	0	0	0	1.23	3.56
oxide gabbronorite	0	0	0.91	0	0	0
TOTAL	7.5	6.655	5.04	4.23	12.19	5.31

Lithology	HSZ1	HSZ2	HSZ3	HSZ4	HSZ5	HSZ6
orthopyroxene-bearing dunite	2.0%	9.5%	0.0%	0.0%	0.0%	0.0%
Harzburgite	29.9%	1.4%	8.7%	0.0%	0.0%	0.0%
olivine-bearing gabbro	9.7%	15.9%	19.2%	0.0%	0.0%	0.0%
olivine gabbro	7.7%	12.0%	8.7%	2.4%	0.0%	0.0%
orthopyroxene-bearing olivine gabbro	1.5%	0.0%	0.0%	0.0%	0.0%	0.0%
olivine-bearing gabbronorite	0.0%	0.0%	16.1%	0.0%	0.0%	0.0%
olivine gabbronorite	0.0%	0.0%	0.0%	0.0%	0.0%	0.0%
Gabbro	42.5%	13.3%	14.7%	59.1%	0.0%	7.2%
orthopyroxene-bearing gabbro	0.0%	0.0%	0.0%	0.0%	0.0%	0.0%
gabbronorite	2.9%	0.0%	10.7%	0.0%	58.7%	0.0%
oxide-bearing gabbro	0.0%	11.6%	0.0%	31.9%	0.0%	5.8%
disseminated oxide gabbro	0.8%	30.2%	3.0%	6.6%	22.6%	0.0%
oxide gabbro	2.9%	6.2%	0.8%	0.0%	8.7%	20.0%
disseminated oxide gabbronorite	0.0%	0.0%	0.0%	0.0%	10.1%	67.0%
oxide gabbronorite	0.0%	0.0%	18.1%	0.0%	0.0%	0.0%
TOTAL	100.0%	100.0%	100.0%	100.0%	100.0%	100.0%

Lithology (Grouped)	HSZ1	HSZ2	HSZ3	HSZ4	HSZ5	HSZ6
Ultramafic	32%	11%	9%	0%	0%	0%
Olivine gabbro/gabbronorite	19%	28%	44%	2%	0%	0%
Gabbro	43%	13%	15%	59%	0%	7%
disseminated oxide gabbro	1%	30%	3%	7%	23%	0%
oxide gabbro	3%	18%	19%	32%	9%	26%
disseminated oxide gabbronorite	0%	0%	0%	0%	10%	67%
gabbronorite	3%	0%	11%	0%	59%	0%
TOTAL	100.0%	100.0%	100.0%	100.0%	100.0%	100.0%

Table S4.

Thickness and percentage distribution of ductile deformation interval lithology for HSZs 1 to 6

Data S1. (separate file)

Ductile deformation interval and lithology interval datasets used in this study presented in an excel file, alongside Tables S1 to S4 (above)